1 Historical greenhouse gas concentrations

2 Malte Meinshausen[1,2,3] Elisabeth Vogel[1,2], Alexander Nauels[1,2], Katja Lorbacher[1,2], Nicolai Meinshausen[4], David Etheridge[5],
3 Paul Fraser[5], Stephen A. Montzka[6], Peter Rayner[2], Cathy Trudinger[5], Paul Krummel[5], Urs Beyerle[7], Josep G. Canadell[8], John
4 S. Daniel[9], Ian Enting[10], Rachel M. Law[5], Simon O'Doherty[11], Ron G. Prinn[12], Stefan Reimann[13], Mauro Rubino[5,14], Guus J.M.
5 Velders[15], Martin K. Vollmer[13], Ray Weiss[16]

6 [1]Australian-German Climate & Energy College, The University of Melbourne, Parkville, Victoria, Australia
7 [2]Department of Earth Sciences, The University of Melbourne, Parkville, Victoria, Australia
8 [3]Potsdam Institute for Climate Impact Research, Potsdam, Germany
9 [4]Seminar for Statistics, Swiss Federal Institute of Technology (ETH Zurich), Zurich, Switzerland.
10 [5]CSIRO Oceans and Atmosphere, Aspendale, Victoria, Australia
11 [6]NOAA, Earth System Research Laboratory, Global Monitoring Division, Boulder, Colorado, USA
12 [7]Institute for Atmospheric and Climate Science, Swiss Federal Institute of Technology, Zurich (ETH Zurich), Switzerland
13 [8]Global Carbon Project, CSIRO Oceans and Atmosphere, Canberra, ACT, Australia
14 [9]NOAA, Earth System Research Laboratory, Chemical Sciences Division, Boulder, Colorado, USA
15 [10]The University of Melbourne, Victoria, Australia (retired)
16 [11]University of Bristol, Bristol, United Kingdom
17 [12]MIT, Cambridge, MA, United States
18 [13]Empa, Swiss Federal Laboratories for Materials Science and Technology, Laboratory for Air Pollution and Environmental
19 Technology, Switzerland
20 [14]Dipartimento di matematica e fisica, Seconda Università degli studi di Napoli, 81100 Caserta, Italy
21 [15]National Institute for Public Health and the Environment (RIVM), Bilthoven, Netherlands
22 [16]Scripps Institution of Oceanography, La Jolla, CA, United States
23
24 *Correspondence to:* M. Meinshausen (malte.meinshausen@unimelb.edu.au)

25 **Abstract.** Atmospheric greenhouse gas concentrations are at unprecedented, record-high levels compared to pre-industrial
26 reconstructions over the last 800,000 years. Those elevated greenhouse gas concentrations warm the planet and together with
27 net cooling effects by aerosols, they are the reason of observed climate change over the past 150 years. An accurate
28 representation of those concentrations is hence important to understand and model recent and future climate change. So far,
29 community efforts to create composite datasets with seasonal and latitudinal information have focused on marine boundary
30 layer conditions and recent trends since 1980s. Here, we provide consolidated data sets of historical atmospheric (volume)
31 mixing ratios of 43 greenhouse gases specifically for the purpose of climate model runs. The presented datasets are based on
32 AGAGE and NOAA networks and a large set of literature studies. In contrast to previous intercomparisons, the new datasets
33 are latitudinally resolved, and include seasonality over the period between year 0 to 2014. We assimilate data for CO_2, methane
34 (CH_4) and nitrous oxide (N_2O), 5 chlorofluorocarbons (CFCs), 3 hydrochlorofluorocarbons (HCFCs), 16 hydrofluorocarbons
35 (HFCs), 3 halons, methyl bromide (CH_3Br), 3 perfluorocarbons (PFCs), sulfur hexafluoride (SF_6), nitrogen triflouride (NF_3)
36 and sulfuryl fluoride (SO_2F_2). We estimate 1850 annual and global mean surface mixing ratios of CO_2 at 284.3 ppmv, CH_4 at
37 808.2 ppbv and N_2O at 273.0 ppbv and quantify the seasonal and hemispheric gradients of surface mixing ratios. Compared to
38 earlier intercomparisons, the stronger implied radiative forcing in the northern hemisphere winter (due to the latitudinal
39 gradient and seasonality) may help to improve the skill of climate models to reproduce past climate and thereby reduce
40 uncertainty in future projections.

1   Introduction

42   The burning of fossil fuels, emissions related to deforestation and agricultural activities and synthetic greenhouse gas emissions

43   are the reasons for the observed increases in greenhouse gas concentrations. Those elevated greenhouse gas mixing ratios in

44   turn cause more than the observed recent climate change as some of the warming effect is dampened by aerosols (Fig. TS.10

45   in IPCC WG1 AR4 (IPCC)). An accurate quantification of anthropogenic and natural climate drivers is crucial for general

46   circulation and Earth System models. Simulations by these models for the historical time periods, e.g. since 1850, can only be

47   meaningfully compared to observations (e.g. surface temperature, ocean heat uptake) to the degree that input forcings are an

48   accurate representation of the past. The difficulty with many anthropogenic drivers is that their global-mean magnitude, their

49   latitudinal gradient and seasonal cycle are uncertain further back in time, even for the main greenhouse gases carbon dioxide

50   (CO_2), methane (CH_4) and nitrous oxide (N_2O). Systematic observational efforts started in 1957-1958, measuring CO_2 at the

51   South Pole and Mauna Loa observatories. Measurements of archived air, and firn air and ice cores from both polar regions

52   provide records for the pre-observational time. To date, there have been few attempts to reconstruct long-term global-mean

53   timeseries based on ice and firn data, e.g. for CO_2 over the last millennia (MacFarling Meure et al. 2006, Ahn et al. 2012,

54   Rubino et al. 2013) or to provide latitudinally-resolved, monthly background mixing ratios of CO_2, CH_4 and N_2O over the

55   instrumental record over the past 20 to 40 years (Cooperative Global Atmospheric Data Integration Project 2013, NOAA ESRL

56   GMD 2014a, NOAA ESRL GMD 2014b, NOAA ESRL GMD 2014c). In light of the observational gaps further back in time,

57   some studies, such as Keeling et al. (2011), used linear regressions between fossil fuel use and latitudinal CO_2 concentration

58   trends to separate natural from anthropogenically-induced effects, which allows to infer latitudinal gradients back in time.

59   In previous climate model inter-comparison projects (Meehl et al. 2005), global-mean concentrations have been prescribed

60   (Meinshausen et al. 2011a), with some models constraining internally generated fields of greenhouse gas mixing ratios to

61   match those global-mean values. Here, we update those global-mean and annual-mean greenhouse gas concentration time-

62   series for the historical period over years 0 to 2014, with 'historical' simulations in the CMIP6 model intercomparison (Eyring

63   et al. 2016) focussed on the most recent period 1850 to 2014. In addition, we provide hemispheric and latitudinal monthly-

64   resolved fields for 43 greenhouse gases in total. In the past, the large latitudinal and seasonal gradient of greenhouse gas

65   radiative forcing has not been consistently applied to model radiative forcing and climate change. Our new dataset provides a

66   more consistent starting point for climate model experiments. The monthly and latitudinal resolution of this new greenhouse

67   gas dataset is in line with monthly solar forcing (Matthes et al. 2016) and monthly and latitudinally resolved ozone and aerosol

68   abundances. Many greenhouse gases also have significant longitudinal (land/ocean) and diurnal variations but we do not

69   attempt to resolve these. Neither do we provide vertical gradients of the greenhouse gases mixing ratios and only discuss

70   possible vertical extension methods (4.1) in case that models do not have their own methods to derive vertical gradients.

71   In this study, we compile one possible reconstruction of latitudinally and monthly resolved fields, as well as global annual

72   means of surface greenhouse gas mixing ratios for 43 gases from Year 0 to 2014, as input for the forthcoming model inter-

73   comparison experiments that are part of the Phase-6 Coupled Model Inter-comparison project (CMIP6) (Eyring et al. 2016),

74   specifically the pre-industrial control runs at 1850 forcing levels (picontrol), the experiment with abruptly quadrupled CO_2

75   concentrations (abrupt4x), and the standard experiment of a 1% annual CO_2 concentration increase (1pct2co2) as well as the

76   historical runs that are driven with best-guess estimates of historical forcings since 1850. Species that are radiatively less

77   important than CO_2, CH_4 and N_2O ('importance' here being measured as radiative forcing exerted in year 2014 compared to

78   1750) are provided individually as well in aggregate as HFC-134a and CFC-12 equivalent mixing ratios.

79 The design principle for this long-term dataset is to provide a plausible reconstruction of past greenhouse gas mixing ratios to

80 be used in climate models. Using various gap-filling procedures, reconstruction and extensions, this dataset aims to reflect

81 observational evidence of both recent flask and *in situ* observations from the worldwide network of NOAA ESRL and AGAGE

82 stations, as well as the Law Dome and Greenland ice core and firn data over the last two thousand years, where available.

83 Furthermore, many detailed literature studies (Mühle et al. 2010b, Arnold et al. 2013, Velders et al. 2014, Vollmer et al. 2016)

84 for radiatively less important species are taken into account and synthesised where direct observational records from the above

85 networks were not available.

86 The predominant climate effect of greenhouse gas increases is captured by the global- and annual mean mixing ratios

87 throughout the atmosphere. The surface global and annual mean mixing ratios provided here, in combination with the models'

88 approximations for the vertical concentration profile, are the minimum standard for CMIP6 models. Assimilating a latitudinally

89 and seasonally resolved data product serves two purposes. On the one hand, deriving the global and annual means from sparse

90 observations rests on knowledge or assumptions about spatial and seasonal distributions. Secondly, a more resolved dataset

91 will open the opportunity for some modelling groups to go beyond the prescription of global and annual mean mixing ratios.

92 Undoubtedly, some of the assumptions stretch into unknown territory, such as the seasonality of the CO_2 mixing ratios in pre-

93 observational times or the time-variability of latitudinal gradients, let alone the higher frequency fluctuations of global-mean

94 mixing ratios during the time, when only ice core data are available. Errors in the historical forcing do propagate and can

95 hinder the comparison between observations and models. This study therefore had to find a workable compromise between

96 providing a complete dataset that covers the whole time and space domain and being as close as possible to sparse observations.

97 Hence, the remaining uncertainties in concentration gradients should be kept in mind, although they might not be of primary

98 concern in regard to the inter-comparison aspect of the multi-model ensemble runs. Thus, while our CMIP6 community dataset

99 will improve on the global- and annual-mean time-series prescribed for the last set of CMIP5 experiments on a number of key

100 aspects, many research questions remain open.

101 The underlying reason for meridional gradients of annual-mean mixing ratios is manifold (Keeling et al. 1989a, Keeling et al.

102 1989b, Tans et al. 1989). For one, the sources of anthropogenic greenhouse gases from fossil fuel burning and cement

103 production or industrial activities are not evenly distributed with latitude, but concentrated in the mid-northern land masses. In

104 the case of CO_2, emissions from deforestation are not uniformly distributed with latitude either. The pattern of land use-related

105 emissions is even less stationary, with CO_2 uptakes and sources predominantly focussed in the mid-northern latitudes up until

106 earlier in the 20th century, shifting more towards lower latitudes in recent decades (Hurtt et al. 2011). This study uses an

107 approach based on simple regressions that implicitly rest on the assumption of a fixed pattern approximation (such as Keeling

108 et al. 2011). One complication to retrieve the latitudinal pre-industrial CO_2 concentration profile is that CO_2 fertilization and

109 temperature effects on the carbon cycle are changing both magnitude and spatial patterns of natural CO_2 fluxes. Lastly, both

110 the diurnal and seasonal cycle of photosynthesis and its covariance with vertical atmospheric mixing can have a pronounced

111 effect on measured surface mixing ratios (the so-called 'rectifier' effect), increasing northern hemispheric CO_2 mixing ratios

112 by up to 2.5 ppmv (Denning et al. 1999).

113 In order to dissect and analyse the different causes for temporal and spatial heterogeneity in surface mixing ratios, a rich body

114 of literature analyses observed latitudinal and seasonal gradients with various inversion techniques. Recent research provides

115 a clearer picture in regard to the root causes of the change in seasonality of CO_2 mixing ratios (Forkel et al. 2016), a topic

116   researched already in 1989 (Kohlmaier et al. 1989) based on the CO_2 fertilization effect on northern hemispheric terrestrial

117   biota. Generally, the research into meridional and seasonal variations employs various atmospheric inversion techniques

118   (Enting and Mansbridge 1989, Enting and Mansbridge 1991, Enting et al. 1995, Enting 1998, Rayner et al. 1999) to match

119   observed mixing ratios with source and sink pattern estimates (Keeling et al. 1989a, Keeling et al. 1989b, Tans et al. 1990a,

120   Enting et al. 1995, Rayner et al. 1999, Gurney et al. 2002, Gurney et al. 2003, Gurney et al. 2004, Baker et al. 2006, Peylin et

121   al. 2013). Similarly to CO_2, the spatial variation in CH_4 mixing ratios is used for model synthesis inversions (Fung et al. 1991).

122   There is a substantial lack of observational evidence of both seasonality and latitudinal CO_2 gradients in pre-industrial times.

123   Given that atmospheric CO_2 is not well preserved in the Greenland ice (Anklin et al. 1995, Barnola et al. 1995), the pre-

124   observational north-south gradient cannot be calculated from the Greenland and Antarctic ice core records. Alternatively,

125   understanding biospheric sink and source dynamics could provide vital evidence to infer pre-industrial surface concentration

126   patterns. In this study, we do not employ any such inversion models or results, and only note that our pre-industrial meridional

127   and seasonal variations should be regarded as highly uncertain. However, some plausibility of the CO_2 gradients is gained by

128   comparison with some model studies (Discussion). High-latitude records of CH_4 and N_2O are available from both hemispheres

129   (Fluckiger et al. 2002, Schilt et al. 2010b, Rhodes et al. 2013) allowing to estimate pre-industrial large-scale concentration

130   gradients.

131

2   Methods

132

133   In order to pursue the primary purpose of this study, namely the provision of a consistent set of historical surface greenhouse

134   gas mixing ratios, a number of analytical steps were taken to assimilate the observational data. Although global-mean and

135   annual mean mixing ratios are of primary interest, the discussion covers latitudinal and seasonal variations in part because the

136   assimilation procedure for sparse observational data does require accounting for this spatio-temporal heterogeneity in order to

137   derive global and annual means.

138   We consider a total of 43 greenhouse gases in this study, namely CO_2, CH_4, N_2O, a group of 17 ozone depleting substances,

139   namely CFC-12, CFC-11, CFC-113, CFC-114, CFC-115, HCFC-22, HCFC-141b, HCFC-142b, CH_3CCl_3, CCl_4, CH_3Cl,

140   CH_2Cl_2, $CHCl_3$, CH_3Br, Halon-1211, Halon-1301, Halon-2402, and 23 other fluorinated compounds, namely 11 HFCs (HFC-

141   134a, HFC-23, HFC-32, HFC-125, HFC-143a, HFC-152a, HFC-227ea, HFC-236fa, HFC-245fa, HFC-365mfc, HFC-43-

142   10mee), NF_3, SF_6, SO_2F_2, and 9 PFCs (CF_4, $C2F_6$, C_3F_8, C_4F_{10}, C_5F_{12}, C_6F_{14}, C_7F_{16}, C_8F_{18}, and c-C_4F_8).

2.1   Summary of assimilation approach.

144   We perform three consecutive steps to synthesize the global mixing ratio fields over the full time horizon from year 0 to year

145   2014. First, we aggregate the available observational data over a recent instrumental period. Second, we estimate three

146   components of the global surface mixing ratio fields from these data, namely global mean mixing ratios, latitudinal gradients

147   and seasonality. Thirdly, we extend those components back in time with – *inter alia* – ice-core or firn data. The full historical

148   GHG concentration field can then be generated by the time-varying components.

149   Under this basic assimilation model, the concentration $\hat{C}(l,t)$ at any point in time t and in a latitudinal band l can be written

150   as:

151    $$\hat{C}(l,t) = \overline{C_{global}}(t) + \hat{S}_{l,m}(y) + \hat{L}_l(y) \qquad (1)$$

152   Where $\overline{C_{global}}(t)$ is the global-mean mixing ratio at time t, and $\hat{S}_{l,m}$ is the seasonality in each latitude l and month m, and

153    $\hat{L}_l(y)$ is the latitudinal annual-mean deviation in year y at latitude l. With this assimilation model, and the optimal low rank

154   approximations of seasonality and latitudinal gradients, a regularisation of the data is performed by a principal components

155   analysis, which creates a certain degree of robustness against data gaps or outliers. Other methods, like a harmonic

156   representation of station data, have, in principle, a similar smoothing and regularisation effect (Masarie and Tans 1995),

157   although quantitative differences exist (section 5.3).

158   A detailed data flow diagram of how the historical greenhouse gas mixing ratios are derived in this study is provided in Figure

159   22. The subsequent section will describe the method step-by-step, as indicated by the green circles in Figure 22.

2.1.1   Step 1: Aggregating raw station data.

161   Atmospheric measurements are taken in remote environments or locations that are closer to pollution sources, in continental

162   or marine areas, at different times of the day or night, at different altitudes, and different seasons of the year, often using

163   different calibration scales. This poses challenges for any synthesis of observational data.

164   The observational station data over the recent decades used in this study are predominantly sourced from the networks operated

165   by NOAA (Earth System Research Laboratories: ESRL), and AGAGE. In general, we use monthly station data provided by

166   the respective networks as a starting point. In the case of the AGAGE network, monthly averages are provided with and without

167   pollution events. We chose the monthly averages that include pollution events (file-endings '.mop', with the exception of

168   CH_2Cl_2, in which case data issues warranted the use of monthly station averages without pollution events). The approach that

169   we do not restrict our source data to background conditions is consistent with our approach elsewhere – and the NOAA network

170   monthly station averages - which do not screen out pollution events (although the dominant number of NOAA flask

171   measurements might be slightly biased towards background conditions rather than pollution events). In total, CO_2 data from

172   81 stations from the NOAA flask network, and 3 stations from the NOAA *in situ* data stations are used (Table 2). For CH_4, 87

173   sampling stations from the NOAA flask network and 5 stations from the AGAGE *in situ* network are compiled (Table 8). For

174   N_2O, data from flask and in situ measurements at 13 stations of the NOAA HATS global network are combined with data from

175   5 stations from the AGAGE network (Table 9). For other gases, the AGAGE and NOAA coverage and timeframes vary, with

176   individual station's codes provided in panels f of the individual gases' factsheets (Figure 23 to Figure 62). The complete

177   AGAGE network is further described in Prinn et al. (2000a), with specific information for CFC-11 and CFC-12 provided in

178   Cunnold et al. (1997), CH_3CCl_3 in Prinn et al. (2001, 2005) and Reimann et al. (2005), CCl_4 in Simmonds et al. (1998), CFC-

179   113 in Fraser et al. (1996), $CHCl_3$ in O'Doherty et al. (2001), CH_3Br and CH_3Cl in Simmonds et al. (2004) and Cox et al.

180   (2003), and HFC-134a, HCFC-141b, HCFC-142b and HCFC-22 in O'Doherty (2004) and Miller et al. (1998).

181   Calibration scales, i.e. the standardized gas mixtures that allow to calibrate the instrumentation used for in-situ or flask

182   measurements, are different between the NOAA and AGAGE networks. While we use the station data that has already been

183   converted to the latest scales of the respective networks, some older comparison data products use previous scales (as the one

184   published in the latest ozone assessment report (WMO 2014)). Thus, where necessary, we convert those older data to the newer

185   scales. For 7 gases, we use scale conversion factors to convert to the SIO14 scale, specifically 1.0826 for HFC-125 (from

186   University of Bristol scale: UB98), 1.1226 for HFC-227ea (from Empa-2005), 1.1970 for HFC-236fa (from Empa-2009-p),

187   and 1.1909 for HFC-245fa (from Empa-2005), 1.1079 for HFC-365-mfc (from Empa-2003), 1.0485 for HFC-43-10-mee (from

188   SIO-10-p), and 0.9903 for CH_2Cl_2 (from UB98), with all conversion factors taken from the Appendix in WMO (2012).

189   Apart from those scale conversions to the latest NOAA and SIO scales mentioned above, we only make sure that the three

190   main gases each are on a unified scaled. As we source all our CO_2 station data from the NOAA network, there is no scale

191   conversion necessary. In the case of CH_4, we account for different calibration scales by converting AGAGE CH_4 data (Tohuko

192   University scale) to the NOAA scale (NOAA04) (multiplication by 1.0003). Both the AGAGE (SIO1998) and NOAA network

193   calibration scales (NOAA-2006) for N_2O are compatible without the need for a conversion factor (WMO 2012).

194   Apart from those three main gases, we do not apply further scale conversions. Thus, given that our results are based on a

195   mixture of the AGAGE and NOAA networks, they are de facto a weighted average between the respective two standard scales

196   (SIO and NOAA) for each gas. The effective weight in this "weighted mean" depends on the station numbers and each

197   networks' station distribution given that our assimilation method implicitly weights stations less that are geographically close,

198   i.e. in the same latitude-longitude box. This mixture of scales is different from previous studies that either applied empirical

199   scale conversions (so that global-mean or station averages are identical) or used both scales in parallel to estimate a

200   measurement uncertainty error (WMO 2014), for example when estimating emission with inverse techniques. Mathematically,

201   our approach is similar to an approach, where a station-by-station scale conversion would be applied towards an intermediate

202   scale between NOAA and AGAGE. However, for some applications, this approach is clearly a limitation as it hides the

203   uncertainty and would for example warrant a new data assimilation if one network updates its scales (section 6). The reason

204 this "weighted mean" approach is chosen in the context of this study is that we intend to reconstruct a single mixing ratio

205 history making use of the station data from both major measurement networks without giving preference to the one or other

206 measurement scale. Given that scale differences amount to generally below 2% differences, often for radiatively less important

207 substances, this "middle of the road" approach seems justified given the other uncertainties in climate models (vertical

208 distributions, radiative forcing routines, other radiative forcings such as aerosols). Any conversion to a single scale would ease

209 comparisons, but would not be able to address the inherent measurement uncertainty, and might even face a stronger bias

210 (assuming that the two scales SIO and NOAA are equally plausible representations of the "truth") (see limitations).

211 In regard to the time of the day, month or year, we do however not apply interpolation or adjustment techniques other than a

212 simple monthly binning of all available data. The spatial and temporal coverages of the raw data used in this study are depicted

213 in Figure 17, Figure 18, and Figure 19 for CO_2, CH_4 and N_2O data, respectively.

2.1.2   Step 2-4: Binning and spatial interpolation

215 We employ a simple monthly mean binning of all available data, separately averaged for each station. In each latitudinal /

216 longitudinal box, all available monthly mean station data are averaged, with the mean being assigned to the grid box centre

217 before employing a 2-dimensional spatial interpolation to extend available data points to longitudinal and latitudinal grid points

218 that do not have observed data for any particular month. Our method provides equal weight to each station within a longitude-

219 latitude box, no matter whether the station reports a few flask measurement samples or sub-hourly *in situ* instrument readings.

220 The chosen assimilation grid has 72 boxes with 12 equal-latitude bands of 15 degrees and 6 longitudinal bands of 30 degree.

221 Following the temporal monthly binning and subsequent spatial linear interpolation, we average all data across the longitudes

222 to obtain 12 latitudinally resolved monthly time series of surface mixing ratios.

2.1.3   Step 5: Global mean mixing ratios

224 The annual-global mean concentration $\overline{C_{global}}(y)$ is simply derived as the area-weighted arithmetic mean of the binned

225 latitudinal data (grey small "5" in Figure 22). In addition to the annual global mean, a time series of monthly values is derived

226 as a smooth spline interpolation between the annual data points, with the constraint of being mean-preserving, i.e. that the

227 average of the 12 monthly values is again the global annual average value initially-derived. Thus, the trend in the mixing ratio

228 data is reflected in the global-mean time series from month to month.

2.1.4   Step 6: Latitudinal Gradient

230 The annual-mean latitudinal gradients are derived as first and second EOFs from the annual-average residuals per latitude after

231 subtracting the global annual mean (step 6 in Figure 22). Let G be the n x m matrix of n years with observations, and m

232 latitudinal boxes, then G can be decomposed into its EOFs and scores by calculating the singular value decomposition of G =

233 UDV^T, where U and V are orthogonal matrices in $\mathbb{R}n$ and $\mathbb{R}m$, respectively, and D is the nxm matrix with non-zero elements

234 only on the diagonal. EOFi is the ith column of V, and the score Si(y) of EOFi in year y is given as the (y,i) entry of the UD

235 matrix. In other words, the EOFs are the eigenvectors of the gram matrix 1/m*G'G and the scores are the projections of the

236 observations G onto the EOFs.

237 Those EOF scores are regressed with suitable predictors or extended constantly. Thus, the term $\hat{L}(y)$ is the optimal low rank

238 approximation of the latitudinal deviations from the global mean over time y. The leading EOF of latitudinal annual-mean

239 variation multiplied with the observed or regressed score S of that year y.

240     $\hat{L}(y) = \sum_{i=1}^{imax} EOF_i * S_i(y)$ (2)

241   with *imax* being 1 or 2 if only the leading or the two leading EOFs are taken into account, respectively.

2.1.5   Step 7-10: Seasonality

243   The seasonality fulfils the condition that the sum of seasonal variations at each latitude is zero over the year, i.e.

244     $\sum_{m=1}^{12} \hat{S}_{l,m} = 0$ (3)

245   This seasonality $\hat{S}_{l,m}(t)$ at time t is calculated as the relative seasonality $\frac{d\hat{S}_{l,m}}{dC_{global}}$, i.e. the seasonal deviation in mole fraction

246   divided by the global-mean mole fraction, multiplied by the global-mean mixing ratio at time t (step 7 and 10 in Figure 22).

247   An exception is the case of CO_2 (step 8 and 9 in Figure 22). In this case, the seasonality pattern over the observational period

248   is held fixed as mole fractions, i.e. not relative to the global mean. However, the residuals between this fixed seasonality and

249   the seasonality, which is derived from the observations by subtracting the latitudinal averages, is used for a singular value

250   decomposition. Let $R_{l,m}(t)$ be the residuals at latitude l and month m at time t, the optimal lower rank representation of this

251   seasonal change is then given by the first EOF of the gram matrix 1/n*R'R with n being the number of observational data

252   points. The derived score, i.e. the projection of the residuals onto the first EOF, is regressed against a time series P, a composite

253   of global-mean CO_2 concentration and historical observed global-mean surface air temperatures. This simplified choice is

254   taken as previous studies identified warmer temperatures and elevated CO_2 mixing ratios as dominant reason for increased

255   seasonality (Graven et al. 2013, Forkel et al. 2016, Welp et al. 2016) although anthropogenically induced cropland productivity

256   increases are suggested to play also some role (Gray et al. 2014). Specifically, P is assumed as a composite of the product and

257   the sum of normed global-mean surface air temperature and normed CO_2 mixing ratio deviations from pre-industrial levels.

258   The temperature and mixing ratio deviations are normalized such that the 2000-2010 deviation from the 1850-1880 base period

259   is set to one. Thus, the regressor P can be described as:

260     $P(t) = \frac{\Delta T(t) * \Delta C(t)}{2} + \frac{\Delta T(t) + \Delta C(t)}{2}$ (4)

261   With ΔT being the normed temperature deviation from the 1850-1880 period, specifically

262     $\Delta T(t) = \left. \left(T(t) - \sum_{t=1850}^{1880} T(t) \right) \middle/ \sum_{t=2000}^{2010} \left(T(t) - \sum_{i=1850}^{1880} T(i) \right) \right.$ (5)

263   And ΔC being synonymously the normed mixing ratio deviation. Note that this regressor P is one of multiple options that were

264   tested and could be regarded as a plausible regressor for seasonality changes. However, given that seasonality changes in the

265   case of CO_2 depend on a complex interaction of CO_2 fertilization of temperate, seasonal gross primary productivity, as well as

266   the influence of temperature, precipitation on biomass growth and respiration, this extension of the observed seasonality

267   changes beyond the observational period is just that: a plausible extrapolation that needs to be refined by further and research

268   to replace this study's *ad hoc* assumption.

269   The empirical seasonality of CH_4 and N_2O over the observational time period is found to be closely approximated by our

270   default assumption of a seasonality that is proportional to global mean mixing ratios. For a number of substances, however,

271 seasonality has been assumed to be zero – either because the diagnosed seasonality was very small or due to a lack of
272 observational data.

2.1.6   Step 11-13: Extension of latitudinal gradients and global means with ice core and firn data

274 Historical GHG records from ice and firn provide high-latitude estimates of atmospheric greenhouse gas mixing ratios before
275 the instrumental record from air sampling stations. We rely mainly on the Law Dome (Etheridge et al. 1998b, MacFarling
276 Meure et al. 2006, Rubino et al. 2013) and, for CH_4, Greenland NEEM ice core data (Rhodes et al. 2013). Although we did
277 not directly use their data, we acknowledge multiple other efforts, including, but not limited to Mitchell et al. (2013), and
278 Bauska et al. (2015), Schilt et al. (2010b), Flueckiger et al. (2002), and Sowers et al. (2003) (Figure 1). Law Dome atmospheric
279 composition records have the advantage of a very narrow air age spread that provides measurements with high temporal
280 resolution and mean air ages up to the 1970s, where they overlap with the beginning of atmospheric observations for many
281 gases. The Law Dome data used here have been updated for minor dating changes and upgrades to NOAA scales (Rubino et
282 al., 2013; http://www.esrl.noaa.gov/gmd/ccl/index.html).

283 Having obtained estimates of the latitudinal gradients over the observational period and having derived approximations back
284 in time by regressing latitudinal gradients EOF scores with emissions (step 11 in Figure 22), this allows estimating global
285 mean mixing ratios based on the Law Dome data in the case of both CO_2 and N_2O (step 12 in Figure 22). In the case of CH_4,
286 the advantage is that there are northern hemispheric data points available from NEEM (Greenland) (Rhodes et al. 2013) that
287 complement the Law Dome record over the past 2000 years. This NEEM record hence allows an optimisation of both the EOF
288 scores and global means at past time points to match both the Law Dome and NEEM records (step 13 in Figure 22). Some data
289 periods with gaps in the NEEM record are filled by linearly interpolating the optimised EOF scores of the latitudinal gradient.
290 With an interpolated EOF score, the global-mean mixing ratio can then be directly inferred from the Law Dome record. All
291 optimisations are performed by minimising area-weighted squared residuals.

292 The Law Dome ice core data are smoothed with a piecewise local 3rd degree polynomial median regression, using ad hoc
293 expert judgement assumptions of errors and smoothing window widths specific to each gas in order to approximately reflect
294 their long-term median evolution. In the case of CO_2, a random error of 2 ppmv was assumed, a percentage age error (60 years
295 at age 2000 years before present) with a bagging of 250 ensembles, a kernel width of 120 years, minimal number of data points
296 of 7 and maximum of 25 (panel a in Figure 6). Likewise, CH_4 Law Dome data ice core data are smoothed with a 3rd degree
297 polynomial median regression with a maximum kernel width of 100 years, 4 minimal data points (a constraint that overwrites
298 the maximum kernel width, if necessary) and 10 maximal data points. Like for CO_2, 250 ensembles were averaged, after adding
299 noise of 3ppb, and an age uncertainty of 50 years for 2000 years. For N_2O, a kernel width of 300 years was chosen with a
300 minimum number of 7 and maximum number of 15 data points to be included in the piecewise 3rd degree polynomial
301 regression. As for CO_2 and CH_4, 250 ensembles were used for bagging after injecting a random noise of 3 ppbv and an age-
302 dependent x-axis uncertainty of 90 years per 2000 years.

303 The Greenland NEEM ice core CH_4 data (Rhodes et al. 2013) exhibits some outliers in the recent period (Figure 1d) due to
304 incursion of modern air into still-open pores of shallow ice. Spikes in deeper ice are likely due to impurities. Hence, we use
305 the 5-year smoothed data provided by Rhodes et al. (2013) as a proxy for atmospheric background mixing ratios. We dated the
306 NEEM firn air samples (Buizert et al. 2012) using the effective age procedure as in Trudinger et al. (2002) with the ages

307   published in Gosh et al. (2015), with a small correction to the NOAA 2006 scale data applied for gravity effects (as applied in

308   other ice and firn data), using here only firn samples from the 2008 campaign.

2.1.7   Step 14: Extension of latitudinal gradients and global means with literature data

310   For several gases, including ozone depleting substances, halons and PFCs, the available AGAGE and NOAA station data is

311   sparse spatially. Before the start of systematic instrumental measurements, we use literature studies which make use of various

312   data sources, such as air sample archives or firn records (step 14 in Figure 22). Specifically, if a global mean is provided, we

313   use that global mean in conjunction with our derived and regressed latitudinal gradients. In case of hemispheric data-points,

314   we adapt the latitudinal gradient to match the literature studies, as in the case of C_4F_{10}, C_5F_{12}, C_6F_{14}, C_7F_{16} or C_8F_{18}, where we

315   based both the global mean and latitudinal gradients on the data of Ivy et al. (2012). Other key studies used were Velders et al.

316   (2014), the data underlying the WMO Ozone Assessment Report (2014), Arnold et al. (2013, 2014), Trudinger et al. (2004),

317   Mühle et al. (2009, 2010a), Montzka et al. (2011), updated time series by Montzka et al. (1999) (updated at:

318   ftp://ftp.cmdl.noaa.gov/hats/Total_Cl_Br/), the recent Halon study by Vollmer et al. (2016) and PFC study by Trudinger et al

319   (2016), as indicated in the gas-specific factsheet figures (Figure 23 to Figure 62). In the case of N_2O and CH_2Cl_2 we assumed

320   a constant latitudinal gradient back in time before ongoing measurement records are available (Figure 5, and Figure 29,

321   respectively).

2.1.8   Step 15: Extrapolation

323   For some limited data segments, an extrapolation has been used. Either a piecewise smoothing spline to converge mixing ratios

324   back to zero or pre-industrial background mixing ratios, e.g. before the WMO (2014) or Velders et al. (2014) data started.

325   Furthermore, a linear extrapolation was applied, when there were not sufficient 2014 data available.

2.1.9   Step 16-19: Creating the composite surface mixing ratio field

327   Following equation (1), the surface mixing ratio fields over the full time span are now synthesized from the lower rank

328   representations of seasonality, latitudinal gradient and the smooth monthly representation of global mean mixing ratios. As per

329   the original station data aggregation, the latitudinal resolution is 15 degrees and time resolution is monthly. In order to assist

330   the application in climate models with finer grids, we produced also a finer grid interpolation to 0.5 degree latitudinal resolution

331   using a mean-preserving smoothing. This finer grid interpolation should not be mistaken as mixing ratio field containing actual

332   information at 0.5 degree level. The purpose is simply to offer a smooth interpolation that avoids errors that will arise from,

333   e.g., a linear interpolation between the provided 15 degree latitude points, as the mean across those (linearly) interpolated

334   values, would not match the original field. The mean-preserving smoothing code is available from the authors on request.

335   Finally, the 15 degree fields are aggregated towards global, northern and southern hemisphere monthly and annual means.

2.1.10   Step 20: Aggregating equivalent mixing ratios

337   It is computationally inefficient to model the radiative effect of 43 individual greenhouse gases in today's Earth system models

338   or general circulation models. Climate models use different pathways to approximate the radiative effects of the full set of

339   greenhouse gases. As one strategy, only the radiatively-major greenhouse gases are explicitly modelled, such as CO_2, CH_4,

340   N_2O, CFC-12, CFC-11, which together cause 94.5% of GHG warming effect (measured in radiative forcing) in 2014 rel. 1750

341   and 98% of the total radiative effect compared to the full set of 43 GHGs (Table 10). Alternatively, radiatively-minor GHGs

342   can be approximated by equivalent greenhouse gas concentrations of a marker gas. In this way, the radiative effect of the group

343   of gases is expressed by a single gas mixing ratio. One definitional issue is whether the radiative forcing since 1750, i.e. only

344   the changes since pre-industrial levels, are expressed by the marker gas (here called 'marginal equivalence' $C_{eq,i}$). In this case,

345   the marker gas' concentrations $C_{eq,i}$ are sought that would exert the same aggregate radiative forcing since 1750 as the group

346   of summarized gases. Thus, let Cj(t) be the concentration (volumetric or mole mixing ratio) of a greenhouse gas and $C_{0,j}$ the

347   pre-industrial level, i.e. in year 1750 that is routinely used as base year for radiative forcing (IPCC 2013). A marker equivalence

348   mixing ratio by gas C_{eq1} for group Cj with j = 1,…n is then given by:

349    $$C_{eq,i}(t) = R_i^{-1}\left(R_i(C_{0,i}) + \sum_{j=1}^n \left(R_j\left(C_j(t)\right) - R_j\left(C_{0,j}\right)\right)\right) \qquad (6)$$

350   With Rj(C) being the radiative forcing function relating mixing ratios C(t) at time t to radiative forcing for gas j, in the linear

351   case $R_j(C) = C * E_j$ with Ej being the radiative efficiency. $R_i^{-1}(F)$ is the inverse of this radiative forcing function, so that the

352   mixing ratio C that corresponds to a forcing F is given by $C = R_i^{-1}(F)$.

353   In contrast, equivalent mixing ratios can express the radiative effects of the summarized greenhouse gases including their

354   natural background levels (here called 'full equivalence' $C'_{eq,i}$).

355    $$C'_{eq,i}(t) = R_i^{-1}\left(\sum_{j=1}^n R_j\left(C_j(t)\right)\right) \qquad (7)$$

356   While the former definition 'marginal equivalence' is often used to express the total greenhouse gas forcing in CO_2 equivalence

357   mixing ratios, the latter 'full equivalence' is the more appropriate quantity to drive climate models, given that natural

358   background mixing ratios of not-explicitly considered gases should nevertheless exert a radiative effect even in a pre-industrial

359   control, even though that radiative effect does not count under a radiative forcing definition that looks at changes from 1750.

360   In the linear case, in which case radiative forcing is proportional to the gas' mixing ratios, equation (7) can be written as:

361    $$C'_{eq,i}(t) = \frac{\sum_{j=1}^n r_j^{eff} * C_j(t)}{r_i^{eff}} \qquad (8)$$

362   With r_i^{eff} being the radiative efficiency of the gas I in W/m^2 per ppbv.

363   Thus, climate models have the option to reduce the complexity of 43 GHGs and the associated computational burden by

364   reducing the number of GHGs that are taken into account. With the top 5 GHGs, CO_2, CH_4, N_2O, CFC-11 and CFC-12, climate

365   models would capture 98% of the total radiative effect in year 2014 and 94.5% of the radiative forcing since 1750, i.e. the

366   change of the radiative effect between 1750 and 2014 (see Table 10). As alternative, there is the option to use equivalent

367   mixing ratios. For two such equivalence options, this study provides input data sets. Modelling groups should indicate the

368   combination of files they employed:

369   a)   **Option 1**: Climate models implement a subset of 43 greenhouse gases.

370   b)   **Option 2**: Climate models implement the four most important GHGs with their actual mixing ratios explicitly,

371   namely CO_2, CH_4, N_2O and CFC-12 and summarize the effect of all other 39 gases in an equivalence mixing ratio

372   of CFC-11. For this purpose, we provide CFC-11-eq mixing ratios ('full equivalence').

373   c)   **Option 3**: Like option 2, but with a different split up of gases other than CO_2, CH_4 and N_2O. Climate models

374   implement the three most important GHGs with their actual mixing ratios explicitly, namely CO_2, CH_4, and N_2O

375 and summarize the radiative effect of the ozone depleting substances in a CFC-12-eq mixing ratio and the radiative

376 effect of all other fluorinated gases as a HFC-134a-eq mixing ratio. For this purpose, we provide CFC-12-eq and

377 HFC-134a-eq mixing ratios ('full equivalence').

378

2.2 Data analysis for comparisons

380 We compare our results to a number of comparison products, namely the CO_2 fields from CMIP5 Earth System Models

381 (ESMs). Here, we briefly describe the analytical steps that we performed for retrieving the CMIP5 ESM data.

382 Analyzed are ten CMIP5 ESMs models that have an interactive carbon cycle model and provided the mole fraction of carbon

383 dioxide in the air as function of different pressure surfaces for the *esmhistorical* experiment. We diagnosed those *esmhistorical*

384 experiments in terms of the simulated CO_2 mixing ratio at surface pressure (1bar = 100000 Pa) for 10 CMIP5 ESM models,

385 for which data were available: (1) BNU-ESM (BNU, China), (2) CanESM2 (CCCMA, Canada), (3) CESM1-BGC (NSF-DOE-

386 NCAR, USA), (4) FIO-ESM (FIO, China), (5) GFDL-ESM2G (NOAA GFDL, USA), (6) GFDL-ESM2M (NOAA GFDL),

387 (7) MIROC-ESM (MIROC, Japan), (8) MPI-ESM-LR (MPI, Germany), (9) MRI-ESM1 (MRI, Japan), (10) NorESM1-ME

388 (NCC, Norway). For the models CanESM2, MIROC-ESM and MPI-ESM-LR more than one realization is available. We

389 calculated an ensemble mean based on the all available ensemble members. The climatological seasonal cycle (Figure 13,

390 Figure 14) is calculated relative to the linear trend of the corresponding 30-year periods.

391

3 Results

Here, we describe the historical mixing ratios of the main greenhouse gases and provide a fact sheet for all 43 individual gases.

3.1 Carbon Dioxide

The 800-thousand-year EPICA composite ice-core record (Lüthi et al. 2008) indicates that CO_2 mixing ratios have fluctuated between 170 and 270ppmv (Figure 1a) in conjunction with glacial- and inter-glacial temperature variations. From the year 0 to 1000, our piecewise fit of the 3rd degree polynomial of Law Dome ice core data allows a derivation of global mean mixing ratios of around 278.6 ppmv (min-max range of 277.0 to 280.2 ppmv).

Our smoothed Law Dome results do not reflect the higher frequency variations suggested by the individual data points ((Etheridge et al. 1996, MacFarling Meure et al. 2006, Rubino et al. 2013) and are comparable to the frequency spectrum that would result from a smoothed median estimate of WAIS data by Bauska et al. (2015) and Ahn et al. (2012). The WAIS record is generally 3-6 ppmv higher than the Law Dome record and is also higher than South Pole and EPICA DML ice cores (Ahn et al. 2012). The cause for this difference is not yet known (Figure 1b). In terms of the various possible frequency spectra, modelling groups might want to test an alternative data set that captures those higher frequency characteristic of the Law Dome record (data can be generated by the authors on request). In that higher frequency data set, the minimum of global mean CO_2 mixing ratios is close to 270 ppmv around the year 1615. The smoother version now provided for CMIP6 has its minimum in year 1666 at 276.27 ppmv (Figure 1b). The reason for the 1610 dip in the Law Dome record and why this does not show in the WAIS record is not yet fully understood. The current understanding of how the age kernel is different for the two sites cannot yet explain this difference in mixing ratios around 1610.

In regard to the latitudinal gradient, we explored various options. If we regress the first EOF of the latitudinal gradient (Figure 2d) against global fossil CO_2 emissions, the pre-industrial latitudinal minimum of surface CO_2 mixing ratios would be estimated in the mid-northern latitudes (approximately 1.8 ppmv below the global-mean), where the maximum was observed in recent decades (e.g. 4.8 ppmv above the global-mean in 2010). Previously a similar regression approach between mixing ratios and CO_2 emissions was used by Keeling et al. (2011) to separate the anthropogenic from the natural component in the mixing ratio difference between Mauna Loa and the South Pole. While this approach is not perfect due to the covariance of regional fossil fuel emissions with natural sinks over the same period, different patterns of anthropogenic land-use emissions, and a latitudinal gradient component that merely results from seasonal CO_2 exchange (e.g. Denning et al. 1995), it can nevertheless provide a first indication of the influence of anthropogenic emissions on the latitudinal gradient. Furthermore, this approach would have resulted in an approximately 0.4 ppmv higher pre-industrial Antarctic CO_2 mixing ratios compared to the global mean coinciding with the assumption taken by Rubino et al. (2013).

However, given the evidence by CMIP5 ESM models of a slight tropical local maximum (Figure 2b) and large uncertainties with regard to pre-industrial sinks and source distributions and hence the latitudinal gradients of CO_2, we assumed a zero pre-industrial latitudinal gradient. Thus we performed a zero-intercept regression of the latitudinal gradient EOF1 with global fossil CO_2 emissions and converging the score of the second EOF towards zero, resulting in a flat latitudinal gradient in pre-industrial times.

The second EOF of the latitudinal gradient of CO_2 does not exhibit the same linearity over time as the first EOF, and the reasons are currently unknown. Potential candidates for this pronounced spike of mid-northern latitude mixing ratios in the

428   case of CO_2 are a shift in station sampling locations with more 'polluted' land-station coming on line after 1995, the 'rectifier'

429   effect due to an enhanced seasonal cycle (Denning et al. 1995), and the rise of Chinese emissions (albeit the onset of the recent

430   surge in Chinese CO_2 emissions is often demarked to start slightly later, only by 2003 (Francey et al. 2013)). One suggested

431   explanation for this 2010 change in north-south gradients are changes in interhemispheric transport (Francey and Frederiksen

432   2016). Recently, i.e. after 2010, this spike in mid-latitude northern mixing ratios seemed to somewhat subside again according

433   to our analysis (see scores for EOF1 and EOF2 in Figure 2d). Future research could further investigate the underlying reasons

434   of this change in latitudinal patterns and a physical explanation will allow a more appropriate backward extension in time.

435   The diagnosed average seasonality of atmospheric CO_2 mixing ratios over the observational period reflects the standard carbon

436   cycle pattern of strong CO_2 uptake in spring and release in autumn due to photosynthesis and heterotrophic respiration in the

437   northern hemispheres ecosystems. Our EOF analysis of the residuals then shows (Figure 2a.2 and a.3) that the seasonality has

438   increased over recent decades in line with previous studies, which explore the link to increased ecosystem productivity (Graven

439   et al. 2013, Forkel et al. 2016, Welp et al. 2016) and increased cropland productivity (Gray et al. 2014). Specifically, our

440   analysis shows a slight shift of the seasonality to earlier months in the year, i.e. the negative and positive deviations of the EOF

441   pattern are shifted by a month compared to the average seasonality (cp. Figure 2a.1 and a.2). The strongest change in CO_2

442   seasonality is derived for the latitudinal bins centered around 37.5 to 67.5 degree north bins with a maximum strengthening of

443   negative deviations in the 52.5 degree north latitudinal band in July by around 4 ppmv over 1984 to 2013 (4 ppmv results from

444   multiplying the EOF pattern value in July in the 52.5-degree bin with the EOF score difference of around 10, see Figure 2a.2

445   and a.3). Although the maximum strengthening of the seasonal cycle happens in July in the 52.5-degree latitudinal band, the

446   maximum seasonal cycle deviation is still observed slightly later in August and extends also slightly more towards the northern

447   latitudes (Figure 2a.1).

448   In 1850, the start of the historical CMIP6 simulations, the estimated global-mean CO_2 mixing ratio is 284.32ppmv, rising to

449   295.67 ppmv in 1900, 312.82 ppmv in 1950, 369.12 ppmv in year 2000 up to 397.55 ppmv in 2014 (Table 7). Here and

450   elsewhere (e.g. Table 7) we provide more significant figures than customary - not to claim a 5-digit precision of the data (which

451   is not given), but to avoid unnecessary (even if small) step changes in mixing ratios between the pre-industrial run and the

452   historical and other runs. Variations in the increase of global-mean surface CO_2 mixing ratios are a slight flattening in the

453   1930s and then a stronger flattening during the World War II until the 1950s. The increase from 1970 onwards has a slightly

454   positive curvature (accelerating trend) with small deviations around 1973, 1981 and the temporary flattening of CO_2 mixing

455   ratios after the 1991 Pinatubo eruption (Jones and Cox 2001, Peylin et al. 2005) (Figure 2 and Figure 3).

456   **3.2   Methane**

457   Over the 800 thousand years before Year 0, atmospheric CH_4 mixing ratios varied between 348.7 ppbv and 728.4 ppbv

458   according to the EPICA ice core composite (Barbante et al. 2006, Loulergue et al. 2008, Capron et al. 2010) (Figure 1c and

459   Figure 4). The Law Dome record (Etheridge et al. 1998a, MacFarling Meure et al. 2006) indicates an onset of increasing

460   mixing ratios around the year 1720 (Figure 1d, and Figure 4). From Year 1850 with slightly higher than 800 ppbv mixing

461   ratios, a slight rise is observed until the 1950s, when CH_4 mixing ratios markedly increase first in the latter half of the 1950s,

462   then again from 1965 onwards. The Greenland firn and ice core data (Rhodes et al. 2013) are more difficult to interpret because

463   part of the record is affected by high frequency ice core CH_4 signals possibly of non-atmospheric origin. CH_4 spikes are

464   accompanied by elevated mixing ratios of black carbon, ammonium and nitrate, suggesting that biological *in situ* production

465   may be responsible – particularly in the later years of the record since 1940. Taking here the 5-yearly average measurement

466   values with outliers removed (Rhodes et al. 2013) that approximate the lower bounds of the raw data points until 1942, we can

467   then infer global gradients back in time and derive an estimate of global-mean mixing ratios. These global-mean mixing ratios

468   are estimated to be around 30 ppbv higher than the Law Dome record by 1850, with the difference growing to 45 ppbv by

469   1940s, increasing further from there (Figure 1d). This approximately matches the findings by Mitchell et al. (2013) of interpolar

470   differences between 35 and 45 ppbv since 400 BC.

471   Our analysis of CH_4 mixing ratios in the recent decades is based on a large number of stations (Table 8 and Figure 4f). While

472   the annual increase of global CH_4 mixing ratios slowed over the 1980s and markedly after 1992 towards stabilized mixing

473   ratios between 1999 to 2005, CH_4 increased again after 2006 at about 5.4 ppbv/yr (Figure 4f).

474   We retrieve a seasonal cycle of CH_4 that is similar in the spatial-temporal seasonality pattern as that of CO_2 (Figure 4a). Each

475   hemisphere exhibits its lowest CH_4 mixing ratios just after the summer solstice, up to 1.6% or 28 ppbv lower than the global

476   mean in the case of the high-latitude northern summer (Figure 4a). Quantifying the underlying reasons is beyond the scope of

477   this study, although the seasonally varying atmospheric sinks by OH oxidization are likely the main contributor to that pattern

478   – in combination with seasonally varying natural and anthropogenic sources.

479   The latitudinal annual-mean gradient of CH_4 mixing ratios is separated into its first two EOFs, with the first EOF being a

480   continuous north-to-south gradient of about 90 ppbv in the recent observational period (combination of EOF and its score, see

481   Figure 4c and d). The second EOF is a distinct mid-northern latitude local maximum with a high-latitude low, showing a slight

482   but marked rise in 2008 within the 1985 to 2014 observational data window. Quantifying the reasons for this hump are again

483   beyond the scope of this study, with the possibility of a shift in locations of sampling stations or coal-seam gas-fracking related

484   fugitive emissions being possible contributors. While we optimize the first EOF, the general north-south gradient to match the

485   Greenland data and Antarctic Law Dome data in the past, we keep the second EOF of the latitudinal gradient constant at its

486   1985 value.

487   As a result of the constant extrapolation of the second EOF, and the optimization of the first EOF's score (Figure 4d), we yield

488   a total annual-mean meridional gradient for the last decades that features around 80 ppbv higher surface CH_4 mixing ratios in

489   mid-to-high northern latitudes compared to the global mean and around 60 ppbv lower CH_4 mixing ratios at the high southern

490   latitudes (Figure 4b). In pre-industrial times, our approach of regressing the score of EOF1 with global emissions suggests this

491   gradient to be smaller, with only approximately 20-30 ppbv higher northern and 20 ppbv lower southern latitude surface mixing

492   ratios (Figure 4b). These mean interpolar differences and their variations have earlier been quantified by Etheridge (1998a)

493   and Mitchell et al. (2013), yielding similar results (between 30 to 60 ppbv) compared to our 40 to 50 ppbv estimate.

494   **3.3   Nitrous Oxide**

495   N_2O mixing ratios from ice cores dating back 800 thousand years (Fluckiger et al. 2002, Schilt et al. 2010b) varied

496   approximately between 200 ppbv and 300 ppbv, with most recent glacial mixing ratio minima of 180 ppbv around 23 thousand

497   years ago (Sowers et al. 2003) (Figure 1e). The ice core record over the last 2000 years indicates marked difference between

498   the Law Dome and GISPII record (Sowers et al. 2003), with the latter being up to 10 ppbv lower. Here, as with CH_4, we use

499   again a median quantile piecewise polynomial regression on the Law Dome record, assuming constant N_2O mixing ratios

500   between year 0 and the first Law Dome data point in Year 154. In contrast to CH_4, there is not a monotonic increase of mixing

501   ratios, but rather an initial slight decrease until year 630 down to a minimum mixing ratio of 265 ppbv in our smoothed

502   timeseries with a subsequent slow increase until the 9th century AD, then a slight decrease until 1650 in the smoothed global-

503 mean mixing ratios. A temporary local maximum indicated by individual Law Dome data in the 15th century is not resolved

504 by our smoothing, and a similar spike in the 17th century is only just reflected (Figure 1f). Several data points indicate a small

505 decrease after a 1750 maximum, with a minimum in 1850 of around 273.02 ppbv. After that, N_2O mixing ratios increased

506 markedly, reaching 1900, 1950, 2000 and 2014 values of 279.45, 289.74, 315.76 and 326.99 ppbv, respectively (Table 7).

507 Compared to CH_4 and CO_2, the seasonality and latitudinal gradient of N_2O are relatively small. The N_2O seasonality is only

508 0.1% of global mixing ratios and is almost symmetric and seasonally time-synchronized between the northern and southern

509 hemispheres with minima in the southern hemisphere late autumn and northern hemisphere summer/autumn (Figure 5a). The

510 seasonality is currently of the same size as the underlying trend, leading to global mean N_2O mixing ratios increasing in the

511 latter months of any year with a subsequent flattening in the first half of any calendar year (e.g. Figure 5h). Given a counter-

512 intuitive slight decrease of the north-south gradient with increasing global N_2O emissions in recent years, we assumed constant

513 scores for the latitudinal gradient EOFs for times before 1996 (Figure 5d). Due to measurement fluctuations in the first years

514 when systematic measurements started in 1978 that are larger compared to the recent period, we chose to interpolate N_2O

515 global-mean mixing ratios over 1966 to 1987. For the period between 1978 and 1987, this interpolation is closely aligned with

516 and can be seen as smooth representation of the atmospheric measurements (Figure 5f, cf. ALE/GAGE/AGAGE data as shown

517 at http://agage.eas.gatech.edu/data_archive/data_figures/gcmd_month/n2o_monS5.pdf).

3.4   Ozone Depleting Substances and other chlorinated substances

519 Ozone depleting substances (ODSs), i.e. the substances destroying ozone and being controlled under the Montreal Protocol,

520 have a large warming effect. In particular CFC-12 and CFC-11 are important greenhouse gases, as well as the replacement

521 substance HCFC-22, which, unlike CFCs, continues to increase in the atmosphere, albeit at a declining rate. The radiative

522 forcing of CFC-12 alone since 1750 is equivalent to that of N_2O, which is usually considered the third most important

523 greenhouse gas after CO_2 and CH_4 (Table 10). The impact of ODSs on climate is somewhat complicated by their destruction

524 of ozone, which leads to a cooling of the global climate. The latest estimates suggest that this cooling might offset roughly

525 two-thirds of the warming of the entire class of ODSs (Shindell et al. 2013). Note that we consider here also methylene chloride

526 and methyl chloride, although these chlorinated substances are not controlled by the Montreal Protocol and hence often not

527 termed ozone depleting substances (WMO 2014).

528 The most abundant ozone depleting substances in the atmosphere (in 2014) are CFC-12 (520.6 pptv), CFC-11 (233.1 pptv)

529 and HCFC-22 (229.5 pptv), with their mole fractions being about six orders of magnitude lower than currently measured for

530 CO_2 (Table 3). In addition, methyl chloride CH_3Cl has a high mole fraction (539.54 pptv), although is not considered an ODS

531 here as it is not controlled by the Montreal Protocol. Out of the 17 considered chlorinated and ozone depleting substances, only

532 6 have currently increasing mixing ratios. Those are the three HCFCs, of which the increase in HCFC-22 alone has offset the

533 reducing radiative forcing of all other ozone depleting substances (ODS) over the past decade (Figure 6m). The other three

534 substances that are still increasing are Halon-1301, methylene chloride (CH_2Cl_2) and chloroform ($CHCl_3$). Chloroform had

535 been decreasing in the 1990s and stabilized in the 2000s, but again recently showed an increase (Figure 33).

536 Four of the considered chlorinated and ozone depleting substances are assumed to have natural emissions and hence non-zero

537 pre-industrial mixing ratios. Specifically, methyl chloride (CH_3Cl) is assumed to have pre-industrial global-mean mixing ratios

538 of 457 pptv, carbon tetrachloride (CCl_4) of 0.025 pptv, and methyl bromide (CH_3Br) of 5.3 pptv. Chloroform ($CHCl_3$) is

539 assumed to have a pre-industrial mixing ratio of about 6 pptv, approximately in line with findings by Worton et al. (2006) and

540   the estimation by Aucott et al. (1999) that in 1990 $CHCl_3$ was at about 8 pptv, 80% are of natural origin. Lastly, methylene

541   chloride (CH_2Cl_2) is estimated to have a 6.9 pptv pre-industrial mixing ratio with a strong latitudinal gradient that results in

542   northern (southern) hemisphere average mixing ratios of 12.8 (1.0) pptv, even though this isn't well described by observational

543   data. The transition of mixing ratios of some species between the observational station data and pre-industrial levels are also

544   uncertain. For CH_2Cl_2, our derivation is in line with the smooth trajectory of Trudinger et al. (2004), indicating an almost

545   monotonic transition between 1997 values and pre-industrial mixing ratios (Figure 29f).

546   The seasonal cycle of ozone depleting substances and other synthetic GHGs can be influenced by seasonally varying

547   stratospheric-tropospheric air exchanges, interhemispheric transport, tropopause heights, emissions and, for those substances

548   with OH-related sinks, the seasonally varying OH mixing ratios. For 11 out of the 17 considered ozone depleting substances

549   we find some indication of seasonal cycles based on the analyzed station data, namely for CCl_4, CFC-11, CFC-12, CFC-113,

550   CH_2Cl_2, CH_3Br, CH_3CCl_3, CH_3Cl, $CHCl_3$, Halon-1211, and HCFC-11. Our analysis indicates that HCFC-141b also shows

551   some signs of a seasonal cycle, although we here assumed a zero seasonal cycle due to data sparsity (see Figure 38a). We find

552   the strongest seasonal cycles in case of the short-lived species CH_3Cl, $CHCl_3$, CH_3Br and CH_2Cl_2 with absolute maximal

553   seasonal deviations of -11%, -12%, ±9%, -32% compared to the annual mean, respectively. For the radiatively important and

554   longer-lived species CFC-12, CFC-11 and HCFC-22, the seasonal cycle is much smaller, with ±0.2%, ±0.4%, ±0.8%,

555   respectively.

556   Similar to the seasonality, the latitudinal gradient is found to be especially pronounced for the short lived substances.

557   Specifically, CH_2Cl_2 with a lifetime of 0.4 years, CH_3Br with a lifetime of 0.8 years, CH_3CCl_3 with a lifetime of 5 years and

558   CH_3Cl with a lifetime of approximately 1 year and $CHCl_3$ with a lifetime of 0.4 years show substantial latitudinal gradients

559   due to spatially heterogeneous sinks and sources (lifetimes following Table 8.A.1 in IPCC WG1 AR5 (2013)). While normally

560   the mid to high northern latitudes experience the highest mixing ratios for these compounds, the measurements for several

561   substances suggest a pronounced high-latitude northern hemisphere decline in annual average mixing ratios (see e.g. CH_3Cl in

562   Figure 32b and c).

3.5   Other flourinated greenhouse gases

564   The 23 other gases in this study whose production and consumption is not controlled under the Montreal Protocol are the

565   hydrofluorocarbons (HFCs), perfluorocarbons (PFCs) as well as Sulphur hexafluoride (SF_6), nitrogen trifluoride (NF_3), and

566   sulphuryl fluoride (SO_2F_2). Except for the latter, the emissions of all these species are controlled under the Kyoto Protocol and

567   covered by most "nationally determined contributions" (NDCs) under the Paris Agreement. In aggregate, this group of

568   synthetic GHGs however exerts an almost factor of 10 smaller greenhouse gas effect to date compared to the ozone depleting

569   substances (cp. Figure 6g and m). In contrast to the gases controlled under the Montreal Protocol, nearly all of these other

570   fluorinated gas mixing ratios are still rising, however, with the exception of HFC-152a, which has stopped growing since 2012

571   and may now be in decline, Figure 55f). Thus, a primary concern with these gases is the potential for substantial climate forcing

572   in the future if uncontrolled growth continues.

573   The most abundant of these gases is the refrigerant HFC-134a with 2014 mixing ratios estimated to be 80.5 pptv, followed by

574   HFC-23 (26.9 pptv), HFC-125 (15.4 pptv) and HFC-143a (15.2 pptv). At the other end of the mixing ratio spectrum, we include

575   results from Ivy et al. (2012) for some PFCs that exhibit low mixing ratios of 0.13 pptv (C_5F_{12} and C_7F_{16}) or 0.09 pptv (C_8F_{18})

576   (Table 3). The only gas considered to have natural sources and hence a pre-industrial background concentration is CF_4 with an

577   assumed pre-industrial mixing ratio of 34.05 pptv (see Figure 48) in line with findings by (Trudinger et al. 2016).

578   For a number of substances, especially the PFCs with lower abundances, there were not sufficient data available to estimate

579   the seasonality of atmospheric mixing ratios. We consider seasonality only for 3 of the 23 species. HFC-134a has a somewhat

580   atypical pattern of lowest mixing ratios in the spring northern hemisphere (-2.6% compared to annual mean) as other gases

581   normally show a summer or autumn low point of mixing ratios. This spring minimum results from a seasonality of sources of

582   this refrigerant (Figure 53a), although seasonality in loss also likely plays a role (Xiang et al. 2014). Secondly, the short-lived

583   HFC-152a (lifetime 1.5 years) shows seasonal variations of up to -13% while the very long lived SF_6 (lifetime of 3200 years)

584   exhibits a much smaller seasonality of up to -0.5%.

585   For most of the considered substances, the latitudinal gradient is rather small. Exceptions are the shorter-lived species like

586   HFC-32, whose mixing ratio rose quickly since 2000 due to rapidly increasing northern hemispheric sources (Figure 50b),

587   HFC-152a, and some other shorter lived HFCs. For the three heavier PFCs with very low abundances of well below 1 pptv in

588   2014, namely C_6F_{14}, C_7F_{16} and C_8F_{18}, we incorporated hemispheric data from Ivy et al. (2012). Before about 1990, those three

589   gases are suggested to have reverse latitudinal gradients with higher southern hemispheric mixing ratios. Due to the very low

590   mixing ratios near the limit of measurement, future studies may need to confirm whether those reverse gradients existed (and

591   if so, why). Given the negligible radiative forcing from these gases to date, this uncertainty does not affect the overall results.

4   The CMIP6 recommendation and data format

593   We present the community CMIP6 data sets of historical GHG mixing ratios. In conjunction with other data, these greenhouse

594   gas surface mixing ratio data sets are to be used in the concentration-driven runs for the climate model inter-comparison project

595   phase 6 (CMIP6) (Eyring et al. 2015), specifically the historical run, and the idealized runs of abrupt4x, 1pctCO2 as well as

596   the picontrol. The CMIP6 recommendation as decided by the CMIP Panel is: "In the CO_2-concentration-driven historical

597   simulations, time-varying global annual mean mixing ratios for CO_2 and other long-lived greenhouse gases are prescribed. If

598   a modelling center decides to represent additional spatial and seasonal variations in prescribed greenhouse gas forcings, this

599   needs to be adequately documented." (Eyring et al. 2016).

600   This study provides the data for both the simple global annual mean mixing ratios as well as the mixing ratio histories that take

601   latitudinal and seasonal variations into account (see data description further below). CMIP6 modelling groups should indicate

602   which time and space resolution of the data version they applied. All data are freely available via the PCMDI servers

603   (https://pcmdi.llnl.gov/search/input4mips/) as netcdf files. In addition, summary tables and csv, xls and MATLAB mat versions

604   of the data files are provided at climatecollege.unimelb.edu.au/cmip6.

605   In terms of the spatio-temporal resolution, four files for each of the 43 greenhouse gases and the three equivalence species

606   CFC-12-eq, HFC-134a-eq and CFC-11-eq (section 2.1.10) are provided as:

607   I.   latitudinal 15-degree bins with monthly resolution (filename-code: '_15degreelatXmonth'), with monthly means for

608   each latitudinal band provided at the centre of the box, i.e. -82.5, -67.5, … 67.5, 82.6.

II. interpolated latitudinal half degree bins with monthly resolution (filename-code: '_0p5degreelatXmonth'), with means for each latitudinal band provided at the center of the box, i.e. -89.75, -89.25, … 89.25, 89.75. The area-weighted mean over 15-degree latitudinal bands is the same as the files under (1).

III. Global and hemispheric means with monthly resolution (filename-code '_GMNHSHmeanXmonth').

IV. Global and hemispheric means with annual resolution (filename-code '_GMNHSHmeanXyear')

Given that climate effects will vary whether global, annual-mean or seasonally varying latitudinally-resolved surface mixing ratios are prescribed, modelling groups are asked to document which data set(s) they choose.

The CMIP6 recommendation for the **picontrol** experiment are to use the 1850 greenhouse gas mixing ratios with annual means as provided in Table 5 (CO_2 annual-mean mixing ratios of 284.32 ppmv, CH_4 mixing ratios of 808.25 ppbv and N_2O mixing ratios of 273.02 ppbv). Other gases are covered, depending on the choice of the modelling group by either following Option 1, Option 2, or Option 3, or an equivalently suited method that aggregates the radiative effect of the remaining 40 GHGs or a large fraction thereof.

The **abrupt4x** experiment should keep all greenhouse gas mixing ratios unchanged from the picontrol run except for the CO_2 mixing ratios, which should be increased instantaneously in year 1 (=1850) of the experiment to four times the 1850 value, namely to 1137.27 ppmv (Table 6).

The **1pctCO2** experiment should also keep all greenhouse gas mixing ratios unchanged from the picontrol run except for CO_2 mixing ratios. Starting in year 1 of the experiment, CO_2 mixing ratios should increase by 1% per annum, reaching slightly over doubled CO_2 mixing ratios in year 70 (or 1920, if the startyear is set to 1850) with 570.56 ppmv and 1,264.76 ppmv in year 150 (or year 2000) (Table 4).

As with the abrupt4x and 1pctCO2 scenarios, the **historical** experiment should diverge from the picontrol run. Greenhouse gases should then follow the historical observations as derived in this study, reaching e.g. CO_2 mixing ratios of 397.55 ppmv in 2014, and CH_4 and N_2O mixing ratios of 1831.47 ppbv and 326.99 ppbv, respectively. Modelling groups should document which spatial and temporal resolution (see above) of the provided data they use, as the climate effect will likely be different with different resolutions.

The future concentration pathways, the so-called 'SSP-RCP' scenarios, considered under ScenarioMIP (O'Neill et al. 2016) are planned to provide the same data formats and spatio-temporal resolutions. The methodological approach to derive and adapt both seasonality and latitudinal gradients in this study was designed such that a future extrapolation will be possible.

4.1 The vertical dimension

The purpose of our reconstructions is to provide radiative forcing for climate models. This radiative forcing depends on the vertical as well as horizontal distribution of a gas' mixing ratio. Our reconstructions describe only surface concentrations and modelers need some method for calculating the three-dimensional distribution. If the model is capable of calculating tracer transport we recommend using this study's surface reconstruction as a mixing ratio lower boundary condition for the tracer transport. If this is not possible then we propose a simple equation to reflect the relaxation of horizontal gradients with height and the upward propagation of mixing ratio changes from the surface.

644   In case of CO_2, there are no sinks in the middle and upper troposphere or stratosphere and only slight sources due to the

645   oxidization of CH_4 and carbon monoxide (CO). Evidence from Earth System Models (Figure 7) indicates an almost well-

646   mixed tropospheric column in the tropics and little or partly reversed vertical gradient in the southern troposphere, while

647   the annual-mean gradient in the northern hemisphere is – depending on the season – variable. The annual average vertical

648   gradient in the northern hemisphere is decreasing in all CMIP5 ESM models analysed here (Figure 7).

649   In order to enable the implementation surface mixing ratios in models that do not have an inherent transport model to

650   capture vertical gradients, we offer here simplified parameterizations as default options. While an assumption about a

651   well-mixed atmospheric vertical column seem a justifiable simplification, these simple vertical extensions could increase

652   the realism, vertical heating structure and overall climatic effect. Specifically, modelling teams could use the following

653   approximation to extend surface mixing ratio fields (at the 1000hPa level) towards higher tropospheric and stratospheric

654   levels. First, a bell-shaped mixing ratio distribution is assumed at the 100hPa level for the higher latitudie tropopause and

655   tropical upper troposphere:

656    $C(l, 100hPa, t) = \bar{C}(global, 1000hPa, t) \ldots + \left(\bar{C}(global, 1000hPa, t - 5yrs) - \bar{C}(global, 1000hPa, t)\right) * \frac{\sin(l)^2}{2}$

657   (9)

658   With $\bar{C}(global, 1000hPa, t)$ indicating global-average, annual-average mixing ratios at the surface 1000hPa level at time

659   t. Ideally, a smoothed mean-preserving monthly dataseries of these annual-average global averages is used to prevent step

660   changes from calendar month 12 to 1. Equivalently, $\bar{C}(global, 1000hPa, t - 5yrs)$ indicates the global-average, annual-

661   average surface mixing ratio 5 years earlier. The $\frac{\sin(l)^2}{2}$ factor depends on the latitude l and results in the bell-shaped

662   mixing ratio curve with concentrations at the tropical 100hPa level to be identical to the global average surface mixing

663   ratios, while the polar mixing ratios are effectively of a medium age (2.5 years in the case of linearly increasing

664   concentration history). Having defined this 100hPa concentration level, the tropospheric mixing ratios at latitude l and

665   pressure level p (with p>100hPa) can then be assumed as a simple linear interpolation between the surface mixing ratio

666   level at latitude l and the 100hPa level, so that:

667    $C(l, p, t) = C(l, 100hPa, t) + \left(C(l, 1000hPa, t) - C(l, 100hPa, t)\right) * \frac{(p - 100hPa)}{(1000hPa - 100hPa)}$ (10)

668   Above 100hPa - i.e. in the tropical upper troposphere and stratosphere, the mixing ratio is a simple linear interpolation

669   between the 100hPa level and the top-of-the atmosphere 1hPa level that is assumed to have a median age of air of 5 years,

670   so that for p<100hPa:

671    $C(l, p, t) = \bar{C}(global, 1000hPa, t - 5yrs) \ldots + \left(C(l, 100hPa, t) - \bar{C}(global, 1000hPa, t - 5yrs)\right) \ldots * \frac{(p - 1hPa)}{(100hPa - 1hPa)}$

672   (11)

673   With $\bar{C}(global, 1000hPa, t - 5yrs)$ being again the global-mean surface mixing ratio (1000hPa) 5 years ago and

674    $C(l, 100hPa, t)$ the latitudinally-dependent mixing ratio at the 100hPa level.

675   This equation captures the general form of the vertical CO_2 mixing ratio gradient observed in CMIP5 ESM models – with

676   the 100hPa being an approximate division line of the vertical CO_2 gradient in all CMIP5 models (see bold red line in

677   Figure 7). The annual-average vertical gradient in the northern hemisphere will be somewhat reducing the effect of the

678   strong surface latitudinal gradient. The idealized shaped of the above parameterization for an hypothetical flat surface

679   mixing ratio of 100 ppmv is shown in Figure 8b. Assuming linearly increasing surface mixing ratios from a south pole

680   minimum towards a 3 ppmv higher north pole maximum will – under this simplified parameterization - result in an almost

681   zero vertical tropospheric gradient in the southern hemisphere (Figure 8a).

682   For non-CO_2 gases, we here suggest a scheme adapted from the CESM model current parameterization – in case that

683   models do not have their own vertical extrapolation methods. These parameterisations assumed a simplified vertically

684   well-mixed troposphere and define a tropopause height as:

685   $p_{tropopause}(l) = 250hpa - 150hPa * \cos(l)^2$ (12)

686   With $p_{tropopause}(l)$ being the tropopause height in hPa, depending on the latitude l. Thus, below the tropopause, the zonal

687   mean mixing ratios are assumed to be well-mixed vertically, so that:

688   $C(l,p,t) = C(l,1000hPa,t)$ for p>p$_{tropopause}$

689   The stratospheric mixing ratio can then modelled for p<p$_{tropopause}$ as:

690   $C(l,p,t) = \bar{C}(global,1000hPa,\bar{t}-1yrs) * \left(\frac{p}{p_{tropopause}(l)}\right)^s$ (13)

691   with $\bar{C}(global,1000hPa,t)$ being the global mean and annual-mean surface mixing ratio of the previous year,

692   p/p$_{tropopause}$(l) being the ratio of the pressure at level p and the tropopause pressure at that latitude and *s* being a gas-

693   dependent scaling factor (Table 11).

694   As mentioned above, this simple vertical extrapolation option of the provided surface data is only to be regarded as a

695   simplified fall-back option in case that there are no model-intrinsic parameterizations available or active tracer transport

696   part of the model. While this study provides the main step from global-mean and annual-mean mixing ratio histories

697   towards zonally and monthly resolved ones, future research will be needed to provide more robust 4-D fields of mixing

698   ratios.

5   Discussion

We compare our results with a number of other data products. First, a comparison with the previous CMIP5 recommendation for historical GHG mixing ratios is provided (5.1). Then we analyse and compare our CMIP6 recommendations to what the Earth System Models from the previous CMIP5 intercomparison produced in terms of CO_2 mixing ratio fields in the emission-driven runs (5.2). Thirdly, we compare our data sets to the other global-mean, hemispheric and latitudinally-resolved data sets, namely the NOAA Marine Boundary Layer product and the WDCGG time series (5.3).

5.1   Comparison to CMIP5 input datasets.

For the CMIP5 inter-comparison, greenhouse gas mixing ratios were specified for historical times until 2005, followed by RCPs and their extensions until 2300. The recommendations for GHG mixing ratios were global and annual mean time series (Meinshausen et al. 2011b), not including a seasonal cycle or latitudinal gradient. Those historical time series were composite products of existing ice core and instrumental data annual means (see references in Meinshausen et al. 2011). Global, annual-mean CO_2 mixing ratios over 1975 to 2005 were very close (<0.7 ppmv different) to our current recommendations for CMIP6. The CMIP5 time series did not show the slight maximum in CO_2 mixing ratios around 1973 (difference 1.2 ppmv), and was generally lower between 1940 and 1956 at about the time of the World War II, when CO_2 mixing ratios briefly plateaued (differences between 1.0 and 2.3 ppmv) (Figure 9). While the CMIP5 historical greenhouse gases were an ad-hoc extension to the RCP pathways, our CMIP6 recommendation advanced the integration of historical data by accounting for latitudinal gradients (ice core data in CMIP5 has not been adjusted for the latitudinal gradients) and by taking into account a large array of additional data beyond a single network average for more recent times.

Recommended global-mean CH_4 mixing ratios for CMIP5 were generally lower than derived here, up to 50 ppbv around 1910 and between 25-30 ppbv more recently (2000-2005). The primary reason is that the CMIP5 data did not take into account the strong latitudinal gradient of CH_4 mixing ratios. In terms of N_2O mixing ratios, the CMIP5 historical timeseries did not capture some higher frequency variability, which caused the CMIP6 recommendation for the picontrol 1850 global-mean mixing ratio being lower by around 2.5 ppbv, and N_2O mixing ratios in the 1910s being higher by up to 2.3 ppbv (Figure 9).

Overall, CMIP5 and CMIP6 recommendations are relatively similar. The 1850 picontrol values at the time of CMIP5 were slightly higher for CO_2 and N_2O (0.14% or 0.4 ppmv and 0.87% or 2.4 ppbv, respectively), countered to some degree by slightly lower values for CH_4 (2.18% or 17.3 ppbv). This is equivalent to a small net change in base year radiative forcing of 0.0065 W/m^2, when applying linear radiative efficiencies of IPCC AR5 (Appendix 8.A in IPCC WG1 AR5).

5.2   Comparison to CMIP5 ESM CO_2 mixing ratio fields.

Several Earth System models during CMIP5 used prescribed CO_2 emissions instead of CO_2 mixing ratios and derived CO_2 mixing ratio fields endogenously. For the year 1875, we see that models vary greatly, with some showing reverse latitudinal gradients with higher mixing ratios in the south (e.g. CanESM2), almost no gradient (CESM1-BCC), a local maximum in the tropics with lower poleward mixing ratios (MIROC-ESM) and very heterogeneous fields with high mixing ratios over the tropical rainforests (NorESM1-ME) (see Figure 10). Similarly, for 1990 (Figure 11), the fields are dissimilar, with some models exhibiting very strong north-south gradients (MPI-ESM-LR), while others show little gradients (CanESM2), although all models indicate an increase of northern hemispheric mixing ratios compared to the global mean between 1875 and 1990 (Figure 12).

735   Though not as strong as NorESM1-ME, most models show a slight tropical maximum in the latitudinal gradient (exceptions

736   are CanESM2, MIROC-ESM) both during 1875 and 1990 (Figure 12). The high-latitude southern mixing ratio deviations from

737   the global-mean in the 1875 time slices have different signs across the models, with some indicating clearly lower mixing

738   ratios (BNU-ESM, MPI-ESM-LR, NorESM1-ME) and others suggesting slightly positive mixing ratios (CanESM2, MIROC-

739   ESM in 1875). The average of three CMIP5 ESMs with full CO_2 data coverage at the surface 1000 hPa level and approximately

740   correct global mean CO_2 mixing ratio values (CanESM2, MPI-ESM-LR, and NorESM1-ESM) shows a latitudinal gradient for

741   1990 comparable to the observed one derived in this study (Figure 2b). In light of this evidence, we assumed constant mixing

742   ratios with latitude for pre-industrial times.

743   In general, all ESMs show climatological seasonal cycles of CO_2 mixing ratios similar to the seasonality derived in this study

744   (Figure 2a). The climatological 1861-1890 average mixing ratios across the models clearly exhibits higher seasonality in the

745   northern hemisphere, especially above 40°N. While the seasonality in some models is weaker, especially CESM1-BCC, others

746   show variations of up to ±10 ppmv (MPI-ESM-LR). In addition, the latter model exhibits as a southern hemisphere seasonality

747   larger than other models and what we observe. As expected from our analysis of observational data, this seasonality strengthens

748   up to 1990 across all models (Figure 14). The latitudinal spread of the northern hemisphere minimum extends southwards

749   towards the equator in August, September and October as we observe (Figure 2a), with the exception of the BNU-ESM model

750   (Figure 14), which indicates a northward propagation of the minimum summer mixing ratio values.

751   Overall, the basic features of the latitudinal gradient and seasonal cycle are represented in the ESMs as seen in the observational

752   data. However, the variation across the models is substantial. This difference of several ppmv in the latitudinal gradient or

753   seasonal cycles will lead to follow-on differences in the climate response observed in those models.

754   As common input for the CMIP5 concentration-driven experiments, all models were provided with the same historical global

755   and annual mean CO_2 mixing ratios. Some models had the capability to nudge internally-generated CO_2 mixing ratio fields to

756   match the prescribed annual and global mean CO_2 mixing ratios. Nevertheless, the differences in those internally-generated

757   fields can be substantial as our analysis from CMIP5 shows and different from the observations. While the internally-generated

758   CO_2 mixing ratio fields are a better match to observations compared to globally uniform annual-mean values, the question

759   arises as to how important those differences are for cross-model comparisons and detection and attribution studies. Differences

760   between model output and observational diagnostics are influenced by the quality of the prescribed input data, and input data

761   have been prescribed in different ways across models. For future model inter-comparisons, it seems preferable that any

762   concentration-driven runs would use the same starting point. Of course, the longer-term aspiration has to be that emission-

763   driven ESMs reliably reproduce observational mixing ratio patterns. For CMIP6, modelling groups are requested to document

764   their choice of concentration input data, specifically in relation to the chosen temporal and spatial resolutions.

765   **5.3   Comparison of global-means to NOAA marine boundary layer products and WDCGG**

766   The primary observational data product with coverage across all latitudes are the marine boundary layer or GLOBALVIEW

767   fields (NOAA 2013, NOAA ESRL GMD 2014c) produced by NOAA based on the Cooperative Global Air Sampling Network

768   (Conway et al. 1994, Dlugokencky et al. 1994b, Trolier et al. 1996) for CO_2, CH_4 and N_2O (available at

769   http://www.esrl.noaa.gov/gmd/ccgg/mbl/mbl.html, with N_2O data pers. comm. Pieter Tans). The aggregation method used to

770   produce this data set is to first fit parametric functions to the weekly data of each station, thereby providing a gap-filling

771   method. In a next step, the procedure fits smooth weekly latitudinal distributions to the various station data points (Tans et al.

772   1989). These latitudinal distributions are then combined into a 2-D field of latitude versus time, comparable to this study's

773   data product. The time period for which these NOAA MBL data products is 1979 to 2014 for CO_2, 1983 to 2014 for CH_4 and

774   2001 to 2014 for N_2O.

775   The four main methodological differences between the NOAA MBL data product and ours are (1) the NOAA data product has

776   a higher resolution in time (weekly instead of monthly) and latitudes, (2) the NOAA MBL data product includes only a subset

777   of the NOAA network data (sites within the marine boundary layer), while this study mixes both NOAA and AGAGE network

778   data in the case of CH_4 and N_2O, (3) this study characterizes the global fields by lower rank representations (EOFs) of annual

779   mean latitudinal gradients and seasonality, while the NOAA product derives latitudinal gradients (and seasonality thereby only

780   implicitly) directly from the observations at each time step. In other words, the main smoothing/regularization step in our study

781   happens at a later level in the analysis, and (4) this study is extended by ice core and firn data, regressions and extra-

782   /interpolation to span the full time period between year 0 and 2014. In other words, this study seamlessly merges in situ

783   observational, air archive, ice and firn data to generate a comprehensive data product.

784   For several applications, the NOAA data product has clear advantages. However, with the task to produce a continuous data

785   product beyond the instrumental observations, this study had to choose a method that was readily extendable. Hence, this study

786   chooses the characterization of global fields into global-means, latitudinal gradients and seasonality. This implies a high degree

787   of regularizations by relying on EOFs and corresponding scores. By regression, these EOF scores for latitudinal gradients or

788   seasonality changes can be easily extended to cover the full time period of interest. Hence, our method allows an estimate of

789   global-means even if there is a single data point (such as a Law Dome ice core record for a specific year), under the assumption

790   that latitudinal gradients and seasonality are captured by the derived EOFs and regressed EOF scores.

791   Global-average time series of monthly greenhouse gas mixing ratios are also provided by the World Data Center for

792   Greenhouse Gases (WDCGG) (Tsutsumi 2009). The WDCGG product uses similar smoothing techniques as the NOAA

793   product, but include, like this study, a broader set of measurement stations, both in terms of regional coverage (including

794   continental stations) and different networks that use different calibration scales, sampling, gas handling etc.

795   We compare the results of this study and NOAA MBL and WDCGG products for the time periods covered by the latter.

796   Overall, our monthly hemispheric averages of CO_2 closely match the NOAA product. The NOAA product suggests a slightly

797   faster increase of northern hemispheric mixing ratios in the latter months of each calendar year (cf. thick and thin orange lines

798   in Figure 15a). Specifically, this difference results from the mid-latitude northern hemispheric bands from about 1995 onwards

799   (with monthly-average differences of up to 4 ppmv) where our study is higher than the NOAA product. This could be because

800   this study does not screen out land stations closer to the pollution sources, as the NOAA marine-boundary-layer product does.

801   Likewise, the WDCGG includes a broader set of stations and matches very closely with our global-mean time series, with our

802   study being very close to WDCGG or in between NOAA MBL and WDCGG (Figure 15a). Given that the difference between

803   the NOAA study and our study has a strong seasonality, the nature of those pollution sources and how they become mixed in

804   the atmosphere, if these effects contribute to the differences, could be a combination of fossil fuel related and (more seasonally-

805   varying) biospheric sources (Figure 16c). The southern hemispheric means of our study and NOAA MBL are very closely

806   matched (cf. thick and thin blue lines in Figure 15a). Consequently, the global-mean mixing ratios from NOAA MBL and our

807   study are closely matched, although again our data suggests NH autumn mixing ratios rising slightly faster than the NOAA

808   MBL product, reflecting the northern hemispheric difference (cf. thick and thin black lines in Figure 15a).

809   For CH_4, the differences between this study and the NOAA MBL data are more systematic and stronger (~10 ppbv), with

810   generally higher surface CH_4 mixing ratios implied by this study (Figure 15b). Again, this study's global mean matches closely

811   the WDCGG or sits in between the NOAA MBL and the WDCGG data products. There are some differences in the seasonality

812   compared to the NOAA MBL product though. The seasonal variation is similarly shaped between our study and NOAA MBL

813   for the southern hemisphere, although there seems to be a slight phase-shift of about a month with the NOAA MBL product

814   in the southern hemisphere assuming a slightly earlier increase and decrease and slightly higher amplitude (Figure 15b). This

815   phase-shift of the southern hemisphere together with sometimes lower peak northern hemispheric mixing ratios in the NOAA

816   MBL product suggests global-mean NOAA MBL CH_4 mixing ratio that show a double peak within any year, while our data

817   assimilation and the WDCGG product suggests a smoother single-peak oscillation of global-mean CH_4 mixing ratios (Figure

818   15b). This peak results from the mid northern latitudes, where in the summer months, our study suggests up to 40 or 50 ppbv

819   higher mixing ratios (Figure 17c).

820   For N_2O, the WDCGG global-mean and our data match very closely, with our implicit smoothing due to our lower rank

821   representation of seasonal cycles and latitudinal means resulting in a smoother global mean compared to WDCGG (Figure

822   15c). Similarly, the draft data product of the NOAA MBL indicates almost identical mixing ratios to our concentration fields

823   over the available time period from 2001 to 2014, with maximal differences being 0.8 ppbv (Figure 18).

824   In summary, our dataset closely matches the global-means of WDCGG in many years, but provides a complete 2-D field of

825   mixing ratios. In comparison to the NOAA MBL products, there is one more systematic difference. Our CMIP6 GHG mixing

826   ratio fields are meant to represent the mean monthly state of the latitudinally-averaged surface atmosphere, including land and

827   polluted areas, i.e. not confined to areas with background mixing ratios (see Section 6 limitations). This is a key difference to

828   the NOAA Marine Boundary Layer product, which is a consistent background mixing ratio product, resulting in slightly lower

829   global-mean mixing ratio estimates.

830   **5.4   Comparison to mid-troposphere CO_2 mixing ratios by NASA Aqua satellite**

831   Since its launch in 2002, the Aqua satellite and its infrared sounder provides an additional independent data product to estimate

832   tropospheric CO_2 mixing ratios. Rather than at ground level, this sensor provides an estimate of tropospheric mixing ratios

833   with a maximum sensitivity around 7km height, i.e. in the mid-troposphere. In the tropics and the parts of the southern

834   hemisphere that are covered by the Aqua satellite product, the agreement between our data and the AIRS level 3 data (available

835   at: ftp://acdisc.gsfc.nasa.gov/ftp/data/s4pa/Aqua_AIRS_Level3/AIRX3C2M.005/) is encouraging, although the overall

836   gradient is lower in line with 3-D atmospheric transport model results (Olsen and Randerson 2004). In the northern hemisphere,

837   the difference in the phase and amplitude of the seasonal cycle is most apparent, with satellite data showing a later onset of the

838   autumn mixing ratio increase by about 4 months while the drawdown of mixing ratios seems closer in phase between mid-

839   troposphere and surface mixing ratios (Figure 15a). Overall the amplitude is less than half of the surface hemispheric mean

840   amplitude, leading to seasonally higher winter and lower summer mixing ratios of our surface data product in the northern

841   hemisphere by up to 10 ppmv (Figure 16e).

842   This systematic difference between ground-level and mid-atmosphere mixing ratios, supported by 3-D transport modelling

843   studies (Olsen and Randerson 2004), has ramifications for the implementation of vertical mixing ratio profiles in climate

844   models. Without taking into account the dampened seasonal cycle and latitudinal gradient in the mid and higher troposphere,

845   the models could overestimate the variations in the radiative effects, if our latitudinally and monthly resolved surface mixing

846 ratio fields are prescribed. On the other hand, if global- annual mean values are prescribed, the radiative forcing effect

847 variations over latitudes and within a year will obviously be underestimated.

5.5 Comparison to other literature studies.

849 Our greenhouse gas derivations over the recent instrumental periods are based on the AGAGE and NOAA station-by-station

850 data and we extended our 2-D mixing ratio field results back in time by using e.g. global-mean estimates of previous studies'

851 estimates (Methods). The AGAGE and NOAA networks themselves publish global-mean results, and WMO as well as other

852 literature studies produce composite long-term global-mean and/or hemispheric mixing ratio estimates. Thus, while often not

853 entirely independent, as the studies use the same original data sources or we rely on some studies' previous derivations, we

854 here provide a comparison to a selection of the literature. Specifically, in addition to the comparisons with NOAA marine

855 boundary layer, WDCGG and NASA Aqua satellite data, we discuss some instances where our results show substantial

856 differences compared to earlier studies that have derived hemispheric or global means from instrumental data (Montzka et al.

857 2014, Rigby et al. 2014), from firn data (Butler et al. 1999, Trudinger et al. 2016) or are themselves composites of multiple

858 data sources (Martinerie et al. 2009, Velders et al. 2014, WMO 2014). The comparisons are shown in the panels f, g, and h of

859 the factsheets for each gas (Figure 2, Figure 4, Figure 5, and Figure 23 to Figure 62).

860 Martinerie et al. (2009) provided high latitude northern hemisphere data for atmospheric mixing ratios, used by (and made

861 available in the supplement of) Buizert et al. (2012). For CO_2, the Martinerie data set has, as expected for the high northern

862 latitudes, a very strong seasonal cycle, stronger than our northern hemispheric cycle (Figure 2f, g, and h). The long-term mixing

863 ratio trend over time in the Martinerie CO_2 record seems similar to the global CMIP5 data set which in turn was based on

864 previous Law Dome data, indicating a slight local maximum in 1890 and lower 1940s plateau (cf. Figure 2g and Figure 9).

865 For CH_4, the Martinerie et al. record shows a comparable, yet again stronger, seasonality. The annual means are very

866 comparable to our derivation (compare the high latitude red circles, indicating annual-mean station averages of our analysis

867 and Martinerie et al. data as shown in Figure 4f), although there are some steps in annual means in the Martinerie et al. data

868 set around 1956 and 1975, which are not present in our dataset (Figure 4f). For earlier times, i.e. between 1860 to 1920s, the

869 Martinerie annual mean is closer to our global-mean, not the high-latitude estimates, as our study assumes a large latitudinal

870 gradient based on the NEEM and Law Dome data differences (Methods) (Figure 4g).

871 For CCl_4, the Martinerie data show a lower increase from 1955 to the late 1960s and strong increase around 1970. The firn

872 data by Butler et al. (1999) suggests an earlier start of atmospheric mixing ratio increases around 1890, and then slightly lower

873 levels over 1960 to 1990 compared to the WMO (2014), Velders et al. (2014) timeseries to which we nudge our 2-D fields.

874 The findings by Sturrock et al. (2002) suggest an onset of atmospheric mixing ratios around 1920 (Figure 5f therein). The

875 NOAA global mean that is available from 1992 onwards (Montzka et al. (1999) updated at

876 http://www.esrl.noaa.gov/gmd/hats/combined/CCl4.html) and indicates initially slightly higher global mean estimates than our

877 derivation, which is for the instrumental period based on 6 AGAGE and 13 NOAA HATS stations (Figure 23f, g, h).

878 For CFC-11 (Figure 24g), the NOAA Montzka reconstruction of the global-mean is slightly higher (1 pptv) than ours, which

879 is almost identical to the WMO (2014) and Velders data (2014). Those differences presumably result from differences in

880 station coverage, different calibration scales and air sampling and analysis techniques between the networks. The seasonalities

881 show comparable amplitudes, as they do for CFC-12 (Figure 25h). With CFC-115, our study follows the historical shape of

882 the WMO (2014) record, with Velders (2014) being slightly lower (~0.5 pptv) (Figure 28f).

883   For CH_2Cl_2, the in situ instrumental record we use only reaches back to 1994, although the Cape Grim air archive record goes

884   back to 1978. From 1994 to 2003, the northern latitude measurements imply a mixing ratio reduction from 40 to 30 pptv,

885   whereas the southern hemispheric measurements are almost flat during that time. Similarly, the southern hemispheric firn

886   reconstructions (Trudinger et al. 2004) indicate an almost flat southern hemispheric evolution from 1997 onwards (Figure 29f).

887   We note however that there are substantial uncertainties in the pre-1995 mixing ratios, as e.g. Koppmvann (1993) reported 18

888   pptv and 36 pptv average mixing ratios for the southern hemispheric and northern hemispheric measurements from a 1989

889   Atlantic transect ship measurement campaign (not shown in the figure). This could imply a global average value of

890   approximately 27 pptv in 1989, instead of the 20 pptv assumed in this study – although different calibration scales might

891   contribute to this difference. Recent seasonality and increases of CH_2Cl_2 are closely matching other time series, such as the

892   AGAGE monthly global means from the Medusa instruments (Figure 29f), although there is a slight offset in the absolute

893   level, possibly caused by our study not sorting out data points from so-called pollution events in the case of CH_2Cl_2.

894   For CH_3Br, our CMIP6 recommendations match very closely the NOAA (Montzka et al. (2003) updated on

895   ftp://ftp.cmdl.noaa.gov/hats/methylhalides/ch3br/flasks) and AGAGE global means (2014) after 1995. Before then, the Butler

896   (1999) global-mean firn reconstruction coincides closely with our southern-hemispheric mean. The 2004 firn reconstruction

897   by Trudinger (2004) is close to the southern hemispheric mean, but shows somewhat more variation than the smooth

898   exponential increase assumed by this study, WMO (2014) and Velders et al. (2014).

899   For CH_3CCl_3, the overall agreement between the different (although not independent) studies considered here is excellent, for

900   example the high northern latitude data in Martinerie et al. (2009) in the south pole firn data reconstruction (Montzka et al.

901   2010), approximately in line also with the findings by Sturrock et al. (2002).

902   The atmospheric mixing ratios of CH_3Cl show a strong seasonal cycle, as is to be expected from the short lifetime due to the

903   OH-related sink. As in the case of methyl bromide (CH_3Br), the pre-instrumental period before 1995 implies a number of

904   uncertainties. Here, we follow again the WMO (2014) and Velders et al. (2014) reconstruction that are in line with shape of

905   the Butler et al. firn reconstructions. However, we note that the more recent Trudinger et al. (2004) reconstruction indicates

906   both a significantly lower mixing ratio for southern latitudes in the 1970s and a smoother increase compared to the more sudden

907   rise of mixing ratios around 1940 as implied in this study (Figure 32g).

908   As briefly discussed in section 3.4, the $CHCl_3$ history in this study relies on the Worton et al. (2006), reconstruction, whose

909   shape is similar to Trudinger et al. (2004), although the latter is indicates lower global mean mixing ratios and not the

910   diminishing latitudinal gradient suggested by Worton et al. (2006). The implied pre-industrial value of around 6 pptv should

911   be investigated in the future (Figure 33).

912   For Halon-1211, the recent study by Vollmer et al. (2016) and also the earlier study by Sturrock et al. (2002) (not shown)

913   suggest slightly higher initial mixing ratios (around 1975 to 1988) compared to the initially-lower and then larger exponential

914   increase we assumed by following Velders (2014). After 1990 the southern hemispheric reconstruction by the Bristol and

915   CSIRO models (Vollmer et al. 2016) are slightly lower and hence the latitudinal gradient slightly larger than what we derived

916   from the AGAGE and NOAA station data, but the differences are small (Figure 34f). Similarly, the very early mixing ratio

917   increases of the Halon-1301 between 1970 and 1978 are higher in the Vollmer (2016) study, and again the more recent years

918   from 2007 onwards (Figure 35h) are higher in Vollmer. In those latter years, our aggregation of AGAGE and NOAA station

919 data however suggests slightly lower mixing ratios, although the absolute difference (0.05 pptv) is within the measurement
920 uncertainty and the overall agreement is very good.

921 Halon-2402 is likely the most obvious example, where a shifting measurement spatial coverage density can lead to small jumps
922 in latitudinal gradients or global means (Figure 36f and h). The overall mixing ratios are very small and the early agreement
923 between the WMO (2014) time series and the Vollmer et al. (2016) findings is very good. In 2009, when data coverage
924 increased, the latitudinal gradient is suggested to suddenly decrease, which is likely an artefact of the assimilation procedure
925 that is only able to cope with time-varying data coverage to a certain degree (Methods). However, overall, the implied shifts
926 of 0.02 pptv are negligible in the larger picture, and certainly negligible for radiative forcing, as the shift in Southern
927 hemispheric radiative forcing is equivalent to only about 0.000003 W/m^2 (Figure 36h).

928 For HCFC-142b our derived global-mean is in the middle of the AGAGE and NOAA network averages, despite our study
929 including those data points that are subject to 'pollution' events in the case of HCFC-142b, with large positive outliers (Figure
930 39f), similar as in the case of HFC-134a (Figure 53f). Pollution events might however be contributing to the difference between
931 our HFC-152a global-means and the two independently derived network global means for AGAGE and NOAA, which largely
932 exclude pollution events by e.g. using statistical methods (O'Doherty et al. 2001) (see Figure 55f).Two more issues can be
933 observed with HCFC-142b data. Firstly, our end of 2014 mixing ratios are somewhat uncertain and this case possibly wrongly
934 decreasing, which results from the smooth annual mean representation and our assimilation procedure. The differences are
935 again very small and negligible in radiative forcing terms, but a smooth connection will have to be designed for the adjacent
936 datasets representing SSP-RCP scenarios. Secondly, since 2010, our estimates for the HCFCs, namely HCFC-22 (Figure 37f),
937 HCFC-141b (Figure 38f) and HCFC-142b (Figure 39f) indicate smaller increases than implied by Velders et al. (2016). As the
938 early study by Sturrock et al. (2002), our study represents the slow onset of HFC-142b mixing ratios in between 1960 and
939 1990 as shown in WMO (2014) and Velders et al. (2014).

940 For the three main PFCs, i.e. CF$_4$ (Figure 48), C$_2$F$_6$ (Figure 40), and C$_3$F$_8$ (Figure 41), we find a similar and good agreement
941 of the main studies. The Trudinger et al. (2016) time series are slightly below those suggested by Mühle et al. (2010b) (~0.5
942 pptv, ~0.1 pptv, ~0.01 pptv, respectively), but the overall agreement again is very good. The outliers are the previously
943 recommended CMIP5 mixing ratios (Meinshausen et al. 2011b) for these gases, which were at the time not yet based on either
944 the Trudinger et al. (2016) or Mühle et al. (2010b) studies. As mentioned above, the mixing ratios of the lesser important PFCs,
945 C$_4$F$_{10}$ (Figure 42), C$_5$F$_{12}$ (Figure 43), C$_6$F$_{14}$ (Figure 44), C$_7$F$_{16}$ (Figure 45) and C$_8$F$_{18}$ (Figure 46) are based on the Ivy et al.
946 (2012) reconstructions, with reversing latitudinal gradients in the case of C$_6$F$_{14}$, C$_7$F$_{16}$, and C$_8$F$_{18}$, which are unexplained so far
947 and require further confirmation. Our historical c-C$_4$F$_8$ mixing ratios are based on the study by Oram et al. (2012) with assumed
948 conversions of the Cape Grim measurements to northern hemispheric and global-averages.

949 For HFC-43-10mee, we based our trajectory on the NH and SH estimates of Arnold et al. (2014) with relatively small latitudinal
950 gradient and hemispheric means being informed by the recently available observations since 2010 from the AGAGE Medusa
951 instruments (Figure 51f). Note that the difference for HFC-365mfc data (Figure 59) between the station data and those
952 published in Montzka (2014) reflects a difference that now vanished after a correction to the NOAA calibration scale since the
953 publication of the Montzka et al. (2014) study. All studies are now in relatively close alignment with the shown AGAGE
954 network average, the Vollmer et al. (2011) study and our derivation (which is slightly lower, <0.1ppt). The air archive and
955 AGAGE network analysis by Vollmer et al. (2011) investigated in addition the HFCs HFCs-236fa, HFC-227ea, and HFC-

956 245fa. Those results are closely aligned with the ones constructed here on the basis of the WMO AGAGE network average
957 estimates (Figure 57, Figure 56, Figure 58).

958 Similar to our study, there are also studies that assimilate a wide range of gases with latitudinal and seasonal variation. For
959 example, the AGAGE network assimilation with a 12-box model and optimization approach to reconcile emissions and mixing
960 ratios (Rigby et al. 2011, Rigby et al. 2013) produces 4 semi-hemispheric concentration timeseries with 3 vertical levels (Rigby
961 et al. 2014). Those studies based on AGAGE data are more comprehensive than this one, as both emissions and concentrations
962 as well as lifetimes are optimized and reconciled. In our case, we only assimilate AGAGE and NOAA observations to derive
963 atmospheric mole fractions in 15 degree latitudinal bands (methods).

964 **6   Limitations**

965 Even though the presented dataset of historical surface greenhouse gas concentrations is – to our knowledge - more
966 comprehensive than other composite datasets before, there are a number of key limitations.

967 First of all, the dataset was assimilated from a number of sources in order to provide a common starting point for global climate
968 models. Thus, for example, the data was not designed to perform as a starting point for inversion studies, which estimate
969 emissions, or studies of biogeochemical processes. Those studies tend to require pure observations, rather than partly
970 interpolated composite products. This warning in terms of our data use is especially important for the fine-grid interpolation
971 we present. The 0.5-degree mean-preserving smooth interpolation should not be misinterpreted to actually portray
972 measurement information at such a fine scale.

973 Secondly, the purpose of forcing climate models correctly would best be accomplished by vertically resolved latitudinal and
974 longitudinal fields, which (in the case of CO_2) even include a diurnal cycle. Our latitudinally and monthly resolved dataset
975 offers climate models already an option to capture some key variability compared to the global and annual mean CMIP5
976 concentration recommendation (Meinshausen et al. 2011b). However, a correct implementation of this additional monthly and
977 latitudinal variability is also dependent on an appropriate propagation of the surface signal throughout the troposphere and
978 stratosphere. For example, some studies (Olsen and Randerson 2004) find that column CO_2 is found to only exhibit roughly
979 half of the latitudinal gradient and seasonal variation compared to the surface mixing ratios. In the CESM1 model (Hurrell et
980 al. 2013) with prescribed surface greenhouse gas concentrations, the vertical propagation of CO_2 mixing ratio is assumed to
981 be constant. In the case of the other greenhouse gases (CH_4, N_2O and CFCs) a constant mixing ratio in the troposphere and a
982 decrease of mixing ratio in the stratosphere is assumed in CESM1. In particular, the scale heights in the stratosphere of these
983 trace gases depend on latitude, which produces a more realistic stratospheric distribution. We recommend vertical extensions
984 to our surface mixing ratio reconstructions only in the case that the model has no intrinsic transport model or extension
985 parameterisation. Furthermore, we do not include the longitudinal variation. Again, in particular for CO_2, this longitudinal
986 variation might be systematic given the land/ocean contrast. For example, the MPI-ESM-LR model indicates systematically
987 higher surface CO_2 mixing ratio over land, which in turn would have a radiative effect (cf. Figure 14).

988 Thirdly, our assimilation procedure is a rather simple one and does not attempt to offset potential biases due to day and night-
989 time sampling biases for CO_2 in the case of some flask measurements, or whether including pollution events would bias the
990 latitudinal averages towards higher than current average values. In a world with continuing point sources, screening out

991   pollution effects might cause proposed averages to lag slightly behind the true average mixing ratio. The question is whether
992   the correlation between sampling locations and source locations will inherently bias the average mixing ratios towards higher-
993   than true average values in our assimilation for species, where we include pollution events. For most substances we do not find
994   any systematic difference between the network averages from AGAGE or NOAA, although there are some species (e.g. HFC-
995   152a, see Figure 55) for which our higher mixing ratio reconstructions could in part be explained by this different method.

996   The opposite might also be the case, i.e. that despite including some pollution events, there could still be an inherent
997   underestimation of true zonal means. That is because the NOAA and AGAGE sampling stations we are sourcing our raw data
998   from tend to be biased to remote/clean-air/well mixed conditions and this will have implications for our latitudinal gradient
999   and seasonal cycle. Where there are continental sites they are often at altitude, and when flasks are sampled they are generally
1000   for mid-afternoon when mixing is largest. Hence the fitted latitudinal gradient for CO_2 at least might be closer to the NOAA
1001   marine boundary layer product than to a true zonal mean. Also the seasonal cycle will be more representative of marine
1002   conditions than continental ones (where a diurnal rectifier could potentially dampen or offset seasonally low mixing ratios in
1003   summer in the case of CO_2). This bias towards remote measurements tends to increase the further back in time we go.

1004   Another limitation of our study is related to the different calibration scales of atmospheric gas measurements. In our data
1005   assimilation method with no scale conversion between the SIO and NOAA scales of the AGAGE and NOAA networks
1006   (Methods), a time-varying difference between the scales or time-varying coverage from one network to another can lead to
1007   spurious trends in the derived mixing ratios. We argue that our "middle of the road" data assimilation method across the two
1008   networks is however one justifiable, yet not the only viable assimilation method. The reasons for our chosen approach are a)
1009   uncertainties in absolute mole fractions estimates are small compared to other uncertainties that would affect the radiative
1010   forcing in climate models, b) alternative "pure" scale data assimilation could only deal with the trend uncertainty, not with the
1011   uncertainty arising for absolute mole fraction values (assuming that both the SIO and NOAA scales are equally sound), c) we
1012   intend to be "network"-neutral and d) a single "in-between" mixing ratio estimate is likely the most appropriate for the primary
1013   application purpose (historical simulations of climate models) of the provided data. However, future researchers are
1014   encouraged to work directly with the principal investigators of the two networks to devise data assimilation methods that would
1015   be better suited for alternative applications, such as uncertainty estimates of inverse emissions etc. A clear limitation of our
1016   data produce is hence our implicit "in between" scale, with time-varying influences from measurements under the one or other
1017   network. Thus, differences to "pure" SIO or NOAA scale will partly arise from this "scale" issue.

1018   Another important limitation of our study is that we do not provide uncertainty estimates. This is primary related to the fact
1019   that the purpose of this study was to provide a consolidated dataset for climate model experiments. Those models experiments
1020   can only be performed a limited number of times given today's computational resources. The experimental protocol hence
1021   does not foresee an ability to vary greenhouse gas mixing ratios within its uncertainties, given that many aspects of climate
1022   models are affected by more substantial uncertainties, such as aerosols. The original AGAGE and NOAA (sometimes monthly
1023   averaged) sampling data points shown in the Factsheets (see panels f, g, and h) can however provide an indication of
1024   uncertainties and the spread in observations.

1025   Note that our choice of predictor for the CO_2 seasonality change (namely the product of CO_2 mixing ratio and global-mean
1026   temperature deviation since pre-industrial) is subjective and using only CO_2 mixing ratio or temperature would have yielded

1027   in a larger seasonality difference between current and pre-industrial times. Further research will be necessary to obtain an

1028   optimal proxy for pre-observational CO_2 seasonality changes.

1029   Similarly, our common explanatory variable for regressions of latitudinal gradients, i.e. global emissions, is an approximation.

1030   Ideally, the time-changing latitudinal distribution of emissions would be taken into account in those backward extensions of

1031   the latitudinal gradient over time.

1032

7 Conclusion

Glacial and interglacial cycles are driven by Milankovich cycles. Ice core measurements over the past 800k years reveal how atmospheric greenhouse gas mixing ratios of CO_2, CH_4 and N_2O varied in turn, indicating various feedback mechanisms. With the arrival of homo sapiens, initially deforestation and agriculture, and then the onset of the fossil-fuel driven industrial revolution, the atmospheric composition changed. Unprecedented over this time of the ice core record, CO_2, CH_4 and N_2O mixing ratios shot upwards, with CO_2 reaching a historical mark of 400 ppmv in 2015. Recently, synthetic greenhouse gases arising from refrigerants, solvents, insulation appliances and even gas-cushioned shoe soles added to the warming effect, the radiative forcing. As the IPCC AR5 found, the most likely warming contribution from these greenhouse gases is now higher than the observed warming (Figure TS.10 in IPCC AR5 (IPCC 2013). That means that without the human activities that happen to cool the planet, namely the aerosols we emit, observed warming would have been even greater than what has already been experienced.

In this study, we compile a set of greenhouse gas histories over the last 2000 years – based on numerous efforts by the scientific community to retrieve firn samples and ice cores in the most remote places on Earth, unlock their secrets by analyzing the enclosed air and by investing in a large network of in-situ and flask measurement stations across the planet. Our understanding of past climate change is vital to develop scenarios of the future and design humanities' response strategies in terms of mitigation and adaptation. Without the ongoing efforts to retrieve and monitor the composition of the planet's atmosphere, sometimes at risk (Lewis 2016), the future ahead of us remains shrouded in many uncertainties.

In this dataset, we attempted to provide a solid base for the next generation of climate and earth system models to further our understanding of past and future climate changes. Providing seasonal and latitudinal differences of the radiative forcing that drives the climate change across the globe, we can hope for an even more appropriate comparison between models and past land-ocean, regional land and oceanic temperature observations. Ignoring these seasonal and latitudinal differences can lead to different calculated climate impacts of GHG emissions. Thus, accurately including this variability is a necessary condition to accurately comparing model calculations and observations and to understanding the reasons for the differences. Those agreements and disagreements between what models and past observations tell us, will then allow us to calibrate our understanding of the earth system, its non-linearities and its many feedback cycles, the human influences and natural variabilities – in jargon called 'detection and attribution'. We have been engaging in a unique experiment with our climate. In order to achieve the limits we set forth in the Paris Agreement of how much further we push the planetary system out of the boundaries it has been in for thousands of years (up to 2°C and 1.5°C, respectively) and in order to cope with the climate change committed to already, the next generation of climate models will be vital. This study into the main past driver of human-induced climate change intends to provide the basis for this further examination of a tremendous challenge we find ourselves in.

8   Code Availability

The matlab and R code that was used to assimilate the raw data is available from the authors on request.

9   Data Availability

A supplementary data table is available with global and annual mean mole fractions. The complete dataset with latitudinally and monthly resolved data in netcdf format is available via https://pcmdi.llnl.gov/search/input4mips/. Additional data formats, i.e. CSV, XLS, MATLAB .mat files of the same data are also available via www.climatecollege.unimelb.edu.au/cmip6. The respective raw data used in this study is available from the original referenced data providers on request.

10   Acknowledgements

The authors would first and foremost like to thank the large community of scientists, research assistants and measurement technicians that were involved collecting the firn, ice core and atmospheric in-situ and flask measurements across the world. The primary networks AGAGE and the Cooperative Air Sampling Network managed by NOAA deserve the most credit, including all its individual researchers and the networks' policy to make the raw data available to the broader scientific community. In particular, we thank the following researchers for invaluable efforts to collect, screen and make available NOAA network data: Ed Dlugokencky, Pieter Tans, David Nance, Bradley Hall, Geoff Dutton, James Elkins, Debra Mondeel. We also like to thank the Editor O. Morgenstern for helpful suggestions.

Furthermore, we thank the ESM CMIP5 modelling groups who contributed to the 5th Climate Model Intercomparison project and whose data we analyzed.

Attributions: MM designed the study. EV wrote most of the data analysis and read-in routines together with MM. KL analysed the CMIP5 ESM models and produced related figures. Other figures and the factsheets were produced by MM. AN provided an initial literature overview. All authors wrote, commented on and/or discussed the manuscript based on a first draft by MM. NM designed the mean-preserving interpolation routines. Multiple authors provided vital data.

1086

1087

1088

1089

1090

1091

1092

1093   **11   Tables**

1094

1095 **Table 1 - Derivation and construction of CMIP6 mixing ratio fields for CO₂, CH₄ and N₂O, as shown in Figure 22 and described in**
1096 **Methods.**

Gas	Time period	Main data source	Global and annual-mean $\overline{C_{global}}$	Seasonality $\hat{S}_{l,m}$	Seasonality Change $\Delta S_{l,m}$	Latitudinal gradient $\hat{L}$
CO₂	1984-2013/2014	NOAA ESRL Carbon Cycle Cooperative Global Air Sampling Network, 1968-2014. Version: 2015-08-03, monthly station averages (NOAA ESRL GMD 2014c, NOAA ESRL GMD 2014b, NOAA ESRL GMD 2014a, Dlugokencky 2015b)	Calculated based on observational data source (section 2.1.3).	Mean over 1984-2013 period.	Leading EOF of residuals from observation	Two leadings EOF and their scores derived from residuals from observations. (2014: optimized to match observational data).
	Before 1984	Law Dome (Etheridge et al. 1998c, MacFarling Meure et al. 2006, Rubino et al. 2013)	Optimized to match smoothed median approximation of Law Dome record	Kept constant as above	regressed against product of CO₂ mixing ratio and surface air temperature change since pre-industrial	The score for EOF1 is regressed against global annual fossil fuel & industry emissions (Boden et al. 2013). Score for EOF2 linearly returned to zero in 1850.
CH₄	1985 to 2013/2014	AGAGE monthly station means, incl. pollution events ('.mop') (Cunnold et al. 2002) & NOAA ESRL monthly station station data (Dlugokencky 2015a)	Calculated based on observational data source (section 2.1.3).	Mean over 1985-2013 period. Applied as relative seasonality	Assumed zero	Two leadings EOF and their scores derived from residuals from observations. (2014: optimized to match observational data).
	Before 1985	Law Dome (Etheridge et al. 1998b, MacFarling Meure et al. 2006) & NEEM (Rhodes et al. 2013)	Optimized to match smoothed Law Dome record & NEEM firn data			The score for EOF1 is regressed against global annual fossil fuel & industry emissions (Gütschow et al. 2016). Score for EOF2 kept constant before in situ instrumental period.
N₂O	1990 to 2013/2014	AGAGE monthly station means, incl. pollution events (Prinn et al. 1990) & Combined Nitrous Oxide data (monthly station averages) from the NOAA/ESRL Global Monitoring Division.	Calculated based on observational data source (section 2.1.3).	Mean over 1990-2013 period. Applied as relative seasonality	Assumed zero	Two leadings EOF and their scores derived from residuals from observations. (2014: optimized to match observational data).
	Before 1990	Law Dome (MacFarling Meure et al. 2006)	Optimized to match smoothed Law Dome record.			The score for EOF1 is regressed against global annual fossil fuel & industry emissions (Gütschow et al. 2016). Score for EOF2 kept constant before in situ instrumental period.

1097

1098

1099 **Table 2- Raw data used for CO₂ surface mixing ratio field derivation**

Dataset	Reference / URL	Stations / Location	Used for	Description / Filtering
NOAA ESRL GMD Surface Flask data.	(Komhyr et al. 1983, Komhyr et al. 1985, Thoning 1987, Conway et al. 1988, Tans et al. 1989, Thoning et al. 1989, Tans et al. 1990a, Tans et al. 1990b, Conway et al. 1994, Thoning et al. 1995, Zhao and Tans 2006)	81 stations of the surface flask network[a]: ABP, ALT, AMS, AOC, ASC, ASK, AVI, AZR, BAL, BHD, BKT, BME, BMW, BRW, BSC, CBA, CGO, CHR, CIB, CMO, CPT, CRZ, DRP, DSI, EIC, GMI, GOZ, HBA, HPB, HSU, HUN, ICE, IZO, KCO, KEY, KUM, KZD, KZM, LEF, LLB, LLN, LMP, MBC, MEX, MHD, MID, MKN, MLO, NAT, NMB, NWR, OPW, OXK, PAL, PAO, POC, PSA, PTA, RPB, SCS, SDZ, SEY, SGI, SGP, SHM, SMO, SPO, STC, STM, SUM, SYO, TAP, THD, TIK, USH, UTA, UUM, WIS, WLG, WPC, ZEP	Observational period estimation of global mean, latitudinal gradient seasonality and seasonality change over 1984-2013. Optimization of global mean and latitudinal gradient in 2014 and before 1984.	This study used monthly average data that uses all sample points, which have an 'accepted' flag, i.e. initial two dots ('..*') in the three digit flag.
NOAA ESRL GMD Surface Flask data.	(NOAA ESRL GMD 2014c, NOAA ESRL GMD 2014b, NOAA ESRL GMD 2014a)	BRW, MLO, SMO		
Law Dome	(Etheridge et al. 1996, Etheridge et al. 1998c, Rubino et al. 2013) (MacFarling Meure et al., 2006)	Law Dome ice core	Used as input for piecewise 3rd-degree polynomial smoothing over remainder of years 0 to 1966.	

1100 [a] See station descriptions here: http://www.esrl.noaa.gov/gmd/dv/site/site_table.html

1101

1102 **Table 3 – Global-mean GHG surface mixing ratios for year 2011 and 2014, including a comparison to 2011 NOAA, AGAGE and**
1103 **UCI estimates – as provided in IPCC AR5 WG1. Unit is pptv, unless otherwise stated.**

Rank of Abundane	Species	*2014*	*2011*	*2011*	*2011*	*2011*
		CMIP6 (This Study)		UCI	SIO b/AGAGE	NOAA
1	CO2 (ppmv)	397.55	390.94		390.48 ± 0.28	390.44 ± 0.16
2	CH4 (ppbv)	1831.47	1813.07	1798.1 ± 0.6	1803.1 ± 4.8	1803.2 ± 1.2
3	N2O (ppbv)	326.99	324.16		324.0 ± 0.1	324.3 ± 0.1
4	CH3Cl	539.54	534.17			
5	CFC-12	520.58	528.53	525.3 ± 0.8	529.5 ± 0.2	527.4 ± 0.4
6	CFC-11	233.08	238.25	237.9 ± 0.8	236.9 ± 0.1	238.5 ± 0.2
7	HCFC-22	229.54	214.56	209.0 ± 1.2	213.4 ± 0.8	213.2 ± 1.2
8	CCl4	83.07	86.06	87.8 ± 0.6	85.0 ± 0.1	86.5 ± 0.3
9	CF4	81.09	79.04		79.0 ± 0.1	
10	HFC-134a	80.52	62.85	63.4 ± 0.9	62.4 ± 0.3	63.0 ± 0.6
11	CFC-113	72.71	74.64	74.9 ± 0.6	74.29 ± 0.06	74.40 ± 0.04
12	CH2Cl2	36.35	29.49			
13	HFC-23	26.89	24.13		24.0 ± 0.3	
14	HCFC-141b	23.81	21.56	20.8 ± 0.5	21.38 ± 0.09	21.4 ± 0.2
15	HCFC-142b	22.08	21.35	21.0 ± 0.5	21.35 ± 0.06	21.0 ± 0.1
16	CFC-114	16.31	16.36			
17	HFC-125	15.36	10.46		9.58 ± 0.04	
18	HFC-143a	15.25	11.92		12.04 ± 0.07	
19	CHCl3	9.90	8.95			
20	CFC-115	8.43	8.39			
21	HFC-32	8.34	5.17			
22	SF6	8.22	7.31		7.26 ± 0.02	7.31 ± 0.02
23	HFC-152a	7.73	7.89		6.4 ± 0.1	
24	CH3Br	6.69	7.11			
25	C2F6	4.40	4.17		4.16 ± 0.02	
26	Halon-1211	3.75	4.05			
27	CH3CCl3	3.68	6.31	6.8 ± 0.6	6.3 ± 0.1	6.35 ± 0.07
28	Halon-1301	3.30	3.23			
29	HFC-245fa	2.05	1.56			
30	SO2F2	2.04	1.74			
31	c-C4F8	1.34	1.23			
32	NF3	1.24	0.83			
33	HFC-227ea	1.01	0.74			
34	HFC-365mfc	0.77	0.56			
35	C3F8	0.60	0.56			
36	Halon-2402	0.43	0.45			
37	C6F14	0.28	0.27			
38	HFC-43-10mee	0.25	0.22			
39	C4F10	0.18	0.17			
40	HFC-236fa	0.13	0.10			
41	C5F12	0.13	0.12			
42	C7F16	0.13	0.12			
43	C8F18	0.09	0.09			

1104

1105 **Table 4 – 1pctCO2: Global-mean annual-mean surface CO₂ mixing ratios for idealized CMIP6 experiments 1pctCO2. All other gases,**
1106 **as in picontrol run (see Table 5). The value 284.317 ppmv with 3-digit precision in year 1850 is increased by 1% per year.**

YEAR	CO_2 (PPMV)	YEAR	CO_2 (PPMV)	YEAR	CO_2 (PPMV)	YEAR	CO_2 (PPMV)	YEAR	CO_2 (PPMV)
1850	284.32	1900	467.60	1950	769.02	2000	1264.76	2050	2080.07
1851	287.16	1901	472.27	1951	776.71	2001	1277.41	2051	2100.87
1852	290.03	1902	477.00	1952	784.48	2002	1290.18	2052	2121.88
1853	292.93	1903	481.77	1953	792.33	2003	1303.09	2053	2143.10
1854	295.86	1904	486.58	1954	800.25	2004	1316.12	2054	2164.53
1855	298.82	1905	491.45	1955	808.25	2005	1329.28	2055	2186.17
1856	301.81	1906	496.36	1956	816.34	2006	1342.57	2056	2208.03
1857	304.83	1907	501.33	1957	824.50	2007	1356.00	2057	2230.11
1858	307.87	1908	506.34	1958	832.74	2008	1369.56	2058	2252.42
1859	310.95	1909	511.40	1959	841.07	2009	1383.25	2059	2274.94
1860	314.06	1910	516.52	1960	849.48	2010	1397.08	2060	2297.69
1861	317.20	1911	521.68	1961	857.98	2011	1411.06	2061	2320.67
1862	320.38	1912	526.90	1962	866.56	2012	1425.17	2062	2343.87
1863	323.58	1913	532.17	1963	875.22	2013	1439.42	2063	2367.31
1864	326.82	1914	537.49	1964	883.97	2014	1453.81	2064	2390.98
1865	330.08	1915	542.87	1965	892.81	2015	1468.35	2065	2414.89
1866	333.38	1916	548.29	1966	901.74	2016	1483.03	2066	2439.04
1867	336.72	1917	553.78	1967	910.76	2017	1497.86	2067	2463.43
1868	340.09	1918	559.31	1968	919.87	2018	1512.84	2068	2488.07
1869	343.49	1919	564.91	1969	929.07	2019	1527.97	2069	2512.95
1870	346.92	1920	570.56	1970	938.36	2020	1543.25	2070	2538.08
1871	350.39	1921	576.26	1971	947.74	2021	1558.68	2071	2563.46
1872	353.89	1922	582.03	1972	957.22	2022	1574.27	2072	2589.09
1873	357.43	1923	587.85	1973	966.79	2023	1590.01	2073	2614.98
1874	361.01	1924	593.72	1974	976.46	2024	1605.91	2074	2641.13
1875	364.62	1925	599.66	1975	986.22	2025	1621.97	2075	2667.55
1876	368.26	1926	605.66	1976	996.08	2026	1638.19	2076	2694.22
1877	371.95	1927	611.71	1977	1006.04	2027	1654.57	2077	2721.16
1878	375.67	1928	617.83	1978	1016.11	2028	1671.12	2078	2748.38
1879	379.42	1929	624.01	1979	1026.27	2029	1687.83	2079	2775.86
1880	383.22	1930	630.25	1980	1036.53	2030	1704.71	2080	2803.62
1881	387.05	1931	636.55	1981	1046.89	2031	1721.76	2081	2831.65
1882	390.92	1932	642.92	1982	1057.36	2032	1738.97	2082	2859.97
1883	394.83	1933	649.35	1983	1067.94	2033	1756.36	2083	2888.57
1884	398.78	1934	655.84	1984	1078.62	2034	1773.93	2084	2917.46
1885	402.76	1935	662.40	1985	1089.40	2035	1791.67	2085	2946.63
1886	406.79	1936	669.02	1986	1100.30	2036	1809.58	2086	2976.10
1887	410.86	1937	675.71	1987	1111.30	2037	1827.68	2087	3005.86
1888	414.97	1938	682.47	1988	1122.41	2038	1845.95	2088	3035.92
1889	419.12	1939	689.29	1989	1133.64	2039	1864.41	2089	3066.28
1890	423.31	1940	696.19	1990	1144.97	2040	1883.06	2090	3096.94
1891	427.54	1941	703.15	1991	1156.42	2041	1901.89	2091	3127.91
1892	431.82	1942	710.18	1992	1167.99	2042	1920.91	2092	3159.19
1893	436.14	1943	717.28	1993	1179.67	2043	1940.12	2093	3190.78
1894	440.50	1944	724.46	1994	1191.46	2044	1959.52	2094	3222.69
1895	444.90	1945	731.70	1995	1203.38	2045	1979.11	2095	3254.91
1896	449.35	1946	739.02	1996	1215.41	2046	1998.90	2096	3287.46
1897	453.84	1947	746.41	1997	1227.57	2047	2018.89	2097	3320.34
1898	458.38	1948	753.87	1998	1239.84	2048	2039.08	2098	3353.54
1899	462.97	1949	761.41	1999	1252.24	2049	2059.47	2099	3387.08
								2100	3420.95

1107

1108

1109

Table 5 – picontrol: Global- and annual-mean surface mixing ratios for the picontrol CMIP6 experiment. The hemispheric and latitudinally resolved mixing ratios for 43 greenhouse gases and three aggregate equivalent mixing ratios are provided in the accompanying historical run dataset for the year 1850. The complexity reduction options for capturing all GHGs with fewer species than 43 are indicated in the Table as Option 1, Option 2, and Option 3, with 'x' denoting relevant columns under each option.

Years	CO_2	CH_4	N_2O	CFC-12-eq	HFC-134a-eq	CFC-11-eq	CFC-12	Other
Option 1	x	x	x				x	x
Option 2	x	x	x			x	x	
Option 3	x	x	x	x	x			
Units:	ppmv	ppbv	ppbv	pptv	pptv	pptv	pptv	
1850	284.317	808.25	273.02	16.51	19.15	32.11	0.00	All or a subset of other 39 individual gases, available in Supplementary

1114

Table 6 – abrupt4x: Global- and annual-mean surface mixing ratios for the idealized abrupt4x CMIP6 experiment. The hemispheric and latitudinally resolved mixing ratios for 43 greenhouse gases and three aggregate equivalent mixing ratios are provided in the accompanying historical run dataset, with the 1850 CO_2 mixing ratio of 284.317 being multiplied by four. The complexity reduction options for capturing all GHGs with fewer species than 43 are indicated in the Table as Option 1, Option 2, and Option 3, with 'x' denoting relevant columns under each option.

Years	CO_2	CH_4	N_2O	CFC-12-eq	HFC-134a-eq	CFC-11-eq	CFC-12	Other
Option 1	x	x	x				x	x
Option 2	x	x	x			x	x	
Option 3	x	x	x	x	x			
Units:	ppmv	ppbv	ppbv	pptv	pptv	pptv	pptv	
0 -150	1137.268	808.25	273.02	16.51	19.15	32.11	0.00	All or a subset of other 39 individual gases, available in Supplementary

1120

1121

1122 **Table 7 – historical: Global- and annual-mean surface mixing ratios for the historical CMIP6 experiments. The year-to-year and**
1123 **monthly resolved global, hemispheric and latitudinally resolved mixing ratios for 43 greenhouse gases and three aggregate equivalent**
1124 **mixing ratios are provided in the accompanying datasets over the time horizon year 0 (1 BC) to year 2014 AC. The complexity**
1125 **reduction options for capturing all GHGs with fewer species than 43 are indicated in the Table as Option 1, Option 2, and Option 3,**
1126 **with 'x' denoting relevant columns under each option (see section 2.1.10).**

Years	CO_2	CH_4	N_2O	CFC-12-eq	HFC-134a-eq	CFC-11-eq	CFC-12	Other
Option 1	x	x	x				x	x
Option 2	x	x	x			x	x	
Option 3	x	x	x	x	x			
Units:	ppmv	ppbv	ppbv	pptv	pptv	pptv	pptv	
1750	277.15	731.41	273.87	16.51	19.15	32.11	0.00	All or a subset of other 39 individual gases, available online
1850	284.32	808.25	273.02	16.51	19.15	32.11	0.00	
1851	284.45	808.41	273.09	16.51	19.15	32.11	0.00	
1852	284.60	809.16	273.17	16.51	19.15	32.11	0.00	
1853	284.73	810.40	273.26	16.51	19.15	32.11	0.00	
1854	284.85	811.73	273.36	16.51	19.15	32.11	0.00	
1855	284.94	813.33	273.47	16.51	19.15	32.11	0.00	
1856	285.05	814.80	273.58	16.51	19.15	32.11	0.00	
1857	285.20	816.45	273.68	16.51	19.15	32.11	0.00	
1858	285.37	818.36	273.76	16.51	19.15	32.11	0.00	
1859	285.54	820.40	273.90	16.51	19.15	32.11	0.00	
1860	285.74	822.31	274.06	16.51	19.15	32.11	0.00	
1861	285.93	824.40	274.24	16.51	19.15	32.11	0.00	
1862	286.10	827.03	274.42	16.51	19.15	32.11	0.00	
1863	286.27	830.17	274.57	16.51	19.15	32.11	0.00	
1864	286.44	833.60	274.72	16.51	19.15	32.11	0.00	
1865	286.61	836.89	274.88	16.51	19.15	32.11	0.00	
1866	286.78	840.36	275.05	16.51	19.15	32.11	0.00	
1867	286.95	844.00	275.21	16.51	19.15	32.11	0.00	
1868	287.10	847.25	275.39	16.51	19.15	32.11	0.00	
1869	287.22	850.13	275.56	16.51	19.15	32.11	0.00	
1870	287.35	852.44	275.72	16.51	19.15	32.11	0.00	
1871	287.49	853.99	275.90	16.51	19.15	32.11	0.00	
1872	287.66	855.23	276.08	16.51	19.15	32.11	0.00	
1873	287.86	856.17	276.25	16.51	19.15	32.11	0.00	
1874	288.06	857.82	276.42	16.51	19.15	32.11	0.00	
1875	288.29	859.47	276.59	16.51	19.15	32.11	0.00	
1876	288.52	860.86	276.74	16.51	19.15	32.11	0.00	
1877	288.75	862.38	276.86	16.51	19.15	32.11	0.00	
1878	288.99	864.14	277.00	16.51	19.15	32.11	0.00	
1879	289.22	866.28	277.13	16.51	19.15	32.11	0.00	
1880	289.47	868.70	277.27	16.51	19.15	32.11	0.00	
1881	289.74	870.98	277.37	16.51	19.15	32.11	0.00	
1882	290.02	873.25	277.49	16.51	19.15	32.11	0.00	
1883	290.26	875.60	277.59	16.51	19.15	32.11	0.00	
1884	290.51	878.15	277.70	16.51	19.15	32.11	0.00	
1885	290.80	881.03	277.80	16.51	19.15	32.11	0.00	
1886	291.10	883.84	277.89	16.51	19.15	32.11	0.00	
1887	291.41	886.93	278.00	16.51	19.15	32.11	0.00	
1888	291.76	889.93	278.08	16.51	19.15	32.11	0.00	
1889	292.11	893.16	278.19	16.51	19.15	32.11	0.00	
1890	292.46	896.38	278.27	16.51	19.16	32.11	0.00	
1891	292.82	899.67	278.35	16.51	19.16	32.11	0.00	
1892	293.17	903.53	278.44	16.51	19.16	32.11	0.00	
1893	293.48	907.27	278.55	16.51	19.16	32.11	0.00	
1894	293.79	910.48	278.69	16.51	19.16	32.11	0.00	
1895	294.08	913.23	278.83	16.51	19.16	32.11	0.00	
1896	294.36	914.77	278.94	16.51	19.16	32.11	0.00	
1897	294.65	916.27	279.05	16.51	19.16	32.11	0.00	
1898	294.95	919.02	279.16	16.51	19.16	32.11	0.00	
1899	295.30	922.28	279.31	16.51	19.16	32.11	0.00	
1900	295.67	925.55	279.45	16.51	19.16	32.11	0.00	
1901	296.01	928.80	279.61	16.51	19.16	32.11	0.00	

Years	CO$_2$	CH$_4$	N$_2$O	CFC-12-eq	HFC-134a-eq	CFC-11-eq	CFC-12	Other
1902	296.32	932.73	279.86	16.51	19.16	32.11	0.00	
1903	296.65	936.78	280.16	16.51	19.16	32.11	0.00	
1904	296.95	942.11	280.43	16.51	19.16	32.12	0.00	
1905	297.29	947.44	280.71	16.51	19.16	32.12	0.00	
1906	297.66	953.09	280.98	16.51	19.17	32.12	0.00	
1907	298.10	959.16	281.28	16.51	19.17	32.12	0.00	
1908	298.52	964.09	281.61	16.51	19.18	32.13	0.00	
1909	298.94	969.40	281.95	16.51	19.18	32.13	0.00	
1910	299.38	974.79	282.31	16.51	19.19	32.13	0.00	
1911	299.83	979.47	282.72	16.54	19.20	32.18	0.00	
1912	300.35	983.61	283.02	16.55	19.21	32.20	0.00	
1913	300.91	986.24	283.36	16.56	19.23	32.22	0.00	
1914	301.42	988.61	283.72	16.60	19.24	32.28	0.00	
1915	301.94	991.46	284.05	16.67	19.26	32.37	0.00	
1916	302.48	998.45	284.31	16.78	19.28	32.51	0.00	
1917	303.01	1,003.57	284.62	16.90	19.31	32.68	0.00	
1918	303.45	1,010.13	284.81	16.99	19.34	32.81	0.00	
1919	303.81	1,017.63	284.85	17.08	19.37	32.94	0.00	
1920	304.25	1,025.07	284.93	17.12	19.40	33.01	0.00	
1921	304.60	1,032.20	285.04	17.16	19.43	33.08	0.00	
1922	304.94	1,039.10	285.17	17.24	19.44	33.18	0.00	
1923	305.27	1,045.13	285.47	17.37	19.46	33.36	0.00	
1924	305.63	1,049.45	285.61	17.50	19.49	33.53	0.00	
1925	305.81	1,052.16	285.65	17.65	19.54	33.74	0.00	
1926	305.95	1,053.60	285.69	17.84	19.58	34.00	0.00	
1927	306.18	1,055.77	285.74	17.97	19.62	34.19	0.00	
1928	306.33	1,060.64	285.83	18.15	19.67	34.45	0.00	
1929	306.49	1,066.66	285.89	18.42	19.73	34.82	0.00	
1930	306.62	1,072.64	285.94	18.72	19.80	35.22	0.00	
1931	306.82	1,077.49	286.12	19.08	19.85	35.71	0.00	
1932	307.09	1,081.96	286.22	19.46	19.89	36.19	0.00	
1933	307.40	1,086.54	286.37	19.85	19.92	36.69	0.00	
1934	307.78	1,091.77	286.47	20.30	19.95	37.26	0.00	
1935	308.23	1,097.08	286.59	20.86	19.98	37.97	0.00	
1936	309.01	1,101.83	286.75	21.57	20.04	38.88	0.00	
1937	309.76	1,106.32	286.95	22.34	20.11	39.87	0.00	
1938	310.29	1,110.63	287.19	23.09	20.21	40.86	0.00	
1939	310.85	1,116.91	287.39	23.89	20.32	41.90	0.00	
1940	311.36	1,120.12	287.62	24.80	20.45	43.11	0.00	
1941	311.81	1,123.24	287.86	25.89	20.59	44.53	0.00	
1942	312.17	1,128.19	288.14	27.25	20.77	46.32	0.00	
1943	312.39	1,132.66	288.78	28.89	21.00	48.48	0.00	
1944	312.41	1,136.27	289.00	30.85	21.31	51.06	0.02	
1945	312.38	1,139.32	289.23	32.67	21.53	52.94	0.42	
1946	312.39	1,143.66	289.43	35.15	21.59	54.53	1.64	
1947	312.49	1,149.64	289.51	37.73	21.67	56.29	2.84	
1948	312.52	1,155.63	289.56	40.53	21.79	58.34	4.03	
1949	312.63	1,160.35	289.60	43.44	21.92	60.53	5.22	
1950	312.82	1,163.82	289.74	46.41	22.04	62.83	6.38	
1951	313.01	1,168.81	289.86	49.53	22.18	65.04	7.78	
1952	313.34	1,174.31	290.03	52.53	22.37	66.80	9.44	
1953	313.73	1,183.36	290.33	55.93	22.58	68.92	11.21	
1954	314.09	1,194.43	290.55	59.82	22.80	71.41	13.20	
1955	314.41	1,206.65	290.84	64.26	23.04	74.27	15.44	
1956	314.70	1,221.10	291.19	69.32	23.29	77.48	18.01	
1957	314.99	1,235.80	291.51	75.05	23.54	81.04	20.98	
1958	315.34	1,247.42	291.77	81.16	23.78	84.76	24.18	
1959	315.81	1,257.32	291.99	87.55	24.03	88.56	27.61	
1960	316.62	1,264.12	292.28	94.78	24.30	92.70	31.61	
1961	317.30	1,269.46	292.60	103.17	24.60	97.52	36.24	
1962	318.04	1,282.57	292.95	112.78	24.94	103.11	41.48	
1963	318.65	1,300.79	293.33	123.96	25.33	109.56	47.60	
1964	319.33	1,317.37	293.69	136.86	25.73	116.84	54.80	
1965	319.82	1,331.06	294.05	151.46	26.15	124.93	63.03	
1966	320.88	1,342.24	294.45	167.71	26.60	133.86	72.25	

Years	CO$_2$	CH$_4$	N$_2$O	CFC-12-eq	HFC-134a-eq	CFC-11-eq	CFC-12	Other
1967	321.48	1,354.27	294.86	185.88	27.09	143.77	82.61	
1968	322.39	1,371.65	295.27	206.27	27.67	154.88	94.26	
1969	323.25	1,389.34	295.68	229.03	28.28	167.24	107.29	
1970	324.78	1,411.10	296.10	254.09	28.94	180.81	121.65	
1971	325.40	1,431.12	296.52	281.15	29.69	195.51	137.14	
1972	327.35	1,449.29	296.96	310.64	30.51	211.74	153.86	
1973	329.91	1,462.86	297.40	343.56	31.41	230.16	172.26	
1974	330.76	1,476.14	297.86	379.95	32.40	250.57	192.56	
1975	330.83	1,491.74	298.33	416.91	33.51	271.30	213.24	
1976	331.54	1,509.11	298.81	453.19	34.60	292.30	233.00	
1977	333.35	1,527.68	299.32	489.38	35.78	314.19	251.99	
1978	335.01	1,546.89	299.85	524.85	37.12	336.51	270.00	
1979	336.60	1,566.16	300.39	557.73	38.90	357.76	286.49	
1980	338.70	1,584.94	300.97	588.51	40.76	377.49	302.18	
1981	340.06	1,602.65	301.56	621.21	42.65	397.68	319.42	
1982	340.64	1,618.73	302.19	652.90	44.48	418.45	335.14	
1983	342.27	1,632.62	302.84	685.20	46.14	437.87	352.51	
1984	344.01	1,643.50	303.53	715.67	47.82	458.80	366.80	
1985	345.46	1,655.91	304.25	753.45	49.69	486.19	383.27	
1986	346.90	1,668.79	305.00	789.53	51.62	508.22	402.41	
1987	348.77	1,683.75	305.79	831.33	53.55	535.08	423.35	
1988	351.28	1,693.94	306.62	879.94	55.70	564.26	449.32	
1989	352.89	1,705.63	307.83	921.47	57.93	593.68	468.07	
1990	354.07	1,717.40	308.68	953.43	60.21	616.35	482.76	
1991	355.35	1,729.33	309.23	979.87	62.66	636.82	493.78	
1992	356.23	1,740.14	309.73	1,001.60	65.13	650.21	505.87	
1993	356.92	1,743.10	310.10	1,012.33	67.79	657.53	511.99	
1994	358.25	1,748.62	310.81	1,021.09	70.74	662.45	518.21	
1995	360.24	1,755.23	311.28	1,029.02	74.60	666.66	524.66	
1996	362.00	1,757.19	312.30	1,038.98	79.14	673.40	531.41	
1997	363.25	1,761.50	313.18	1,041.17	84.42	674.97	534.96	
1998	365.93	1,770.29	313.91	1,046.23	90.45	681.59	537.67	
1999	367.84	1,778.20	314.71	1,048.71	96.94	685.59	540.14	
2000	369.12	1,778.01	315.76	1,051.12	104.52	690.46	542.38	
2001	370.67	1,776.53	316.49	1,052.91	113.35	697.10	543.20	
2002	372.83	1,778.96	317.10	1,053.74	121.44	702.52	543.66	
2003	375.41	1,783.59	317.73	1,053.52	129.89	707.84	543.35	
2004	376.99	1,784.23	318.36	1,053.30	139.31	713.98	542.85	
2005	378.91	1,783.36	319.13	1,053.46	150.43	721.88	542.15	
2006	381.01	1,783.42	319.93	1,053.71	160.64	730.31	540.65	
2007	382.60	1,788.95	320.65	1,053.94	171.15	739.81	538.43	
2008	384.74	1,798.42	321.57	1,054.80	181.99	750.11	536.33	
2009	386.28	1,802.10	322.28	1,054.17	191.13	758.10	533.78	
2010	388.72	1,807.85	323.14	1,054.37	203.07	768.76	531.28	
2011	390.94	1,813.07	324.16	1,053.45	216.23	779.12	528.53	
2012	393.02	1,815.26	325.00	1,051.97	227.84	787.77	525.83	
2013	395.72	1,822.58	325.92	1,051.74	244.88	801.30	523.11	
2014	397.55	1,831.47	326.99	1,049.51	257.06	809.19	520.58	

1127

1128   **Table 8 - Raw data used for CH$_4$ surface mixing ratio field derivation**

Dataset	Reference / URL	Stations / Location	Used for	Description / Filtering
NOAA ESRL GMD Surface Flask data.	(Steele et al. 1987, Lang 1990b, Lang 1990a, Steele 1991, Lang 1992, Steele et al. 1992, Dlugokencky et al. 1994a, Dlugokencky et al. 1994c, Dlugokencky et al. 1998, Dlugokencky et al. 2001, Dlugokencky et al. 2005, Dlugokencky et al. 2009, Dlugokencky 2015a)	87 stations of the surface flask network[a]: ABP, ALT, AMS, AMT, AOC, ASC, ASK, AVI, AZR, BAL, BHD, BKT, BME, BMW, BRW, BSC, CBA, CGO, CHR, CIB, CMO, CPT, CRZ, DRP, DSI, EIC, GMI, GOZ, HBA, HPB, HSU, HUN, ICE, ITN, IZO, KCO, KEY, KPA, KUM, KZD, KZM, LEF, LLB, LLN, LMP, MBC, MCM, MEX, MHD, MID, MKN, MLO, NAT, NMB, NWR, NZL, OPW, OXK, PAL, PAO, POC, PSA, PTA, RPB, SCS, SDZ, SEY, SGI, SGP, SHM, SIO, SMO, SPO, STM, SUM, SYO, TAP, THD, TIK, USH, UTA, UUM, WIS, WKT, WLG, WPC, ZEP	Observational period estimation of global mean, latitudinal gradient seasonality and seasonality change over 1984-2013. Optimization of global mean and latitudinal gradient in 2014 and before 1984.	This study used monthly station averages that include all sample points, which have a 'accepted' flag, i.e. initial two dots ('..*') in the three digit flag.
AGAGE GC-MD	(Prinn et al. 2000b)	AGAGE GC-MD network[b]: CGO, MHD, RPB, SMO, THD		The monthly station averages that include pollution events ('.mop' file endings in case of AGAGE) were used.
Law Dome	(Etheridge et al. 1998a, MacFarling Meure et al. 2006)	Law Dome ice core at -66.73-degree south.	Long-term high-latitude southern hemisphere reference point with piecewise 3rd-degree polynomial smoothing over years 155 to 1974.	
EPICA Dronning Maud Land Ice Core	(Barbante et al. 2006, Capron et al. 2010)	Dronning Maud Land Ice Core	Used as input for piecewise 3rd-degree polynomial smoothing over remainder of years 0 to 153.	
NEEM Greenland	(Dahl-Jensen et al. 2013, Rhodes et al. 2013)	NEEM ice core Greenland data	Used for optimisation of global mean and latitudinal gradient score of EOF1 over timescale from year 0 to 1984, with linear interpolation of score 1 in between available NEEM datapoints. (section 2.1.4)	

1129   [a] NOAA station descriptions here: http://www.esrl.noaa.gov/gmd/dv/site/site_table.html

1130   [b] AGAGE station descriptions here: https://agage.mit.edu/global-network

1131

1132   **Table 9 - Raw data used for N$_2$O surface mixing ratio field derivation**

Dataset	Reference / URL	Stations / Location	Used for	Description / Filtering
NOAA ESRL GMD Surface Flask data.	Combined N$_2$O data from the NOAA/ESRL Global Monitoring Division, (ftp://ftp.cmdl.noaa.gov/hats/n2o/combined/HATS_global_N2O.txt, file date: Wed, Aug 19, 2015 2:40:55 PM)	13 stations of the NOAA HATS global[a]: alt, brw, cgo, kum, mhd, mlo, nwr, psa, smo, spo, sum, tdf, thd	Observational period estimation of global mean, latitudinal gradient seasonality and seasonality change over 1990-2013. Optimization of global mean and latitudinal gradient in 2014.	This study uses station averages, which include all sample points, which have an 'accepted' flag, i.e. initial two dots ('..*') in the three digit flag. ('.mop' file endings in case of AGAGE)
AGAGE GC-MD	(Prinn et al. 1990, Prinn et al. 2000b)	AGAGE GC-MD network[b]: CGO, MHD, RPB, SMO, THD		
Law Dome	(MacFarling Meure et al. 2006)	Law Dome ice core at -66.73 degree south.	Long-term high-latitude southern hemisphere reference point with piecewise 3rd-degree polynomial smoothing over years 155 to 1974.	
NEEM Greenland	(Dahl-Jensen et al. 2013, Rhodes et al. 2013)	NEEM firn Greenland data	Used for comparison only as latitudinal gradient estimated as very small and constant and assumed constant before observational period	
Gap			At this stage, sparse data availability in the period 1968 to 1986 suggests against optimisations of global-means with annual datapoints, which is why an interpolation between 1968 (starting from smoothed Law Dome record) to 1986 (ending with optimized global mean to fit observational data) is assumed.	

1133   [a] NOAA station descriptions here: http://www.esrl.noaa.gov/gmd/dv/site/site_table.html

1134   [b] AGAGE station descriptions here: https://agage.mit.edu/global-network

1135

Table 10- Options for reducing the number of GHGs to be taken into account to approximate full radiative forcing of all GHGs. In Option 1, a climate model explicitly resolves actual GHG mixing ratios. With 8 and 15 species, 99.1% and 99.7% of the total radiative effect can be captured. In Option 2, only CFC-12 is modelled next to CO₂, CH₄, and N₂O; all other gases are summarized in a CFC-11-equivalence mixing ratio. In Option 2, all ODS are summarized in a CFC-12-equivalence mixing ratio, and all other fluorinated substances are summarized in HFC-134a-equivalence mixing ratios. The first column indicates the importance of gases in terms of the radiative effect change between 1750 and 2014. Note that below shares are approximations, as linear radiative forcing efficiencies are assumed here for all gases, also for CO₂, N₂O and CH₄.

Rank	The GHG contribution to climate change since 1750. Shares of change of total warming effect since 1750: Approx. Radiative forcing contribution between 1750 and 2014 relative to that of all GHGs		Option 1 Using subset of actual mixing ratios, no equivalent gases Shares of total warming effect: Approx. Radiative effect compared to effect of all GHGs (absolute in 2014, not relative to 1850)		Option 2 Summarizing all gases of lower importance than CFC-12 into CFC-11eq.		Option 3 Summarizing all ODS into CFC-12-eq and all other fluorinated gases into HFC134a-eq	
1	CO_2	64.0%	CO_2	72.9%	CO_2	72.9%	CO_2	72.9%
2	CH_4	79.5%	N_2O	86.1%	N_2O	86.1%	N_2O	86.1%
3	CFC12	86.0%	CH_4	95.0%	CH_4	95.0%	CH_4	95.0%
4	N_2O	92.2%	CFC12	97.2%	CFC12	97.2%	CFC12-eq	99.5%
5	CFC11	94.5%	CFC11	98.0%	CFC11-eq	100.0%	HFC134a-eq	100%
6	HCFC22	96.4%	HCFC22	98.6%				
7	CFC113	97.2%	CFC113	98.9%				
8	CCl4	97.8%	CCl4	99.1%				
9	HFC134a	98.3%	HFC134a	99.3%				
10	CFC114	98.5%	CF4	99.4%				
11	HFC23	98.7%	CH3Cl	99.5%				
12	SF6	98.8%	CFC114	99.5%				
13	CF4	99.0%	HFC23	99.6%				
14	HCFC142b	99.2%	SF6	99.7%				
15	HCFC141b	99.3%	HCFC142b	99.7%				
...	28 more GHGs	100%	28 more GHGs	100%				

1143

1144

1145

Table 11 – Exponents 's' to estimate vertical gradient of mixing ratios for gases with stratospheric sinks in the stratospheric column – depending on the latitude 'lat'. See text. For HFC-134a and other species with stratospheric lifetimes shorter than 30 years, the CH_4 exponent parameterization can be used as approximation. This exponent scale parameterization is taken from the CESM model, implemented by J. Kiehl.

	TROPICS AND MID-LATITUDES ABS(LAT)<45°	MID TO HIGH LATITUDES, ABS(LAT)≥45°
CH_4	0.2353	0.2353 + 0.0225489 * (abs(lat) - 45);
N_2O	0.3478 + 0.00116 * abs(lat)	0.40 + 0.013333 * (abs(lat) - 45)
CFC-11	0.7273 + 0.00606 * abs(lat)	1.00 + 0.013333 * (abs(lat) - 45);
CFC-12	0.4000 + 0.00222 * abs(lat)	0.50 + 0.024444 * (abs(lat) - 45)

1150

1151

1152

1153

1154

1155

1156 **12 Figures**

1157 *Note: all mixing ratios (ppmv, ppbv, pptv) are mole mixing ratios and should be read as 9ppmvv, ppbv and pptv,*
1158 *respectively).*
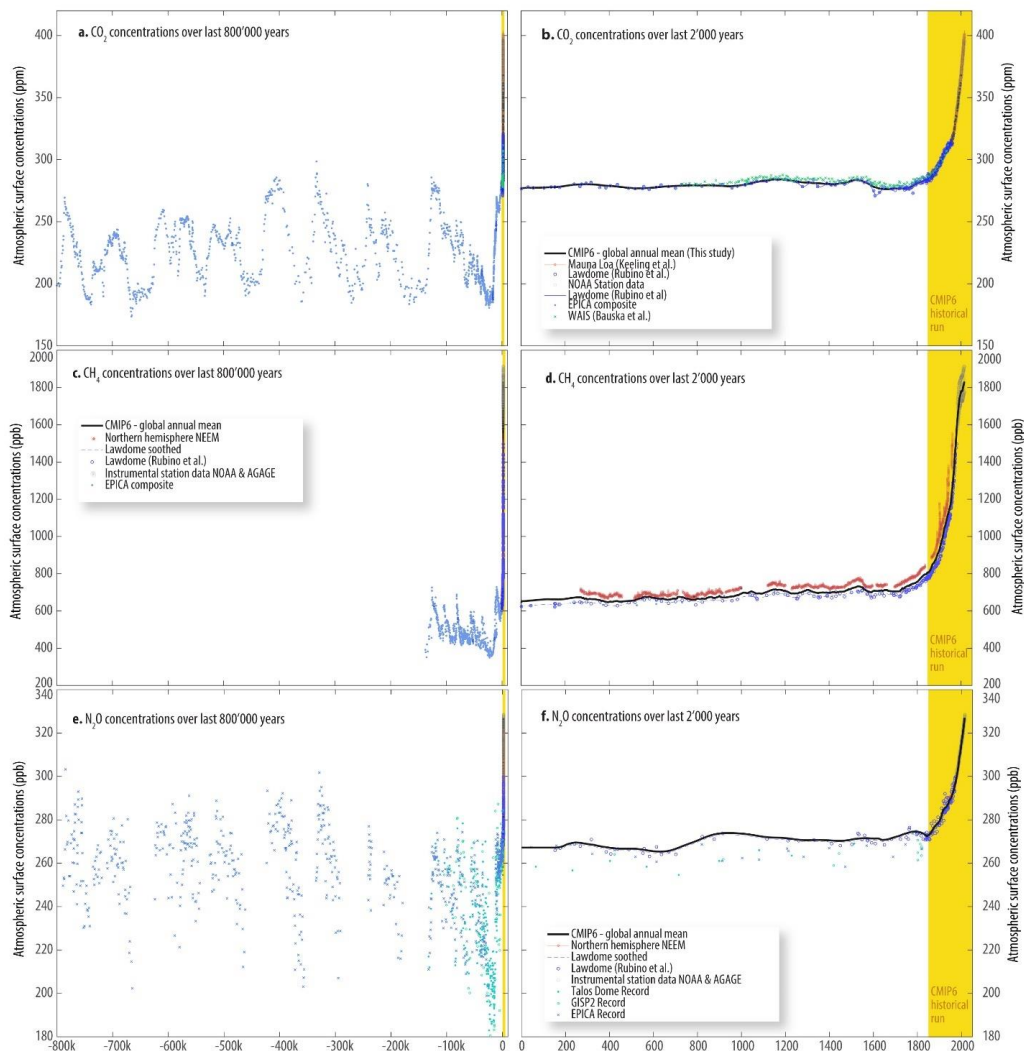
1159

Figure 1 - Atmospheric CO₂, CH₄ and N₂O mixing ratios over different time-scales, from 800 thousand years ago until today (panel a, c, e), from Year 0 A.D. to today (panel b, d, f). The shown data is for CO₂: Mauna Loa data by Keeling et al. (Keeling et al. 1976); the Law Dome ice record (Etheridge et al. 1998c, MacFarling Meure et al. 2006, Rubino et al. 2013); NOAA ESRL station data (NOAA 2013, NOAA ESRL GMD 2014c, NOAA ESRL GMD 2014b, NOAA ESRL GMD 2014a); the EPICA composite data (Lüthi et al. 2008, Bereiter et al. 2015) and the WAIS data (Bauska et al. 2015). For CH₄, the shown data is the Law Dome data (Etheridge et al. 1998b, MacFarling Meure et al. 2006), the instrumental data from the NOAA and AGAGE networks (see Table 8), NEEM ice core measurements (Rhodes et al. 2013) and the EPICA composite (Barbante et al. 2006)   In case of N₂O, the shown data is the Law Dome record (MacFarling Meure et al. 2006), the Talos Dome record (Schilt et al. 2010b), the GISPII record (Sowers et al. 2003) and the EPICA record (Fluckiger et al. 2002, Spahni et al. 2005, Schilt et al. 2010a) [The figure will be updated to reflect references in legend and to include CH₄ data over the last 800,000 years based on data by Loulergue (2008)].

1170

1171
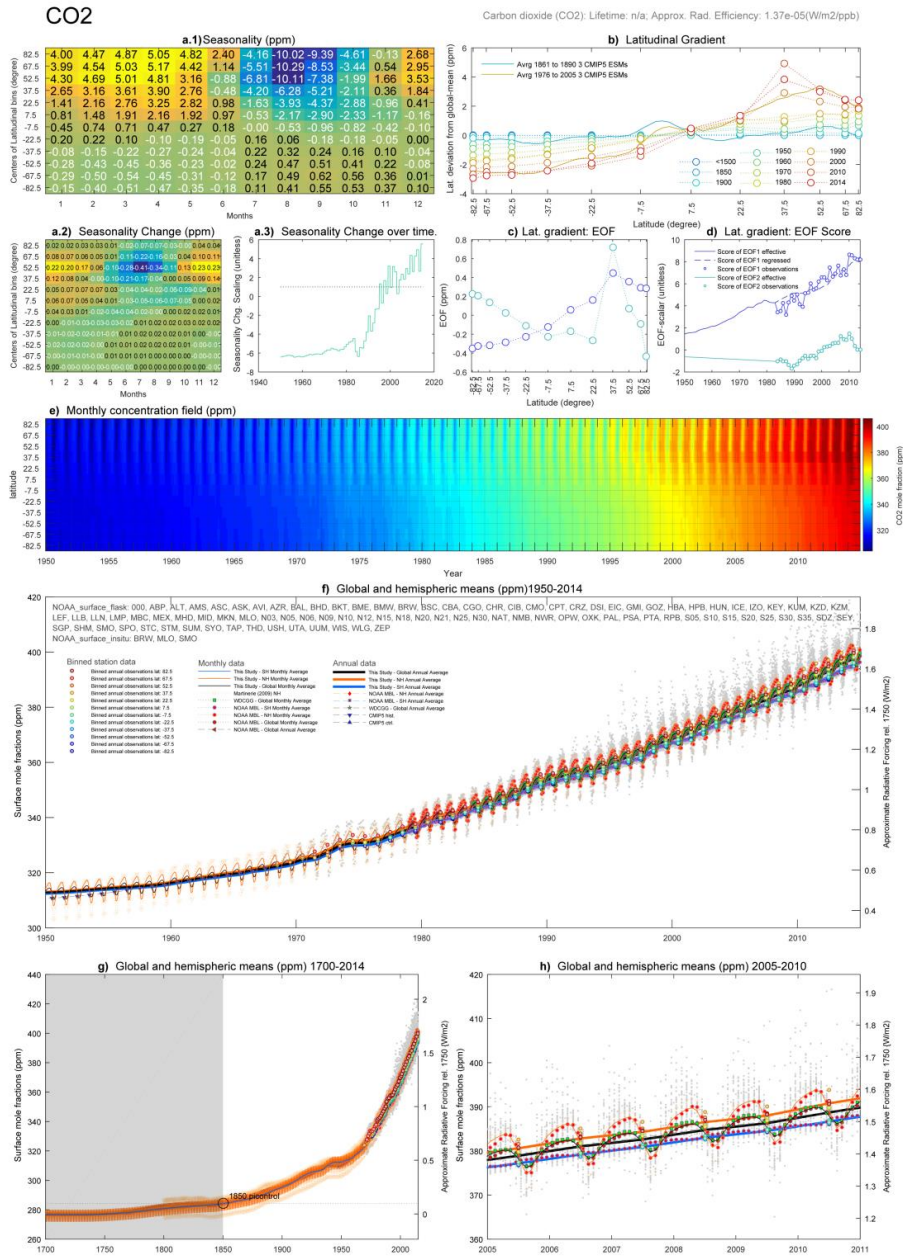
1172

Figure 2 - Overview of historical CO₂ mixing ratios. Panel a.1, the average seasonality of CO₂ over the observational period, a.2, the change of seasonality over time. a.3, the observationally derived and extended EOF score of the seasonality change. The first EOF1's score is almost linearly increasing over the time of instrumental data from 1984 to 2014. b, the latitudinal variation of mixing ratios (dashed lines), shown for example years from 1500 to 2014, including (for comparison) the average of three CMIP5 ESM models (solid lines). c, the first and second EOF of latitudinal variation. The second EOF exhibits a strong signal around middle northern latitudes d, the EOF scores derived from the observational data (dots) and regression (dashed line) as well as the ultimately used EOF score (solid line). The second EOF's score indicates that the mid-latitude northern spike was only a recent phenomenon and

1180 the score is here assumed to linearly converge to zero. The first EOF's score is more linearly increasing, and regressed against global
1181 fossil emissions. e, the resulting latitudinal-monthly mixing ratio field, here shown between 1950 and 2014. f, global and hemispheric
1182 means of the derived mixing ratio field over the same time period 1950 to 2014 in comparison to monthly station data (grey dots),
1183 latitudinal average station data (colored circles), and various literature studies (see legend). g, same as panel f, except for time period
1184 1750 to 2014. h, same as panel f but for time period 2005 to 2010.

1185

1186

1187

1188
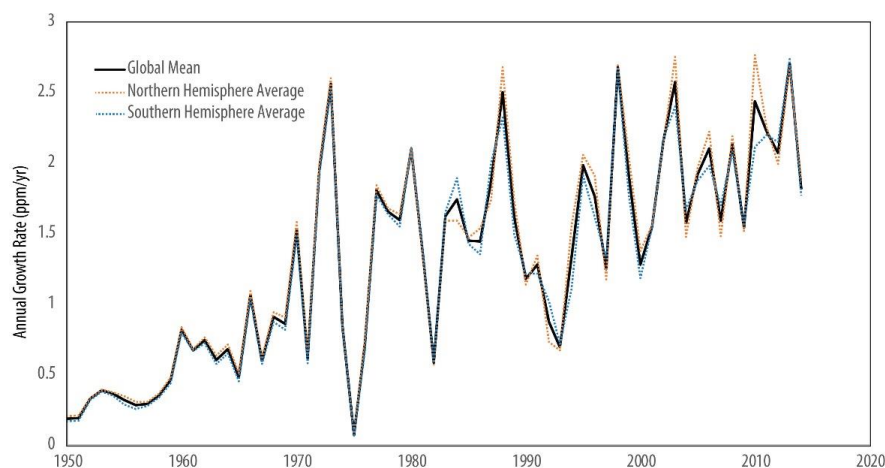
1189

1190 Figure 3 - Annual Growth Rate of CO_2 mixing ratios for global-mean, northern hemispheric average and southern hemispheric
1191 average mixing ratios. Before 1960, the smooth growth rate results from interpolated global mean values. After 1960, the growth
1192 rates are diagnosed from the surface station data, as shown in Figure 2f. Noticeable are fluctuations of the annual growth rate around
1193 1973, 1981, and 1992.
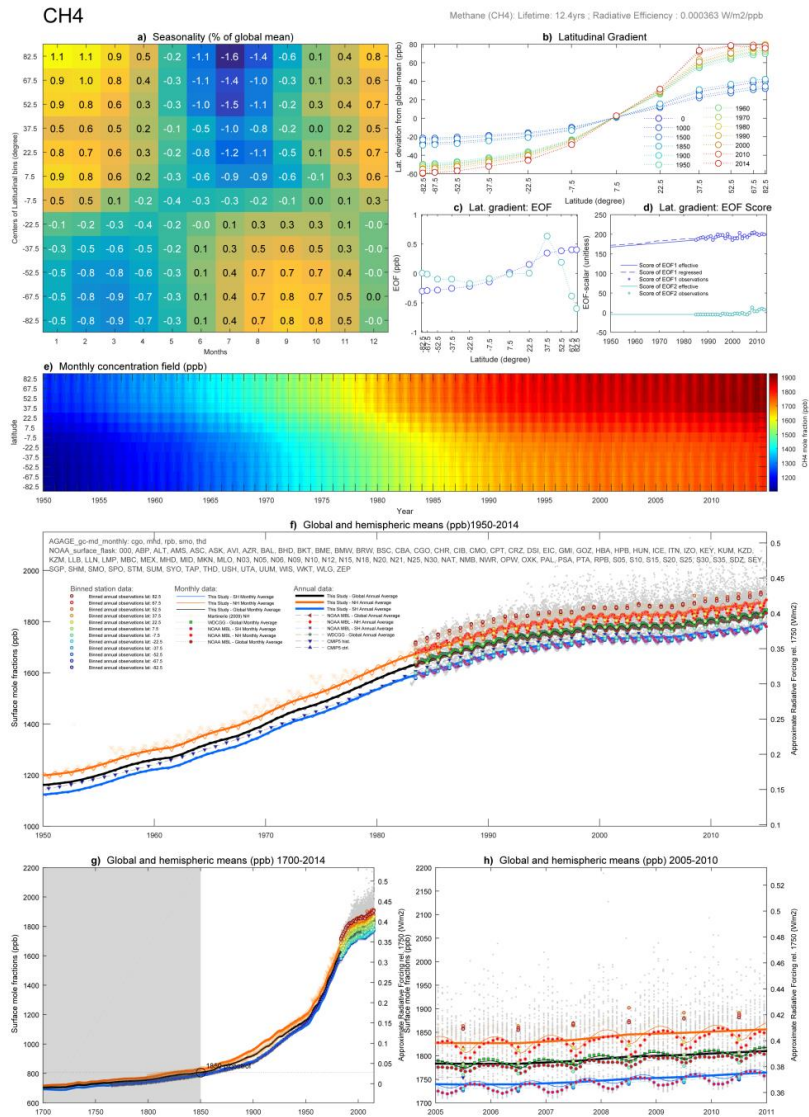
1194

Figure 4 - Overview of historical CH₄ mixing ratios. Panel a.1**, the relative seasonality of CH₄ over the observational period.** b**, the latitudinal variation of mixing ratios (dashed lines), shown for example years.** c**, the first and second EOF of latitudinal variation.** d**, the EOF scores derived from the observational data (dots) and regression against global emissions (dashed line) as well as the ultimately used EOF score (solid line).** e**, the resulting latitudinal-monthly mixing ratio field, here shown between 1950 and 2014.** f**, global and hemispheric means of the derived mixing ratio field over the same time period 1950 to 2014 in comparison to monthly station data (grey dots), latitudinal average station data (colored circles), and various literature studies (see legend).** g**, same as panel f, except for time period 1750 to 2014.** h**, same as panel f but for time period 2005 to 2010.**
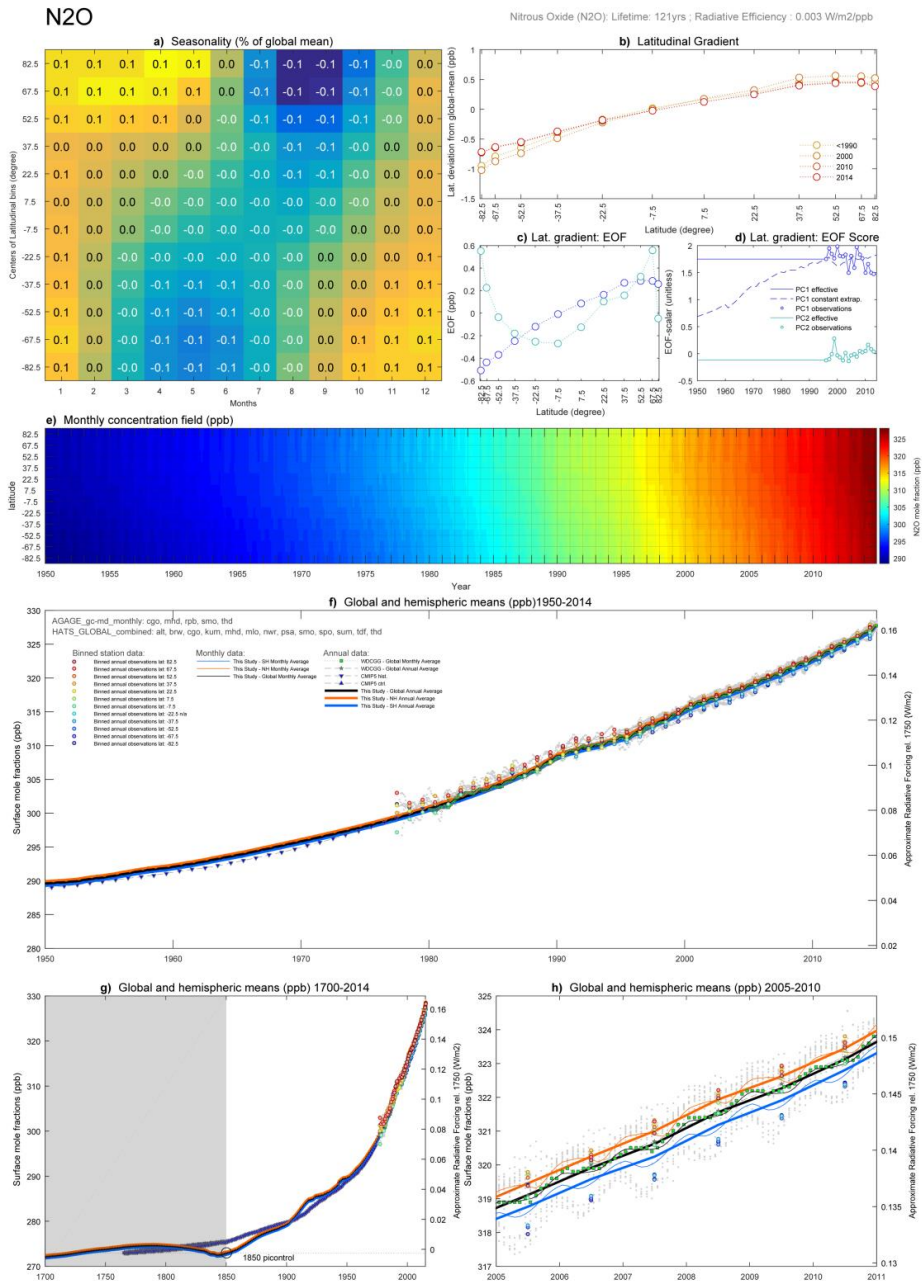
1202

Figure 5 - Overview over historical N₂O mixing ratios. As Figure 4, but for N₂O.
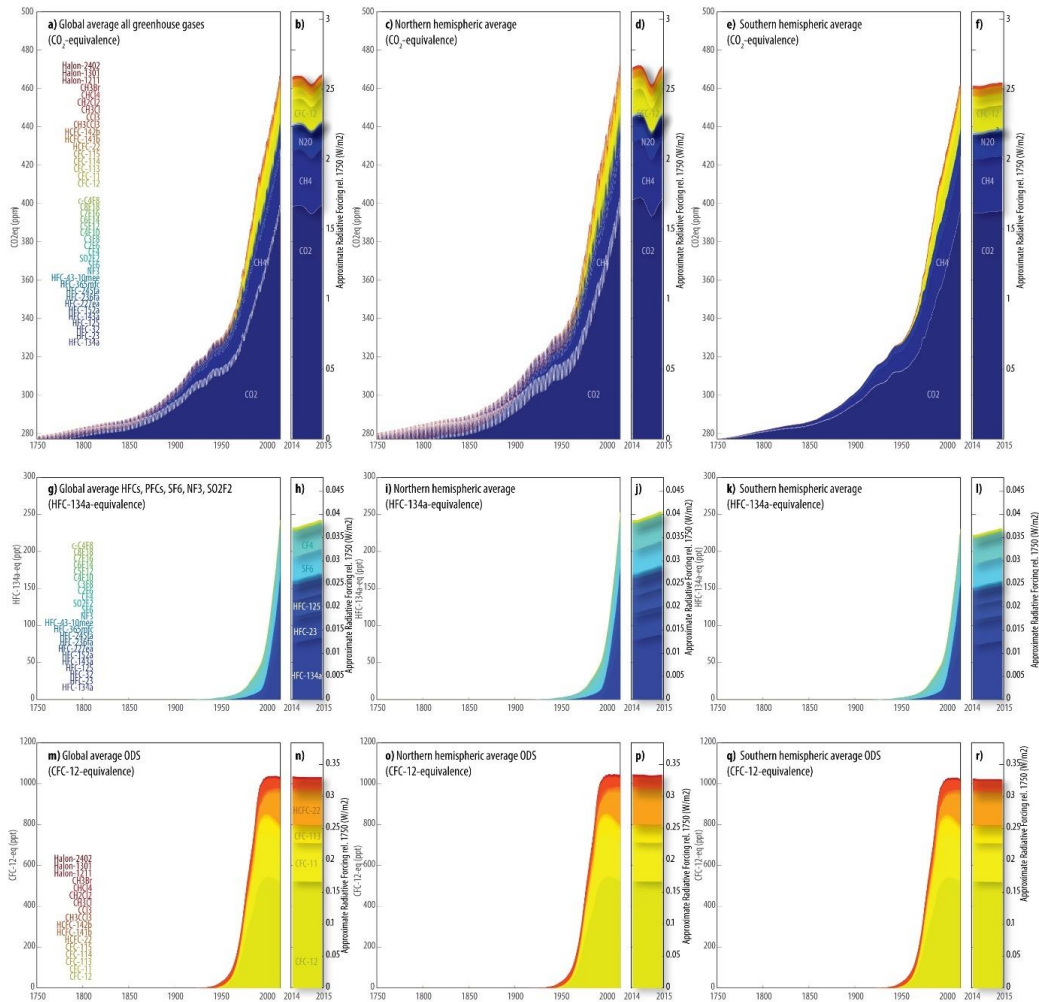
1204

Figure 6 – Historical GHG mixing ratios from 1750 to 2014 as global-mean average (right panels) northern hemispheric average (middle panels) and southern hemispheric averages (right panels). The top row comprises all greenhouse gases, the middle row comprises HFCs, PFCs, SF6, NF3 and SO2F2. The lower row comprises all ozone depleting substances, expressed as equivalent CFC-12eq mixing ratios. In the narrow boxes, the last data year from 15 Jan 2014 to 15 Dec 2015 is shown, indicating the intra-annual trend (top row), increasing gradient (middle row) or relatively flat mixing ratio levels (lower row). [NOTE, the lower two rows of this figure need a slight update in regard to their left hand axes, as equivalent mixing ratios are positive due to some gases with natural background mixing ratios].

1212
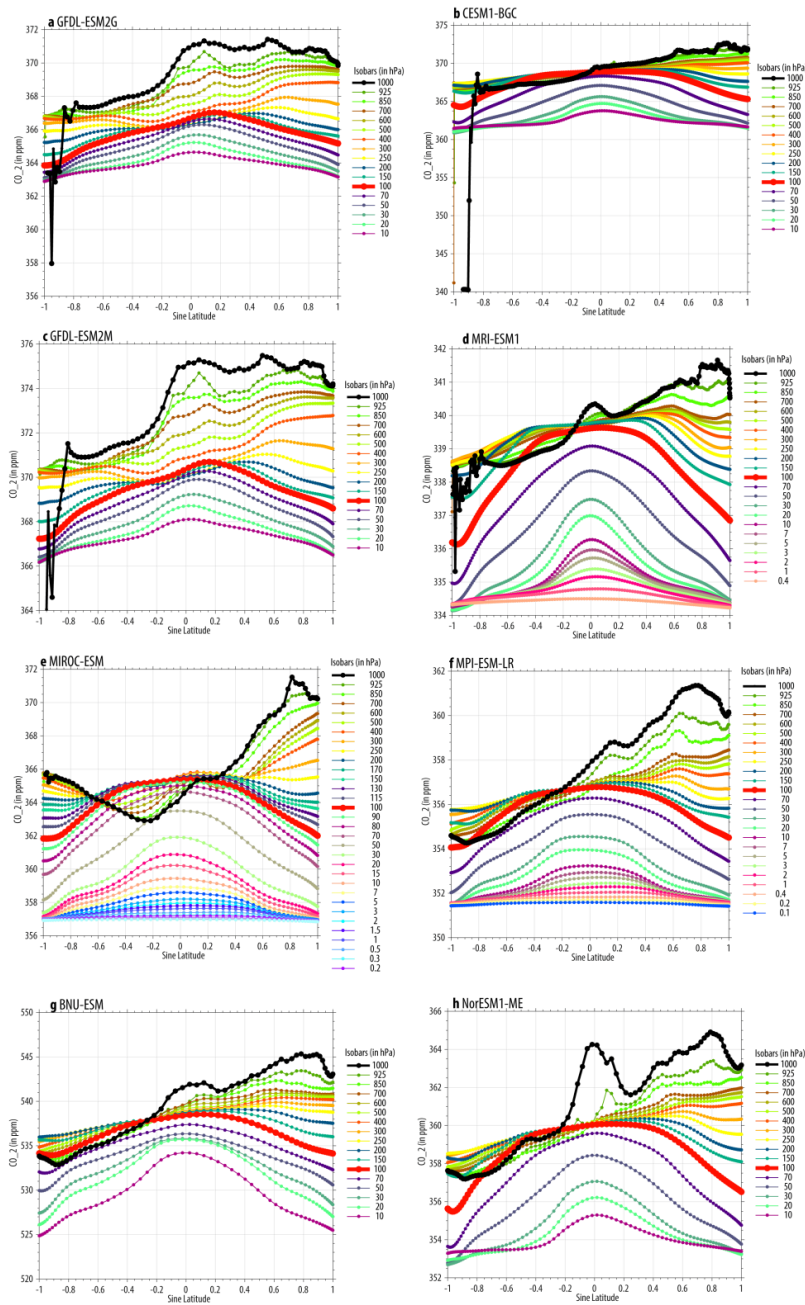
1213

Figure 7 - CMIP5 ESM models vertical mixing ratio averages at the provided pressure levels - as average over the 30-year period 1976 to 2005. The black line indicates surface mixing ratios at the 1000hPa pressure level. The red bold line indicates mixing ratios at the 100hPa level (cf. Figure 8a, and b).

1217
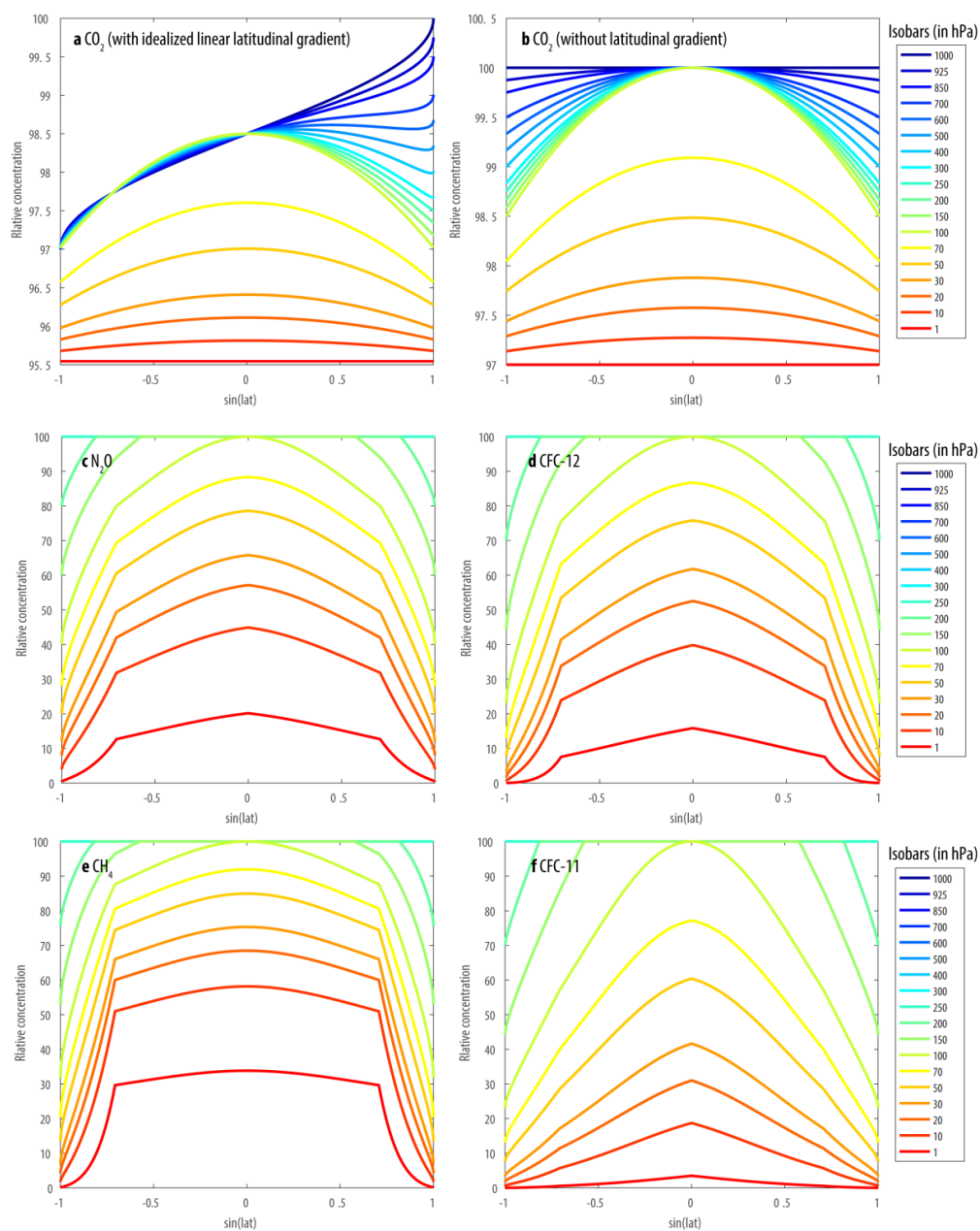
1218

Figure 8 – Idealized vertical gradients recommended for implementation of surface mixing ratio fields. For parametric formulas, see text. Note that tropospheric columns of non-CO$_2$ gases are – for simplicity – assumed to be well-mixed. The assumed age of air at the 1haPa level for CO$_2$ is 5 years.

1219
1220
1221

1222
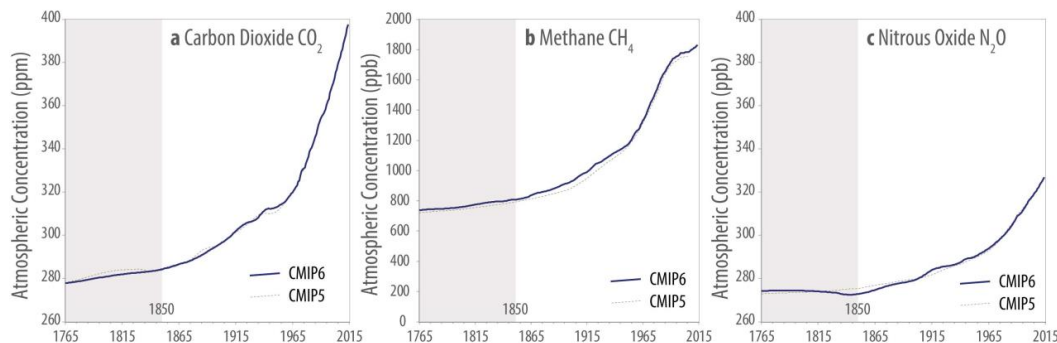
1223 **Figure 9 - Comparison between the recommendations for annual global mean surface mixing ratios of CO_2, CH_4 and N_2O between**
1224 **CMIP5 and CMIP6 for the historical experiment.**
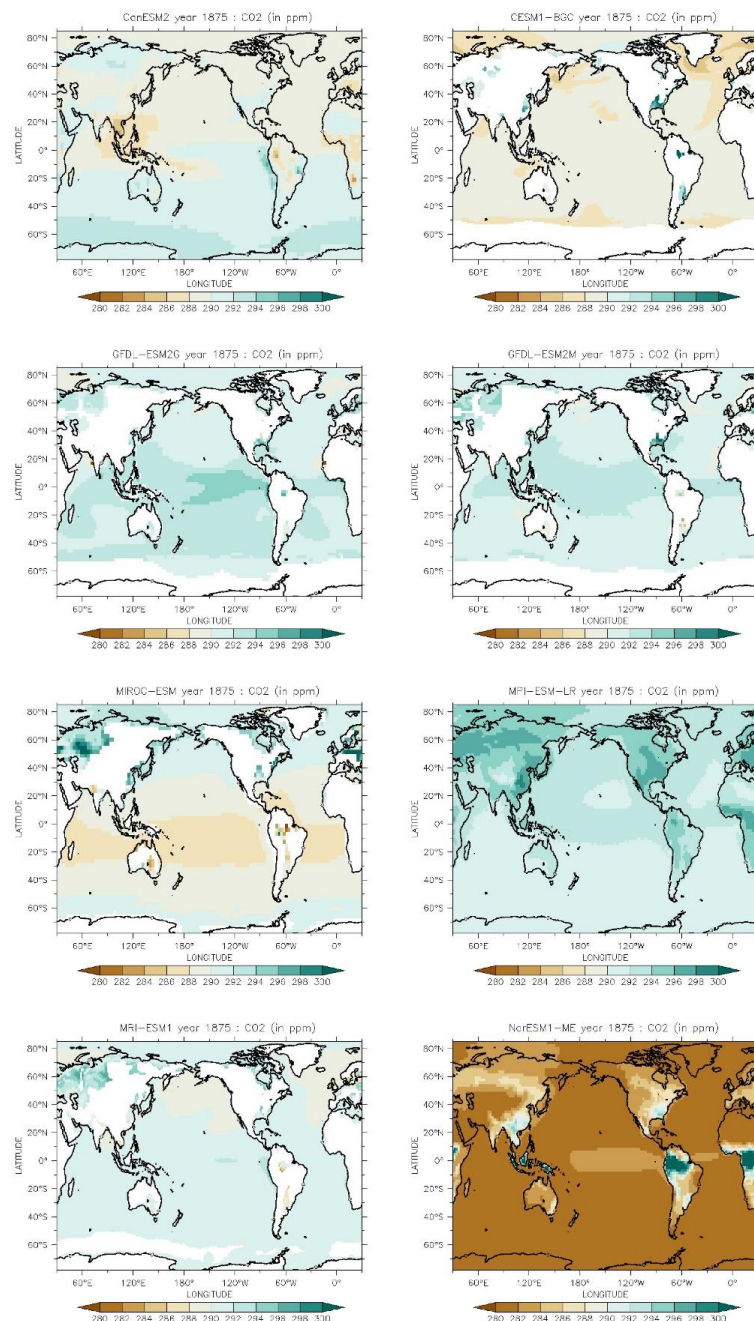
1225

Figure 10 - Annual mean CO_2 mixing ratios in 8 CMIP5 ESM models in the year 1875. The CMIP5 recommended value was 288.7 ppmv for 1875. Two more models with higher average CO_2 mixing ratios, namely BNU-ESM and FIO-ESM, are shown in Figure 63 and Figure 64.
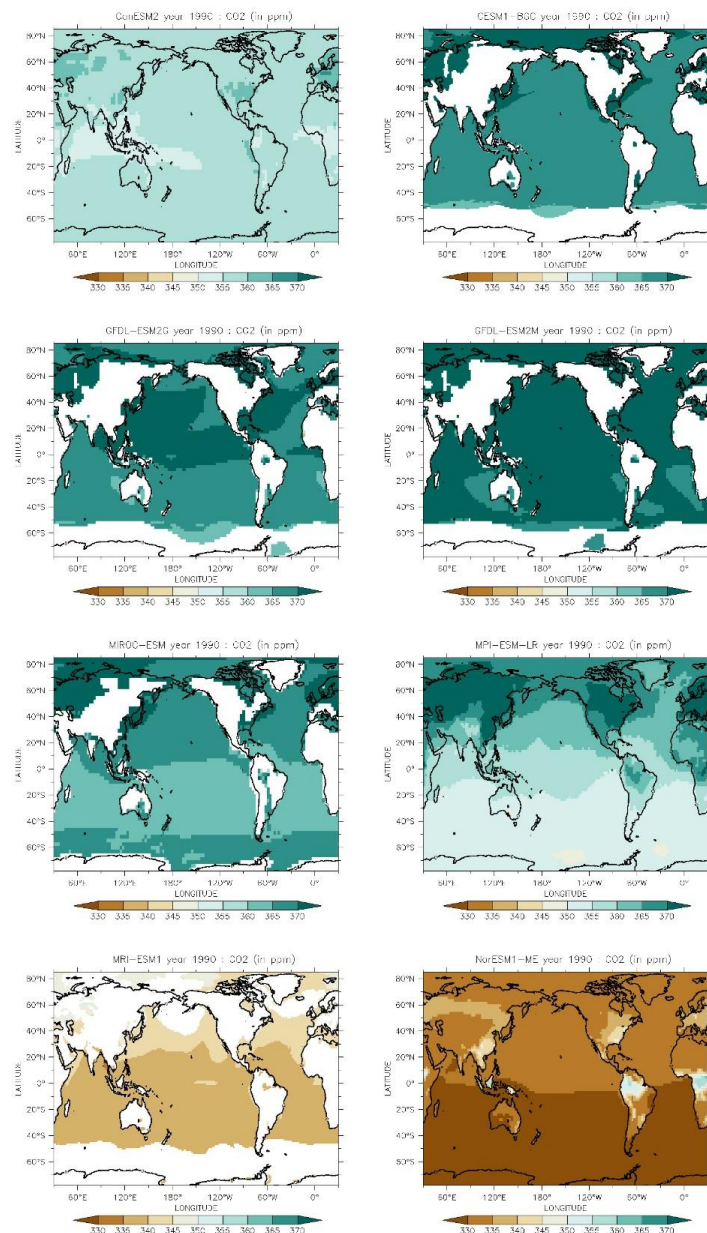
1229

Figure 11 - Annual mean CO$_2$ mixing ratios in 8 CMIP5 ESM models in the year 1990. The CMIP5 recommended value was 353.885 ppmv for 1990 in the historical experiment.

1230
1231

1232
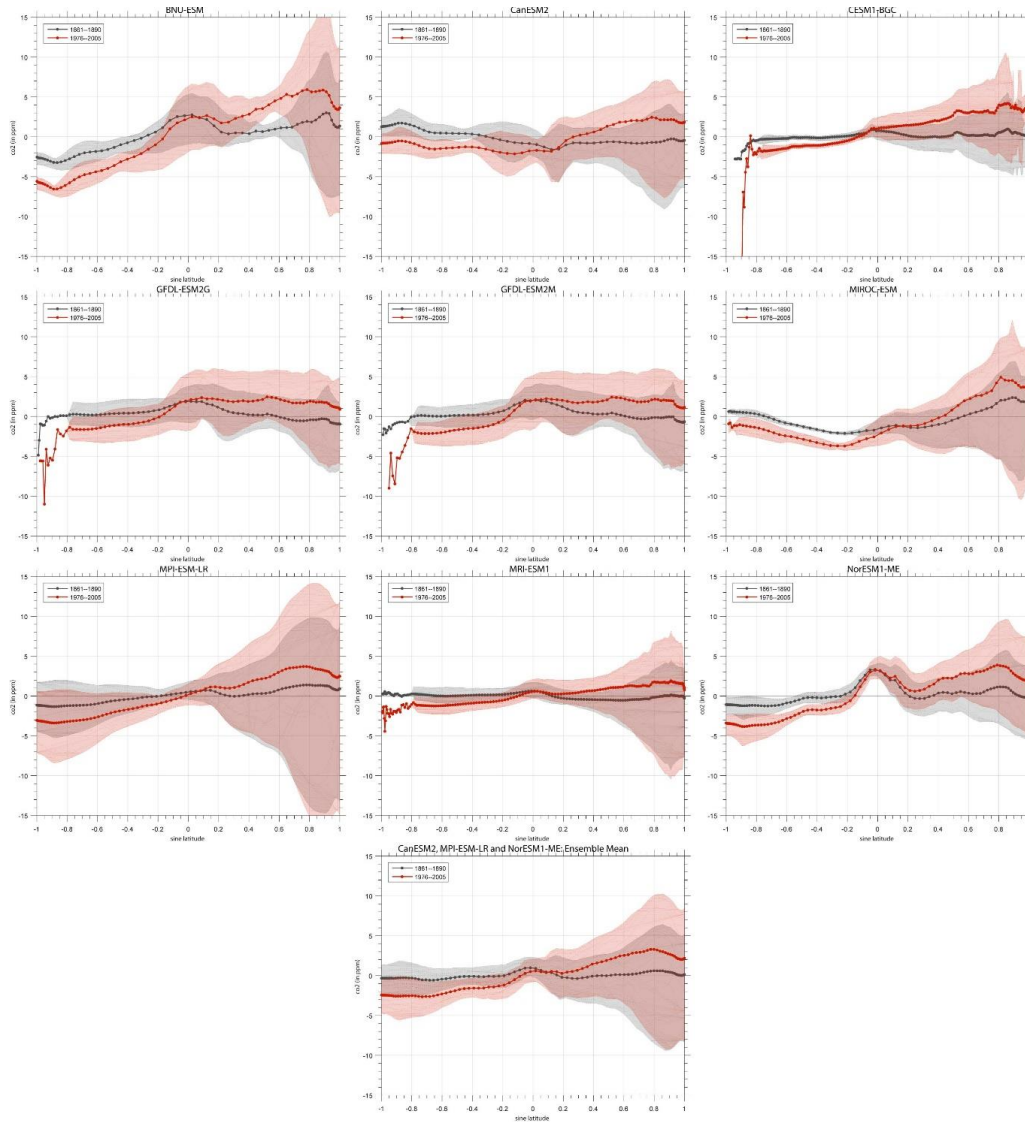
1233

Figure 12 - Latitudinal gradient of surface atmospheric CO₂ mixing ratios exhibited in 9 considered CMIP5 ESM models for both the preindustrial period (grey lines) and recent period 1976-2005 (red lines). The bold dotted lines indicate the annual means. The 12 finer lines represent the individual 12 monthly averages over the respective 30 year periods. The lowest panel shows an ensemble mean for three CMIP5 ESMs, namely CanESM2, MPI-ESM-LR and NorESM1-ME.

1238
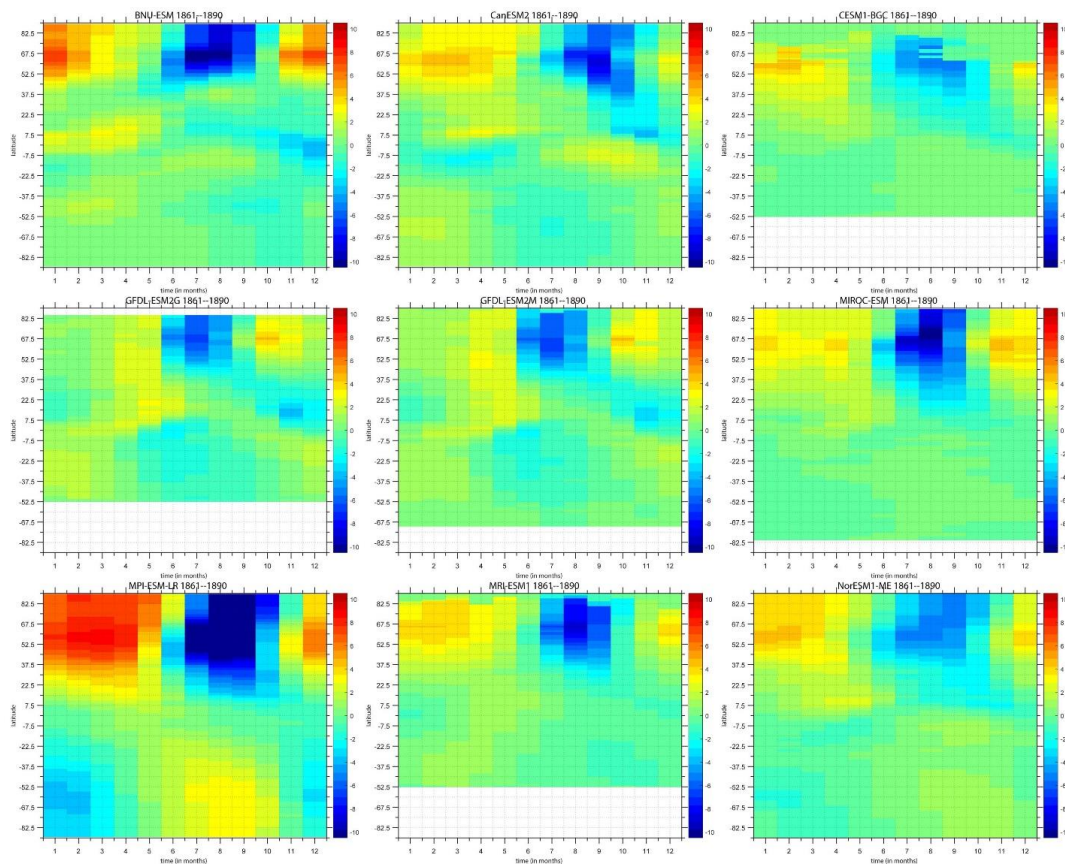
1239

Figure 13 – Climatological seasonal cycle of CO₂ mixing ratios in 9 CMIP5 ESM models for the historical experiment's 30-year period 1861-1890.
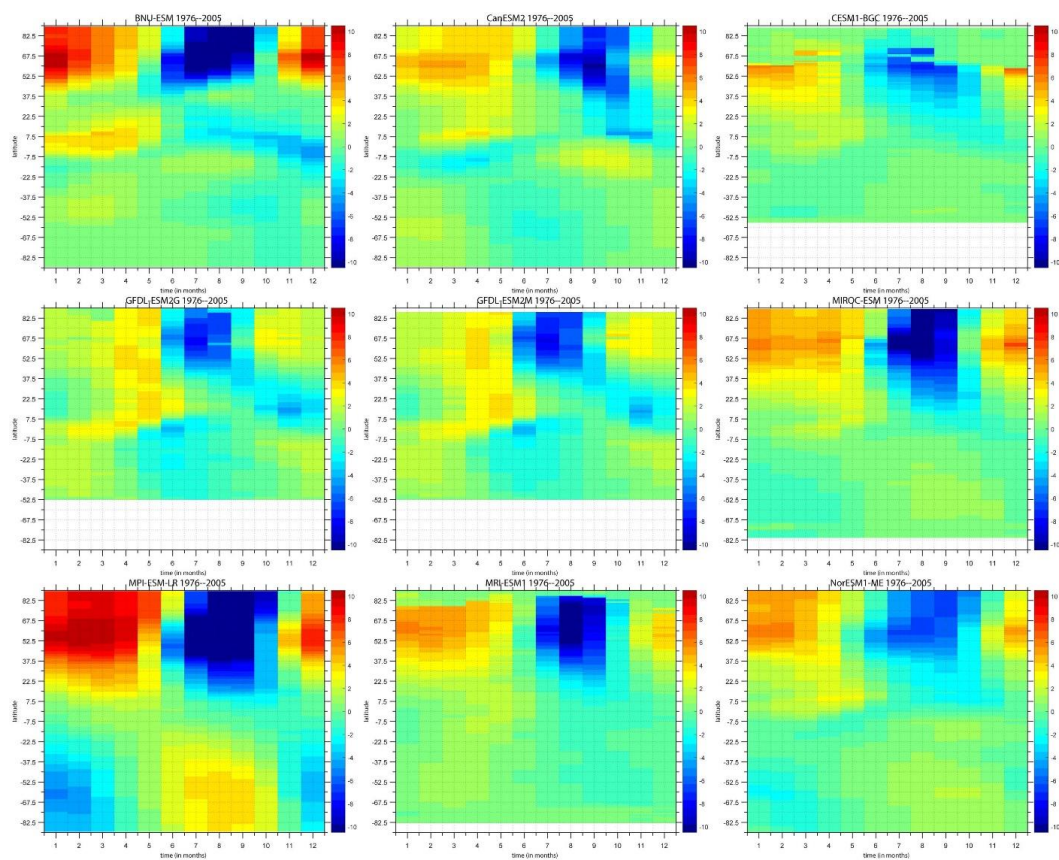
1242

Figure 14 – Climatological seasonal cycle of CO₂ mixing ratios in 9 CMIP5 ESM models for the historical experiment's 30-year period 1976-2005.

1243
1244

1245
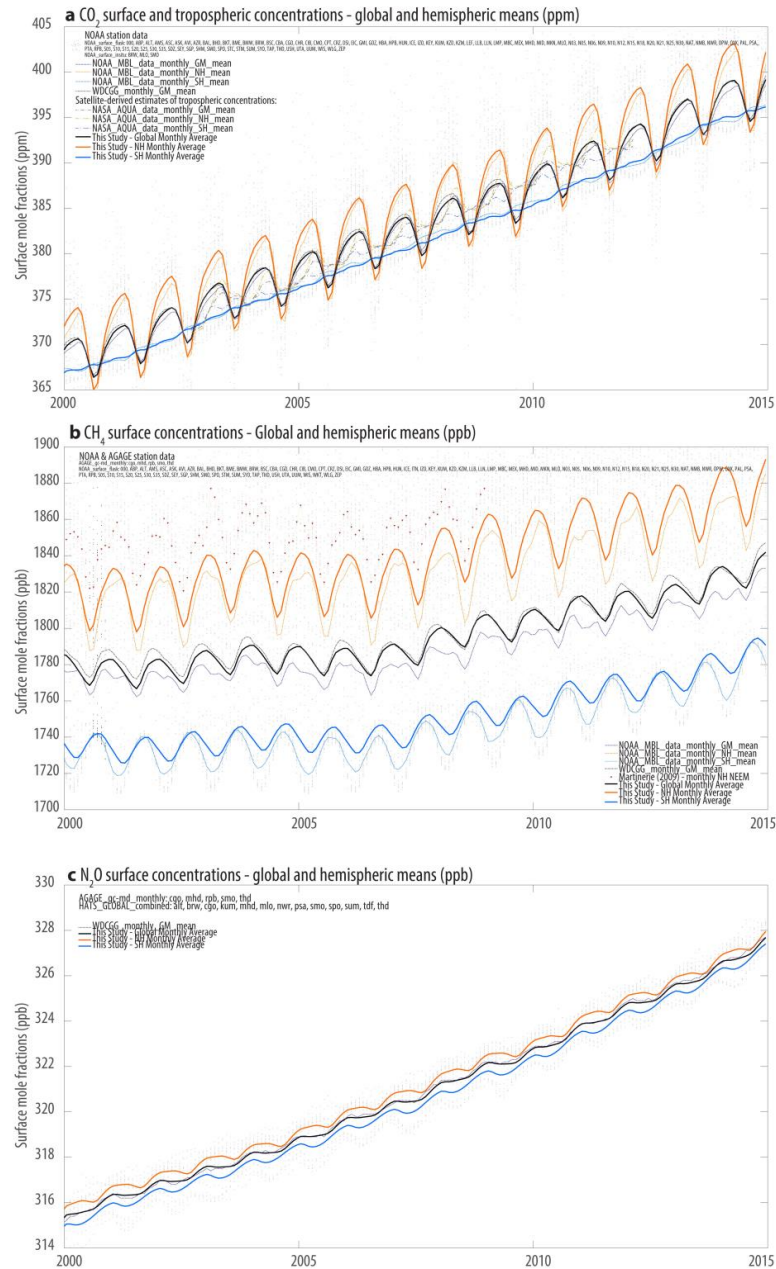
1246

Figure 15 - Comparison of global-mean, and hemispheric monthly average mixing ratios of CO₂ (panel a), CH₄ (panel b) and N₂O (panel c) between the CMIP6 surface mole fractions (this study), the NOAA Marine Layer Boundary products, the World Data Centre of Greenhouse gases (WDCGG) products and the NASA AQUA satellite data of tropospheric CO₂ mixing ratios. For comparison, individual (monthly average) NOAA and AGAGE station data across all latitudes is shown in the background (grey dots).

1252
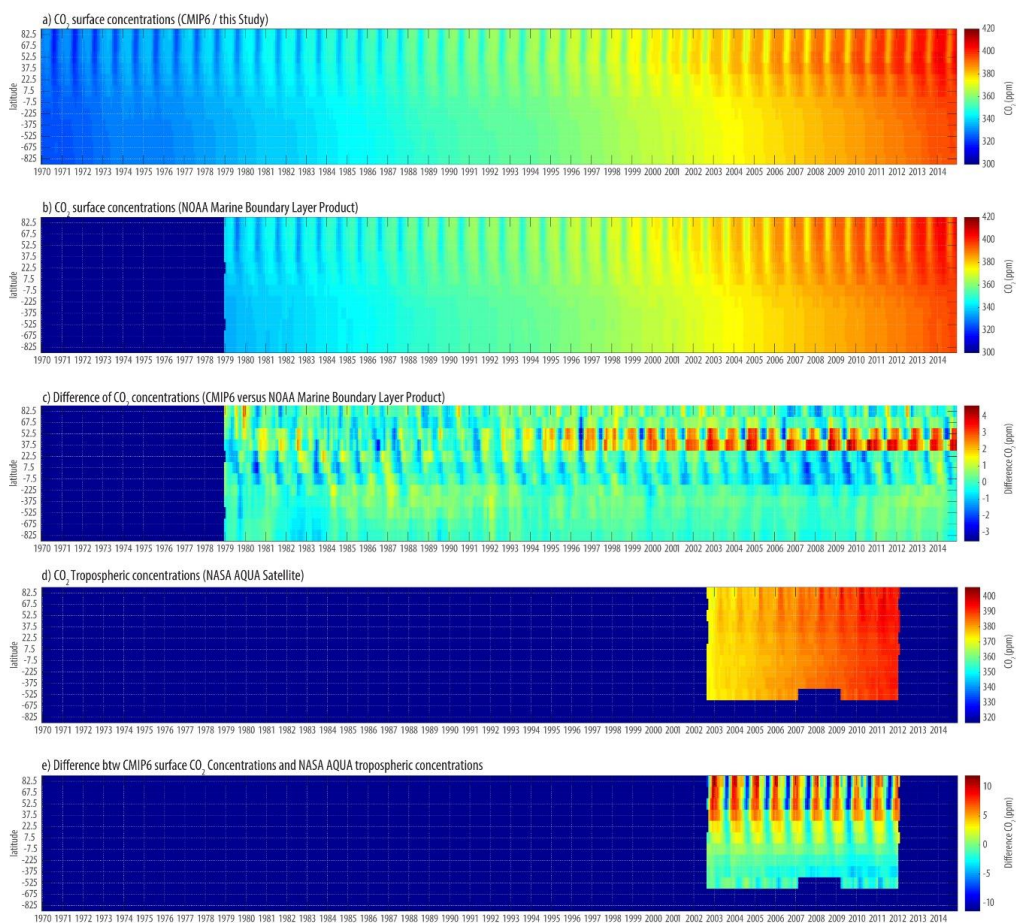
1253

1254   **Figure 16 - Comparison of the CMIP6 historical CO_2 emissions (panel a) with the NOAA Marine Boundary Layer MBL product**
1255   **from 1979 to 2014 (panel b). Differences indicate that a seasonal higher CO_2 mixing ratio is implied by the CMIP6 data of up to 5**
1256   **ppmv in mid-latitude northern bands, whereas some monthly tropical CO_2 mixing ratios tend to be slightly lower in the CMIP6**
1257   **product compared to NOAA MBL (panel c).**

1258
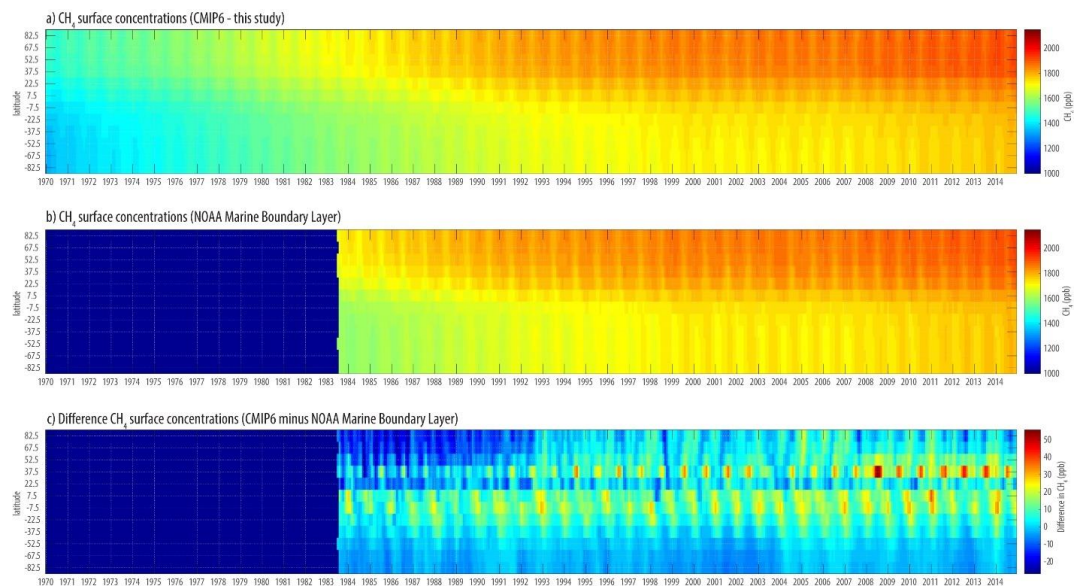
1259

1260 **Figure 17 - Comparison of the surface CH4 monthly mean mixing ratios between CMIP6 (panel a), the NOAA Marine Boundary**
1261 **Layer product (panel b) and the difference (panel c). Since around 1992, there are seasonal differences in the mid northern latitudes**
1262 **with the CMIP6 data being up to 50ppb higher than the NOAA MBL product. Similarly, higher mixing ratios are apparent in the**
1263 **areas of tropical southern and lower latitude southern areas, presumably due to differences of data over land areas.**

1264
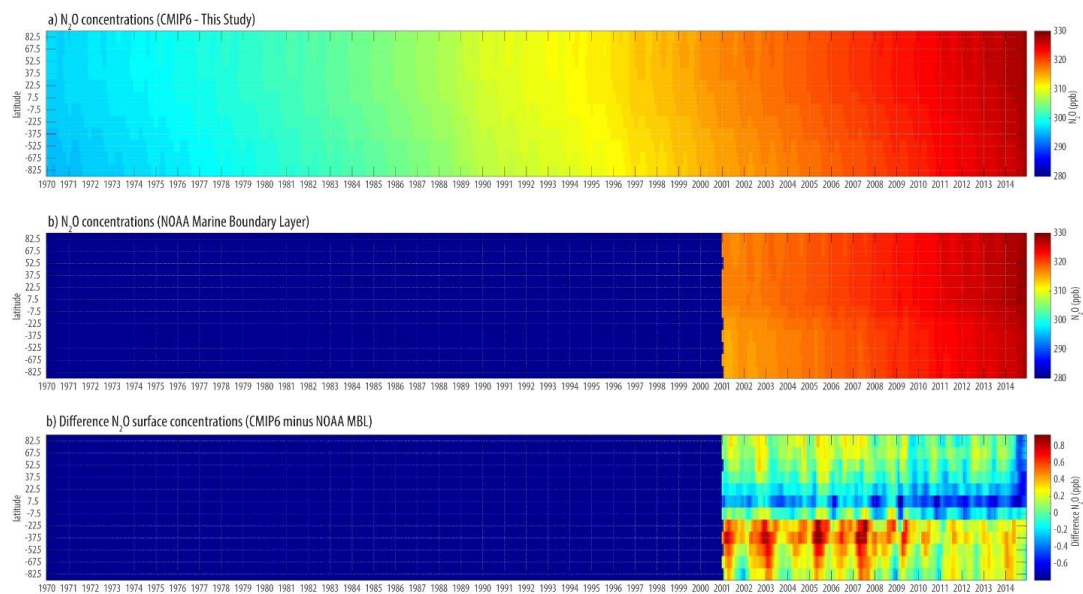
1265

Figure 18 - The comparison between latitudinal and monthly N₂O mixing ratios to the NOAA Marine Boundary Layer product (panel b). The differences (panel c) show that the CMIP6 historical GHG mixing ratios are slightly higher in the southern hemisphere (-0.5ppb) and slightly lower in the tropics (-0.5ppb), as the stronger latitudinal gradient from tropics to southern latitudes is not reproduces in CMIP6 data. Note: Data submitted by Pieter Tans, pers. Communication.

1270
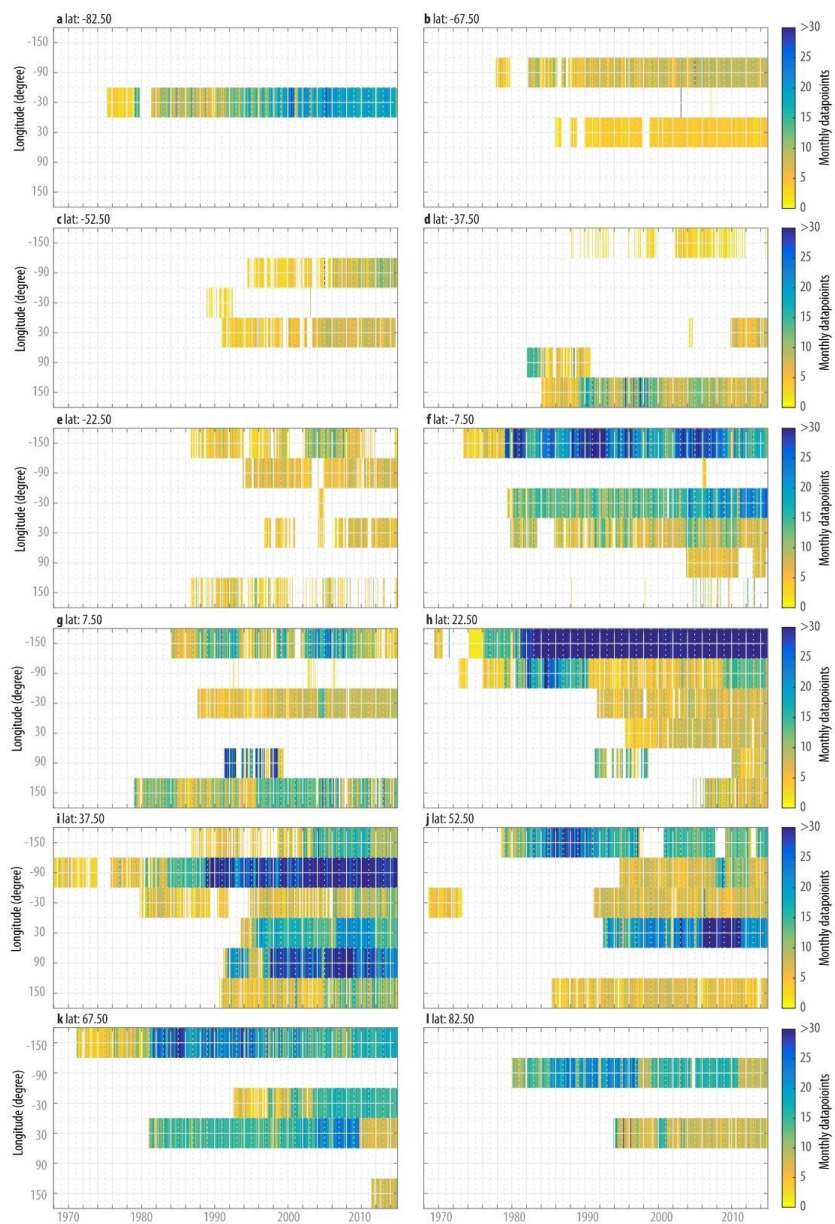
1271

1272 **Figure 19 - Availability of instrumental carbon dioxide data from 1968 to 2015 from the NOAA ESRL network, shown as data**
1273 **samples per month, per latitudinal band (panels a to l) and per longitudinal bin within each latitudinal band.**

1274
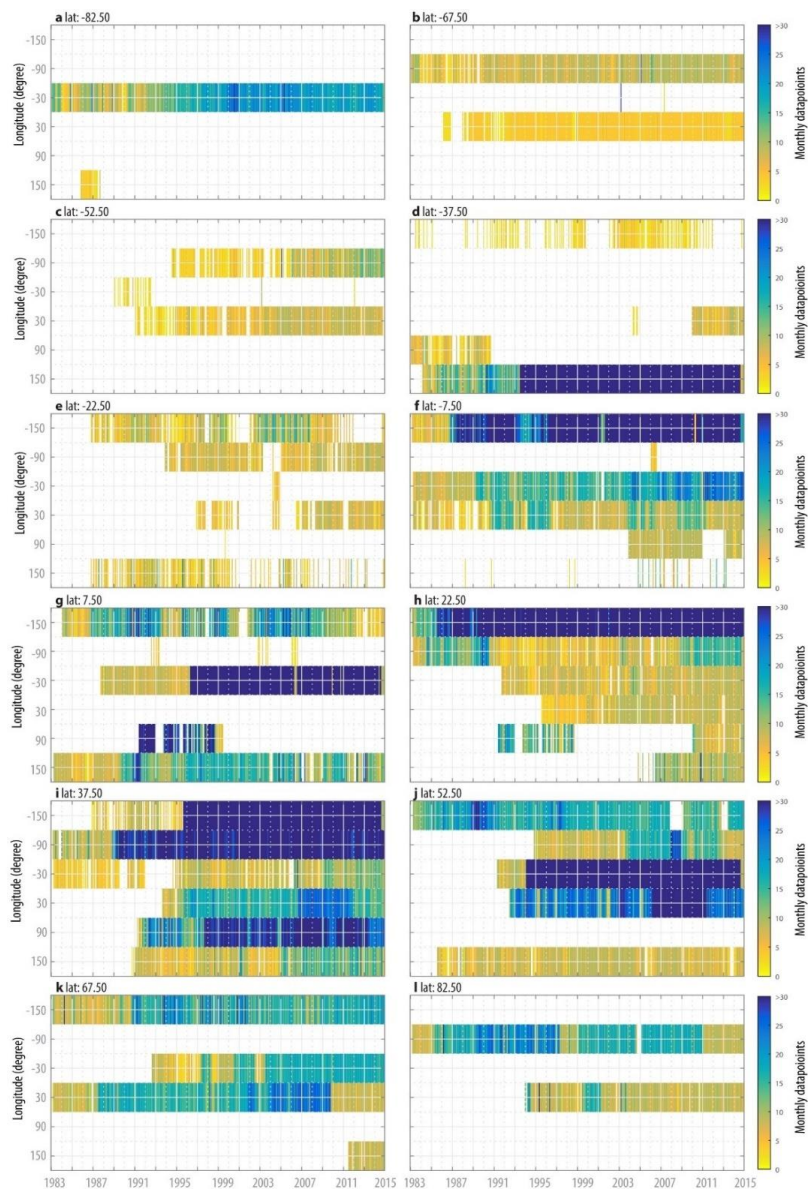
1275

Figure 20 - Availability of instrumental CH₄ data from 1983 to 2015 from the AGAGE and NOAA ESRL networks, shown as data samples per month, per latitudinal band (panels a to l) and per longitudinal bin within each latitudinal band.

1276
1277

1278
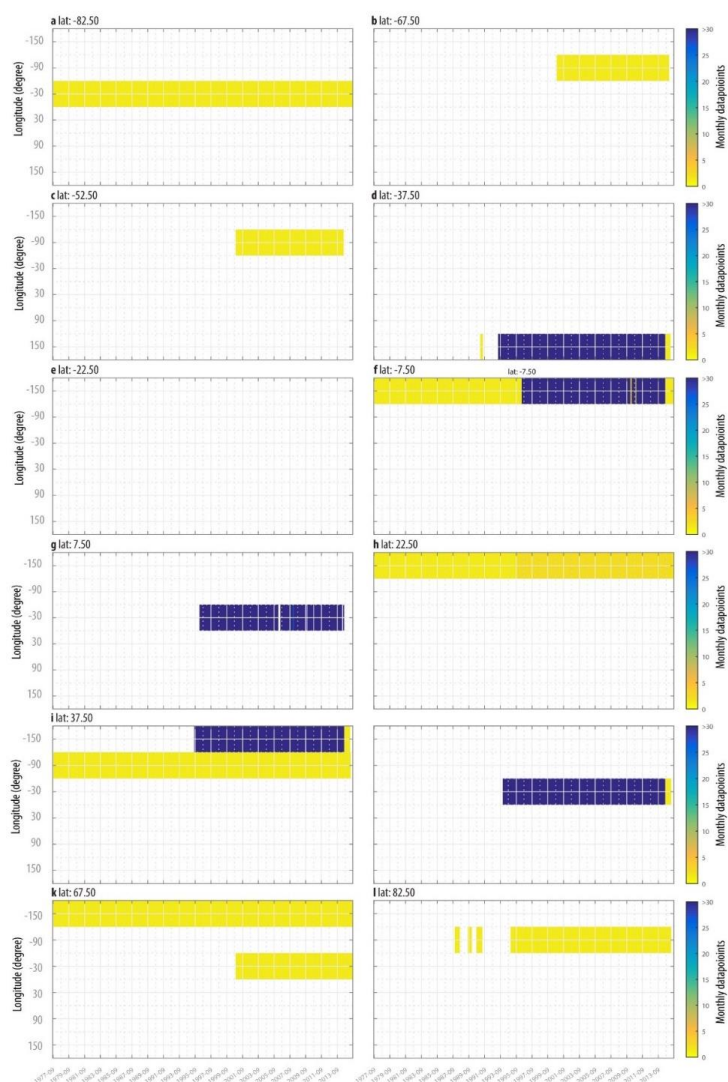
1279

Figure 21 - Availability of instrumental N$_2$O data from 1983 to 2015 from the AGAGE and NOAA ESRL networks, shown as data samples per month, per latitudinal band (panels a to l) and per longitudinal bin within each latitudinal band.

1280
1281

1282
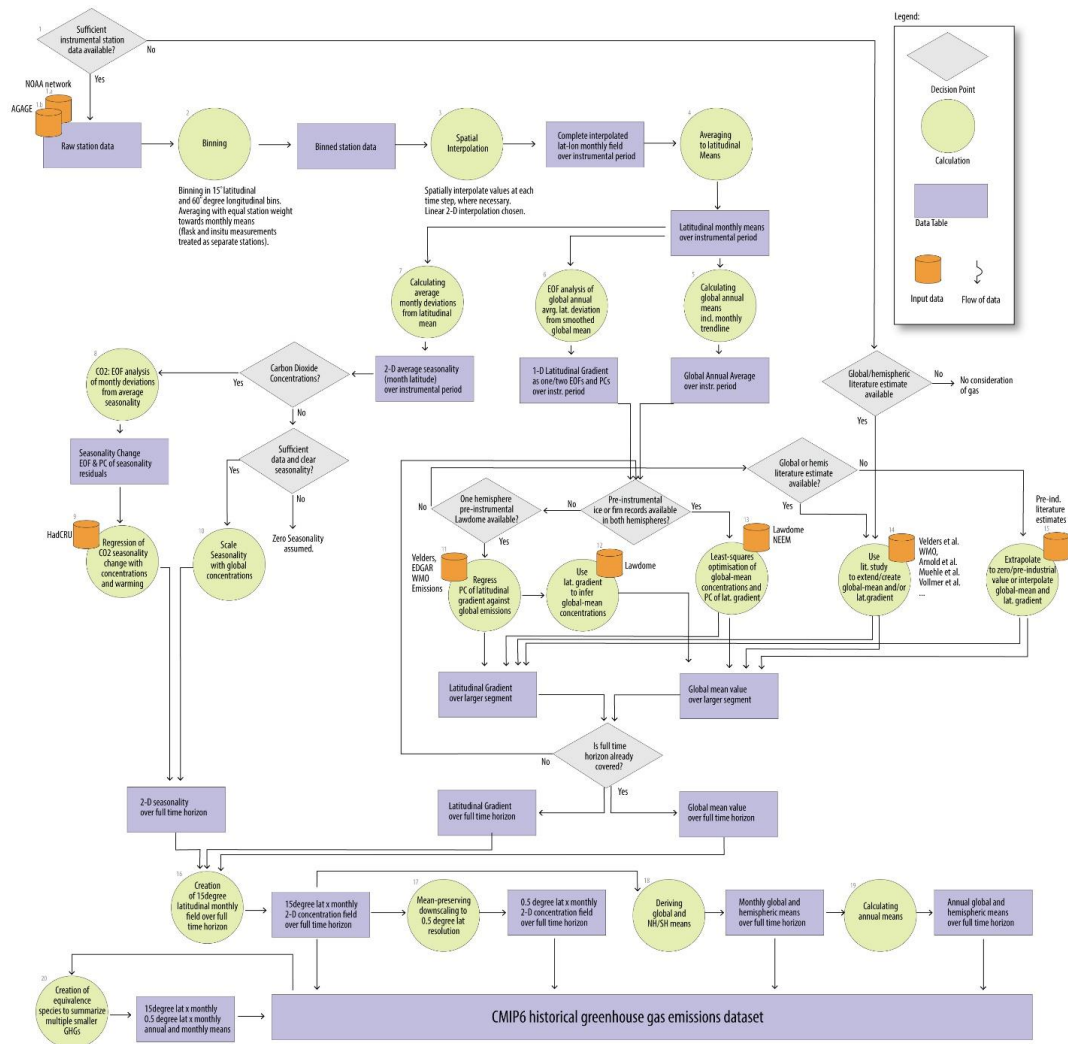
1283

Figure 22 - Data flow diagram of how historical GHG mixing ratios are derived in this study. See text.

1285

1286

1287

1288

1289

1290

1291

1292

13   Appendix A: Individual GHGs other than CO₂, CH₄ and N₂O

1294
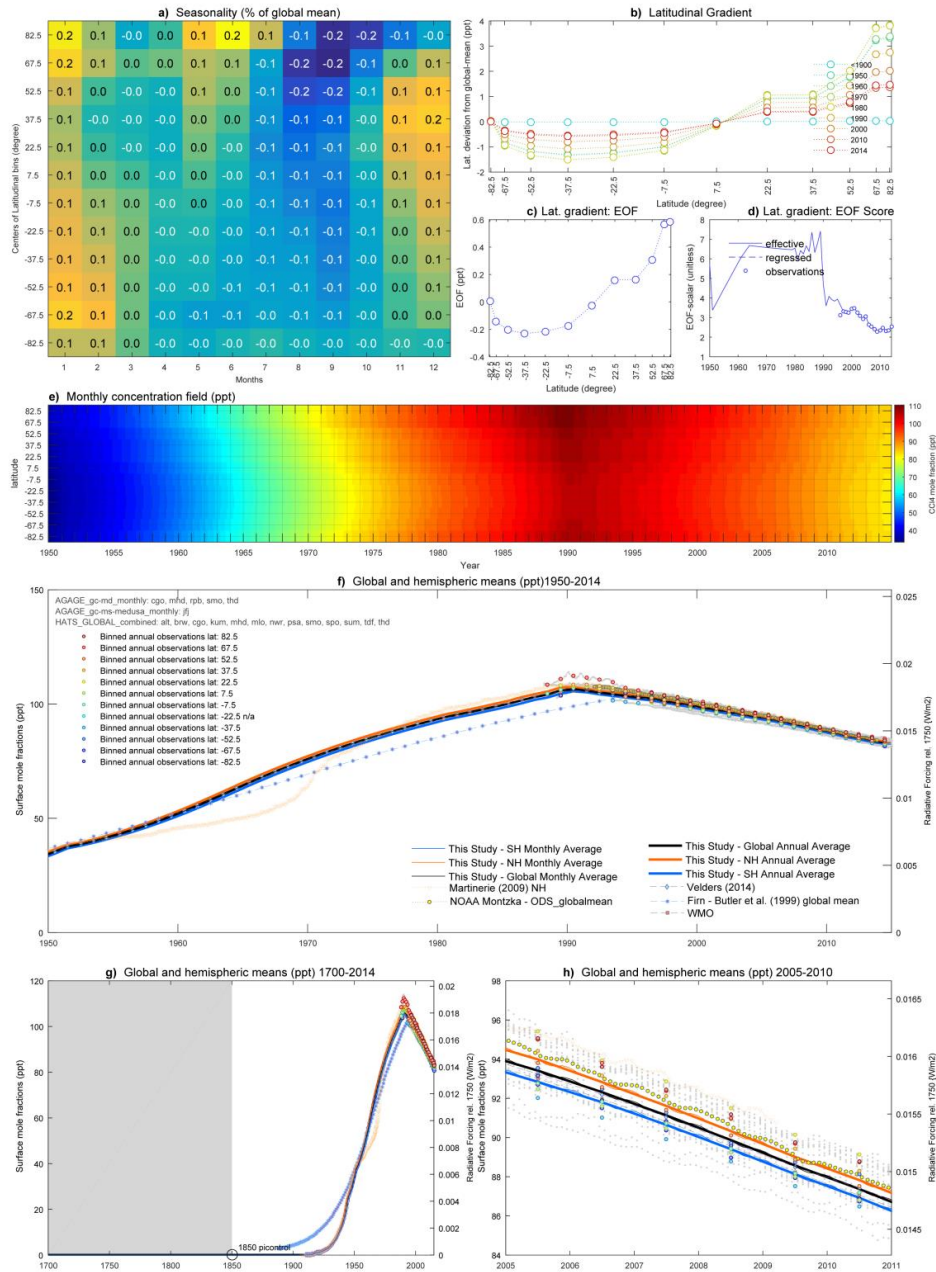
1295

1296   **Figure 23 - CCl4 Factsheet**
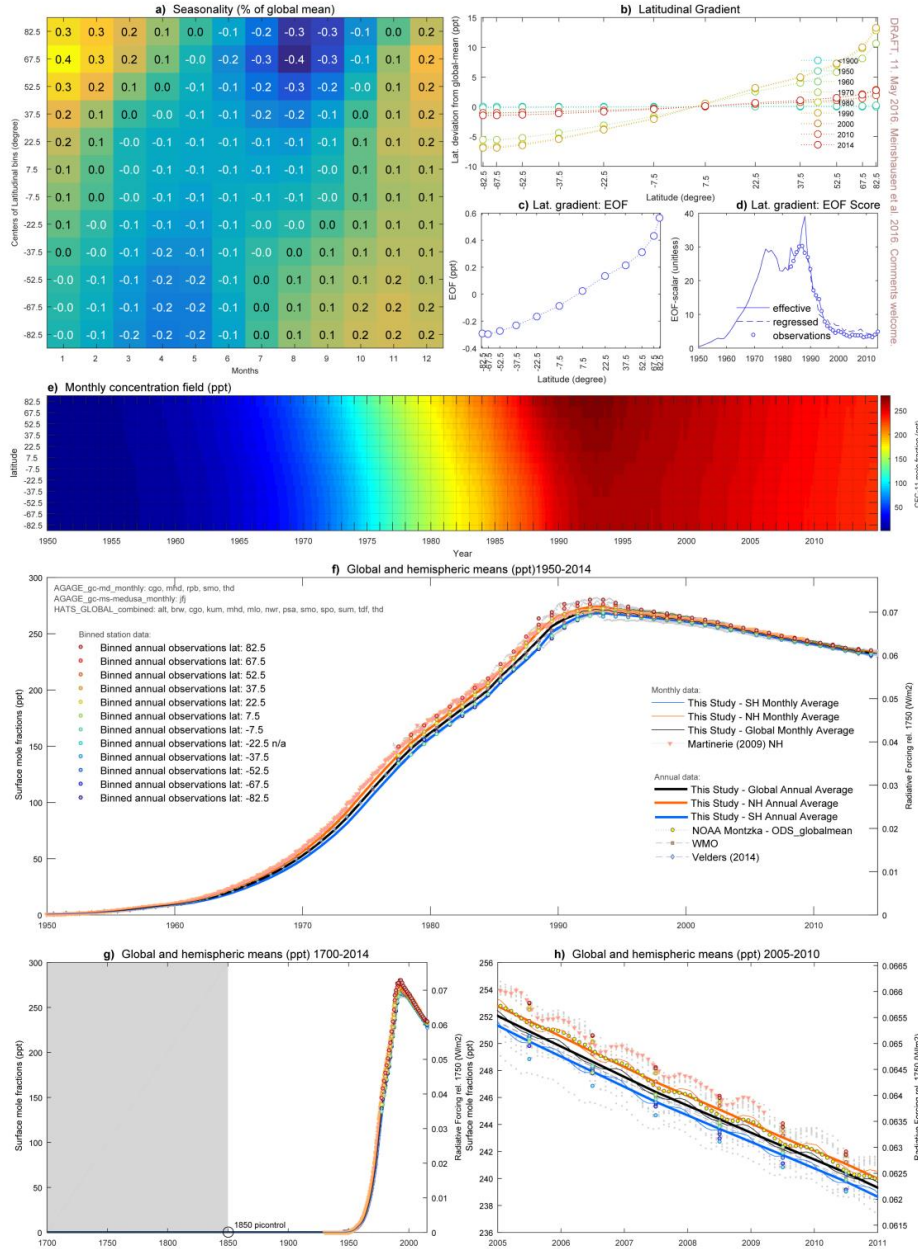
1297

Figure 24 - CFC-11 Factsheet
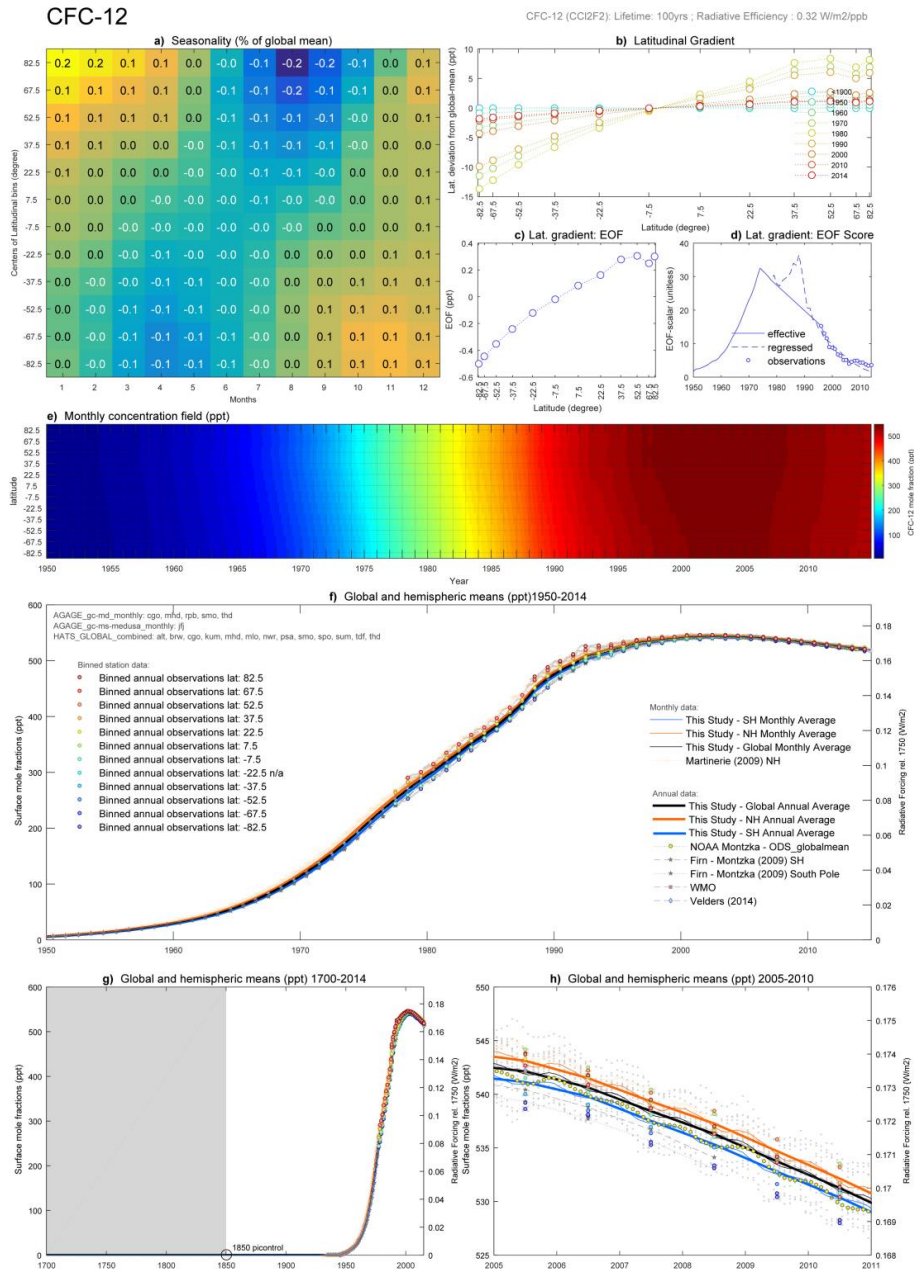
1299

1300   **Figure 25 – CFC-12 Factsheet**
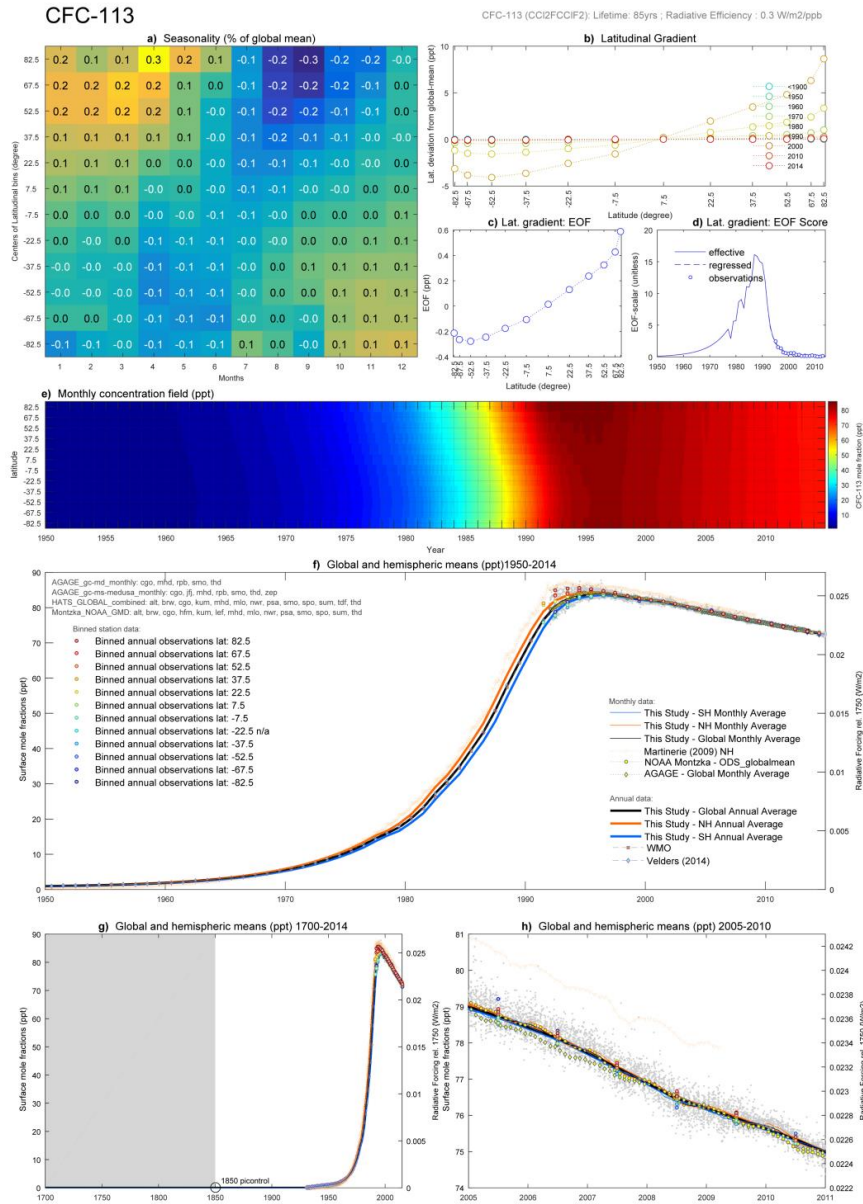
1301

1302 **Figure 26 - CFC-113 Factsheet**
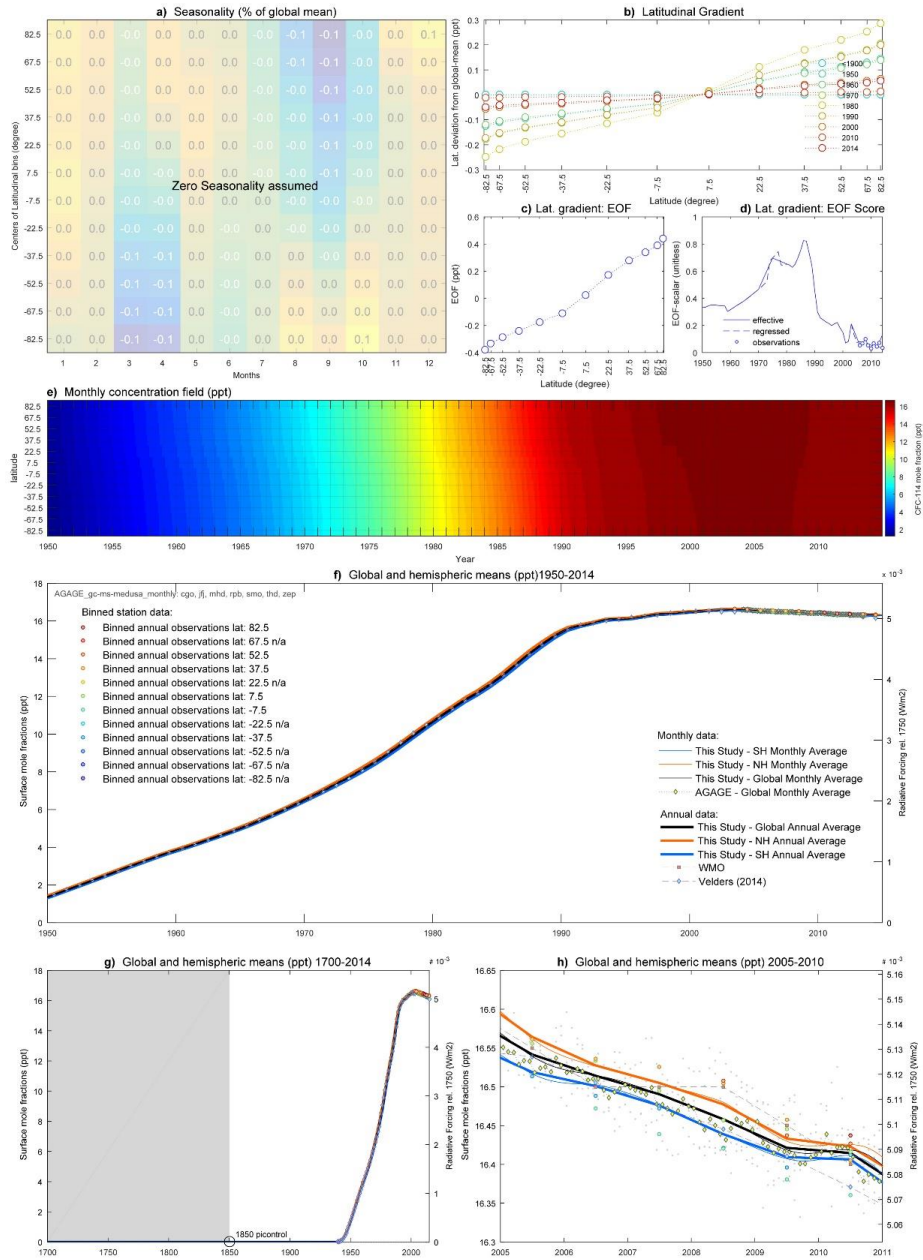
1303

1304   **Figure 27 - CFC-114 Factsheet**
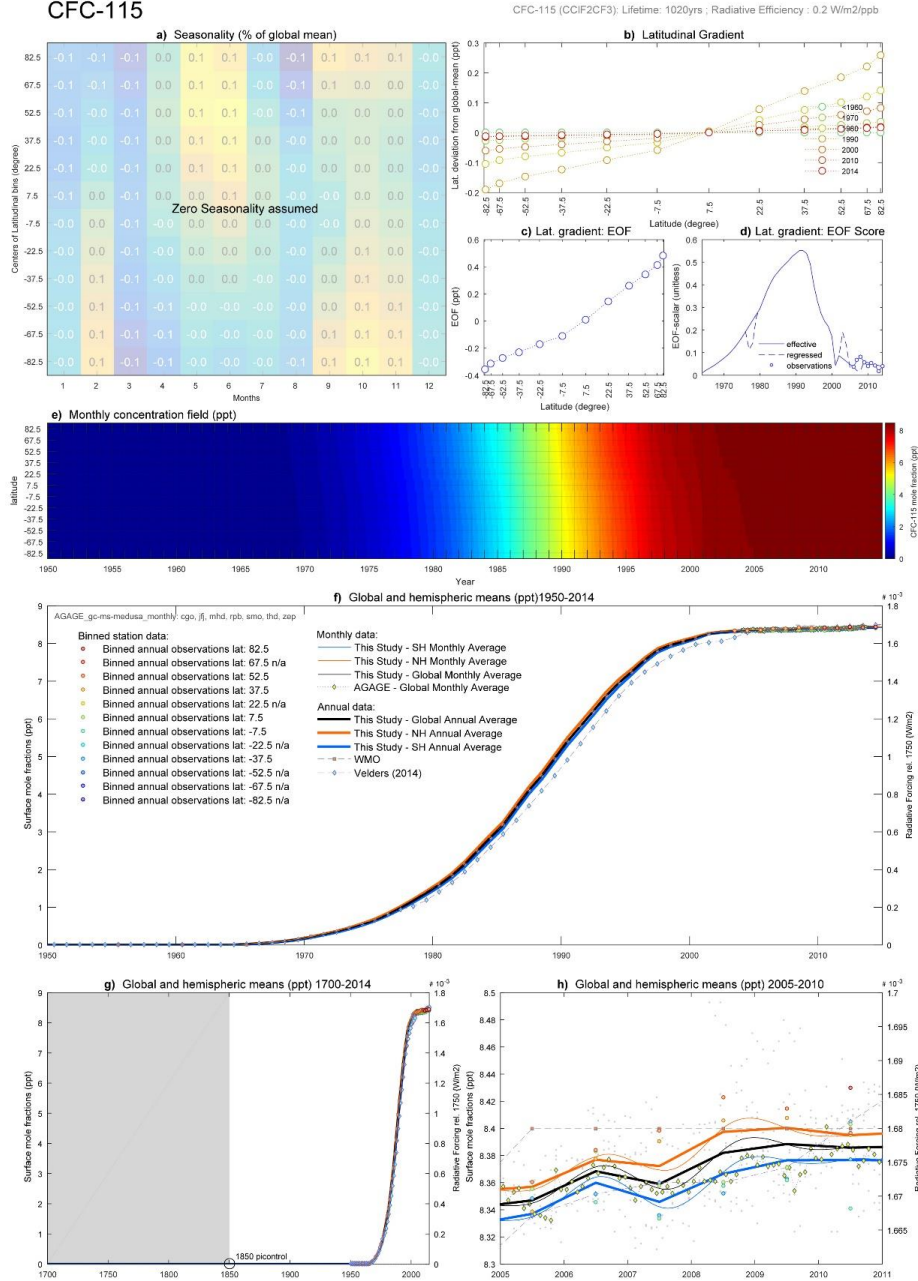
1305

1306   **Figure 28 - CFC-115 Factsheet**
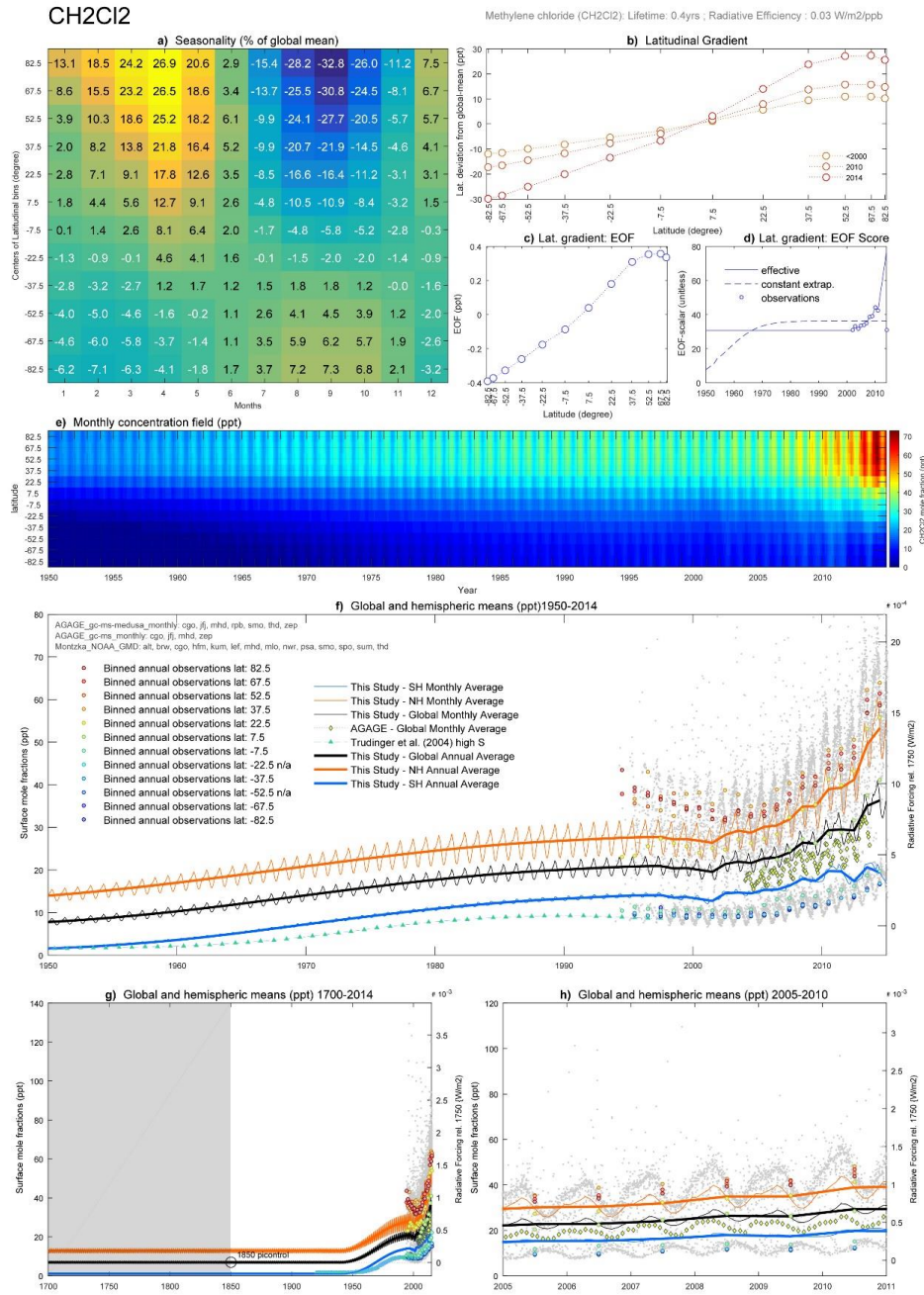
1307

Figure 29 - CH2Cl2 Factsheet
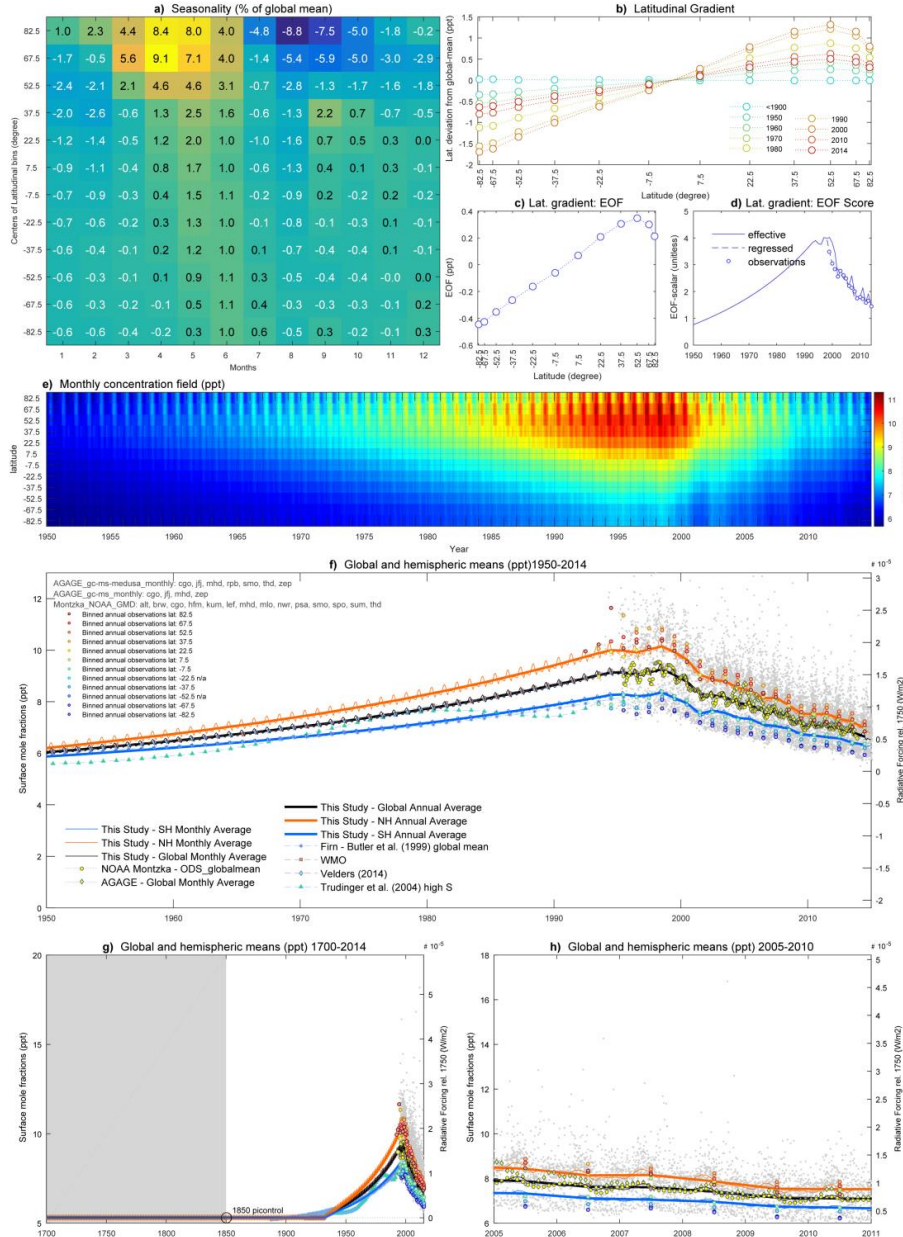
1309

Figure 30 - CH3Br Factsheet
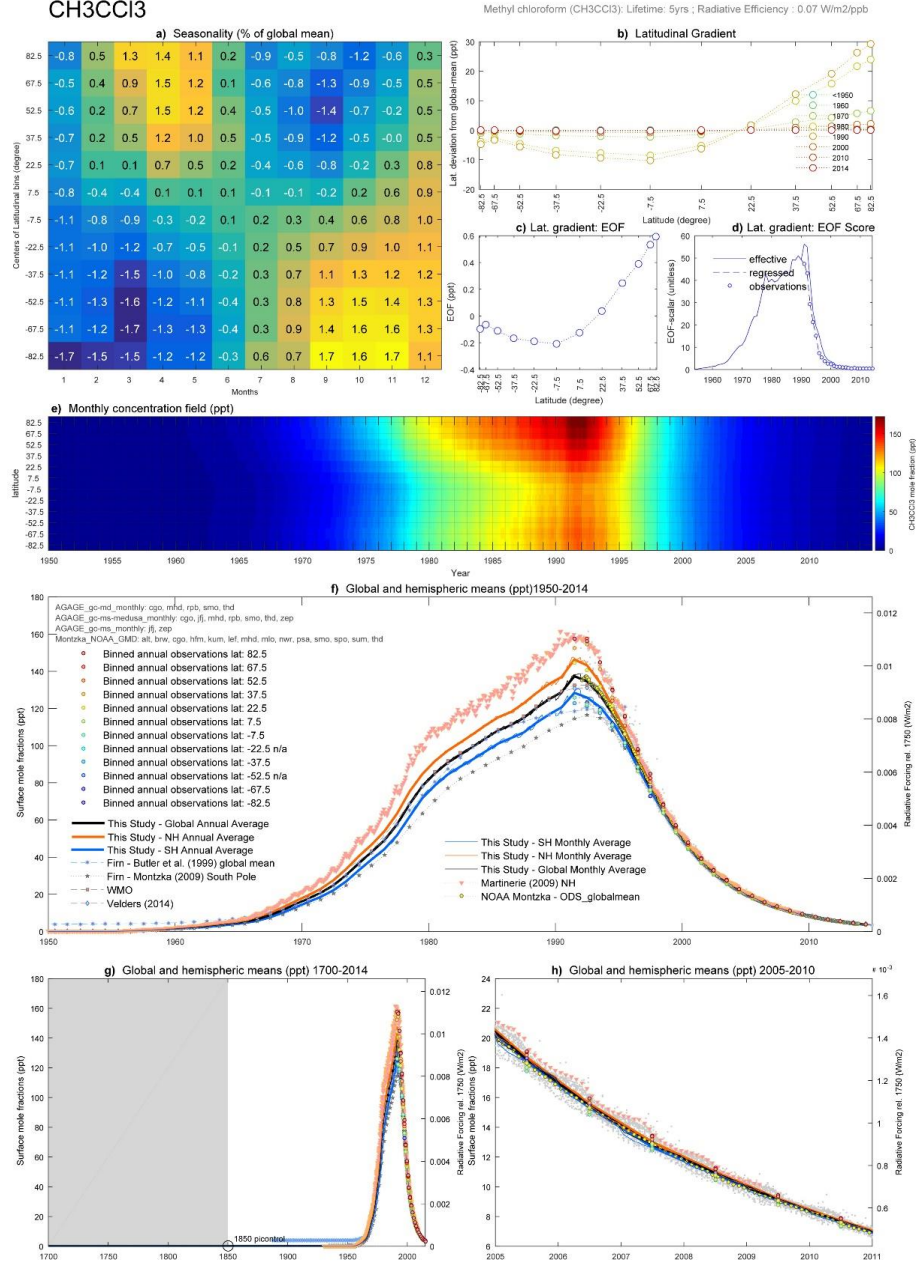
1311

1312   **Figure 31 - CH3CCl3 Factsheet**
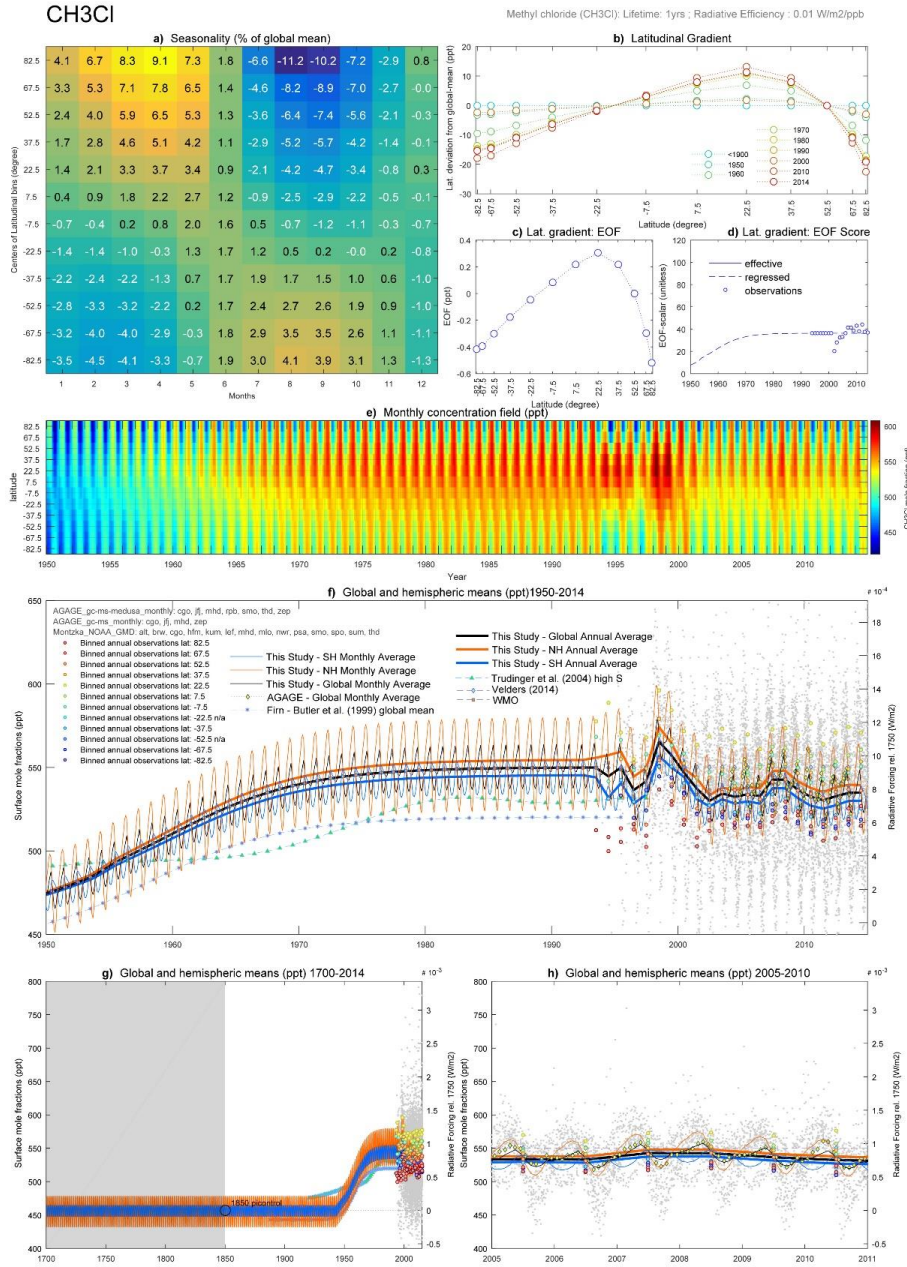
1313

1314   **Figure 32 - CH3Cl Factsheet**
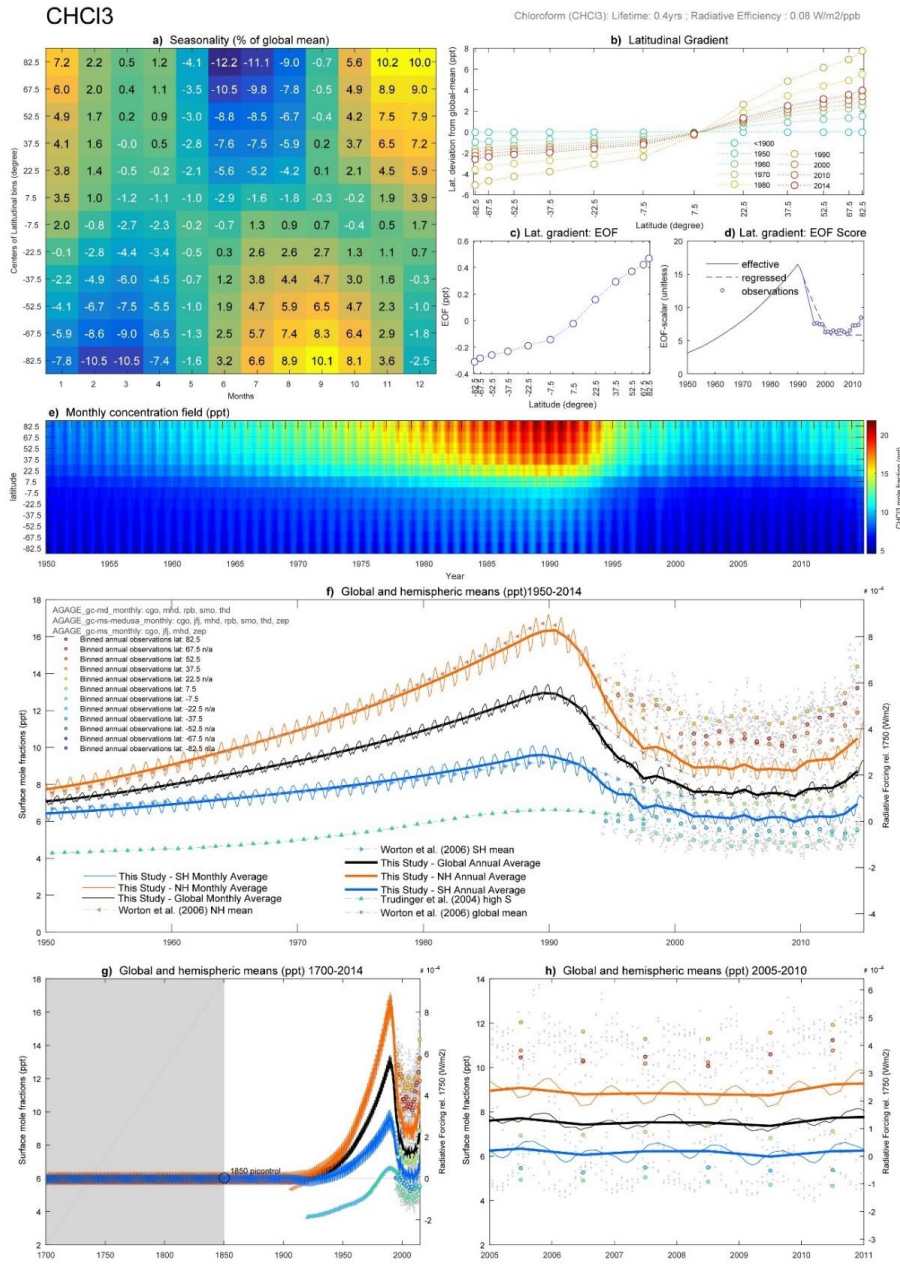
1315

1316 **Figure 33 - CHCl3 Factsheet**
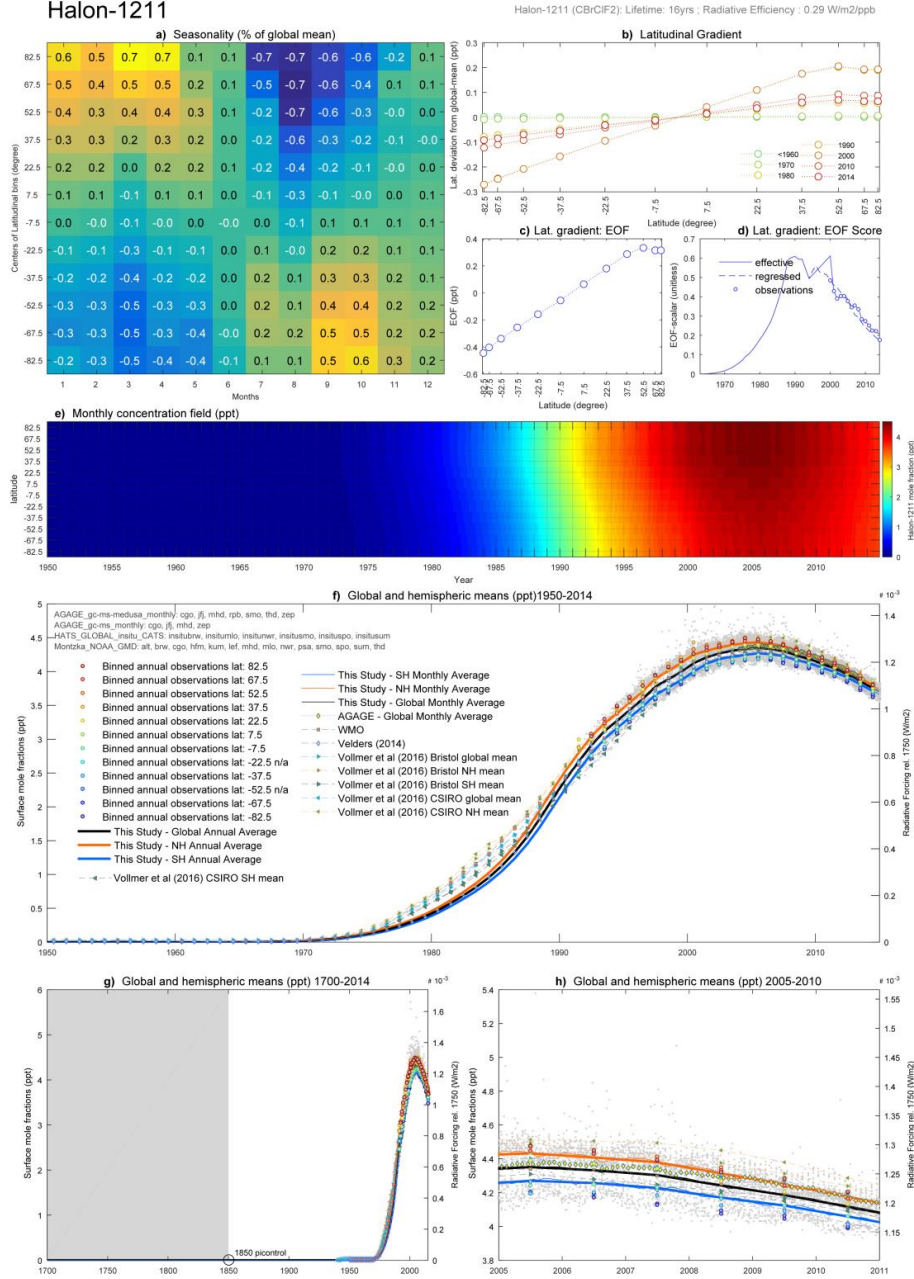
1317

Figure 34 - Halon-1211 Factsheet
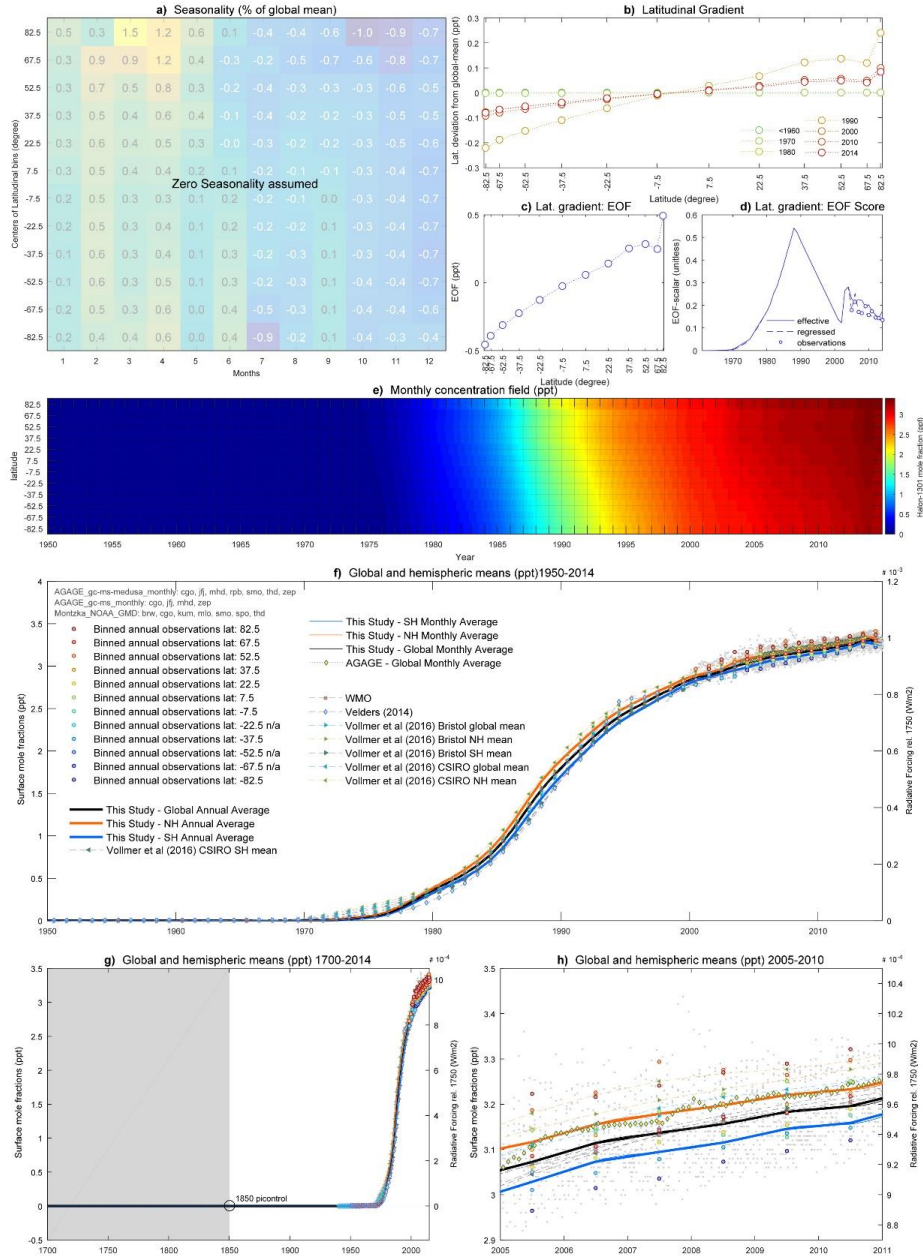
1319

Figure 35 - Halon-1301 Factsheet
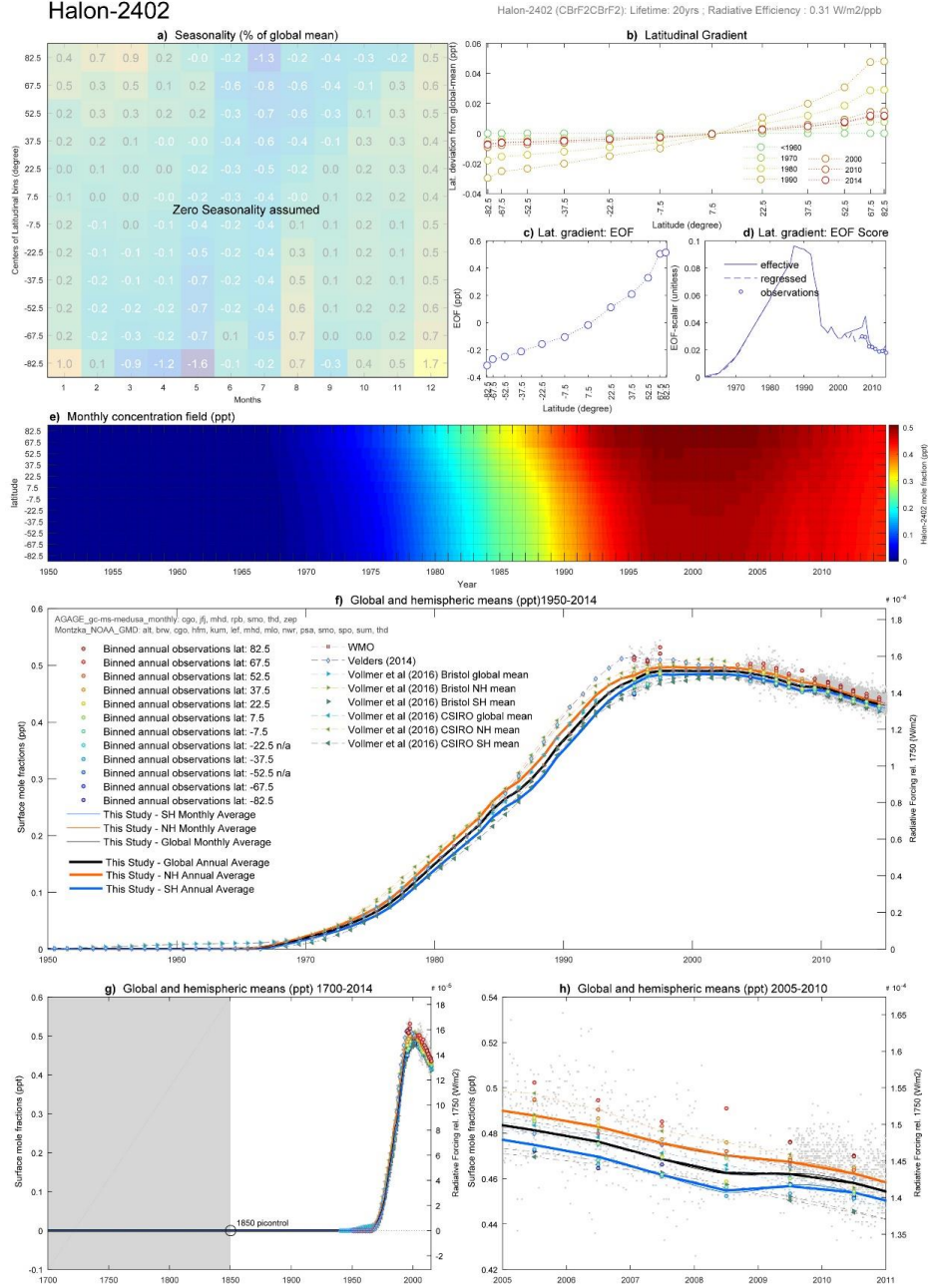
1321

1322   **Figure 36 - Halon-2402 Factsheet**
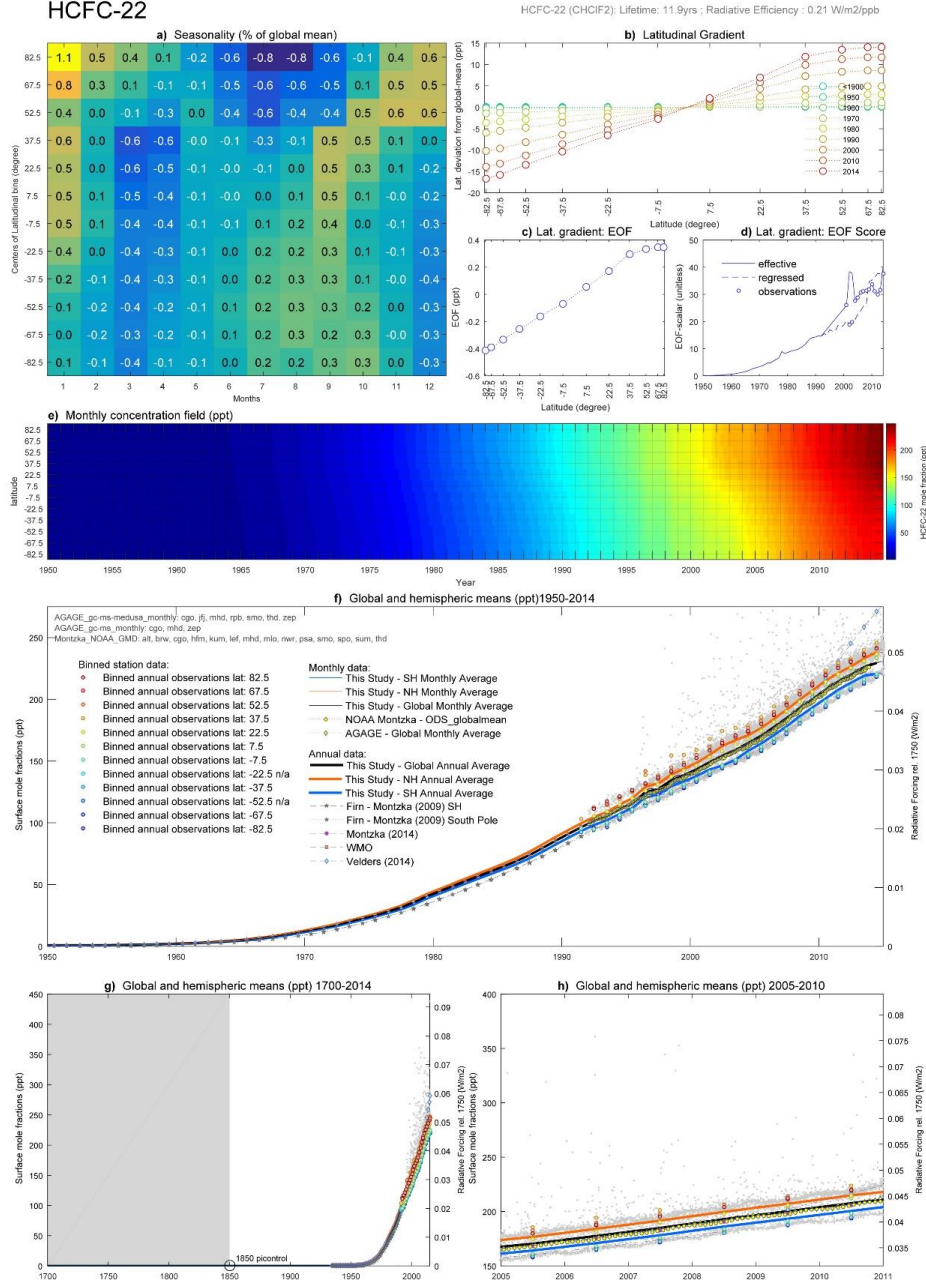
1323

1324   **Figure 37 - HCFC-22 Factsheet**
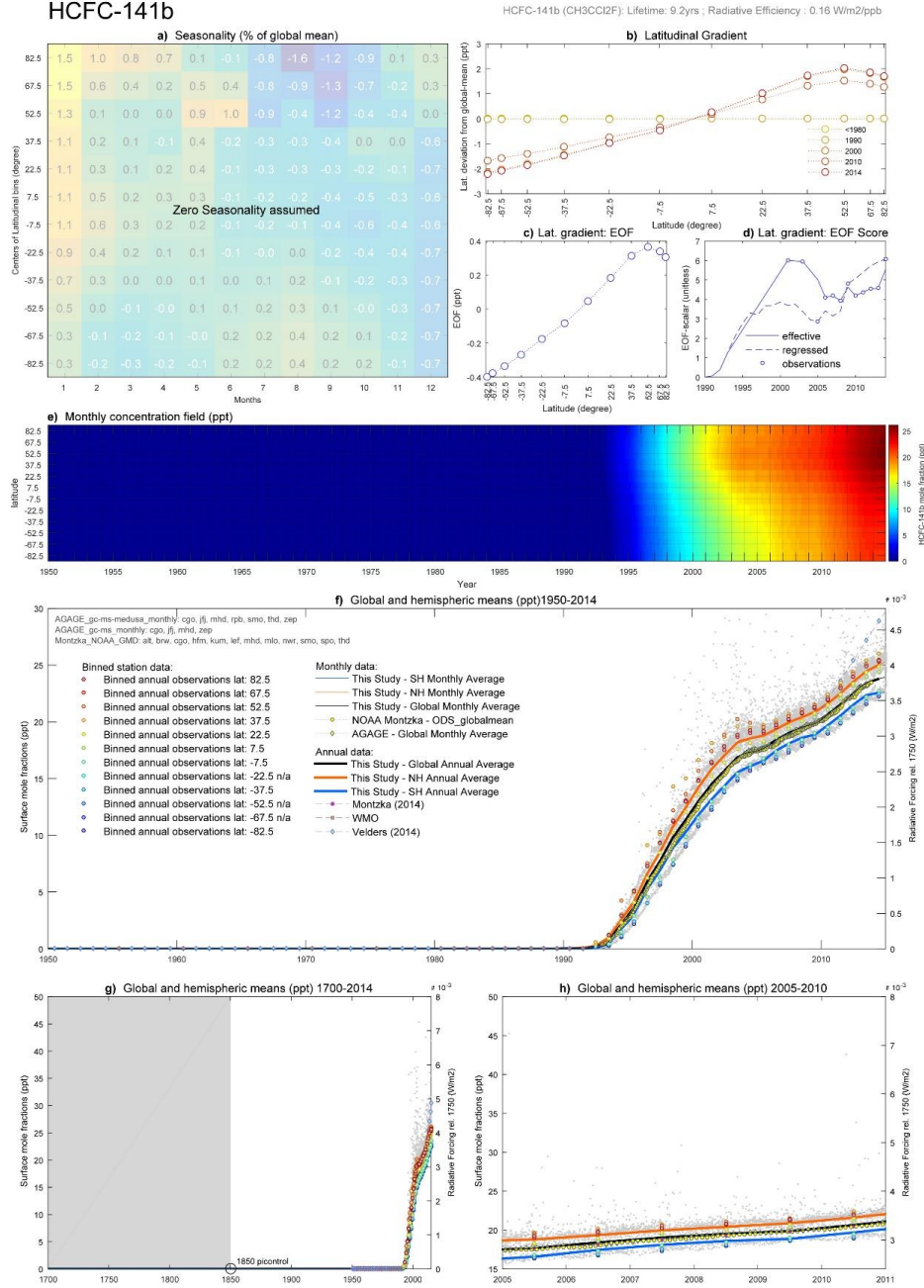
1325

1326   **Figure 38 - HCFC-141b Factsheet**
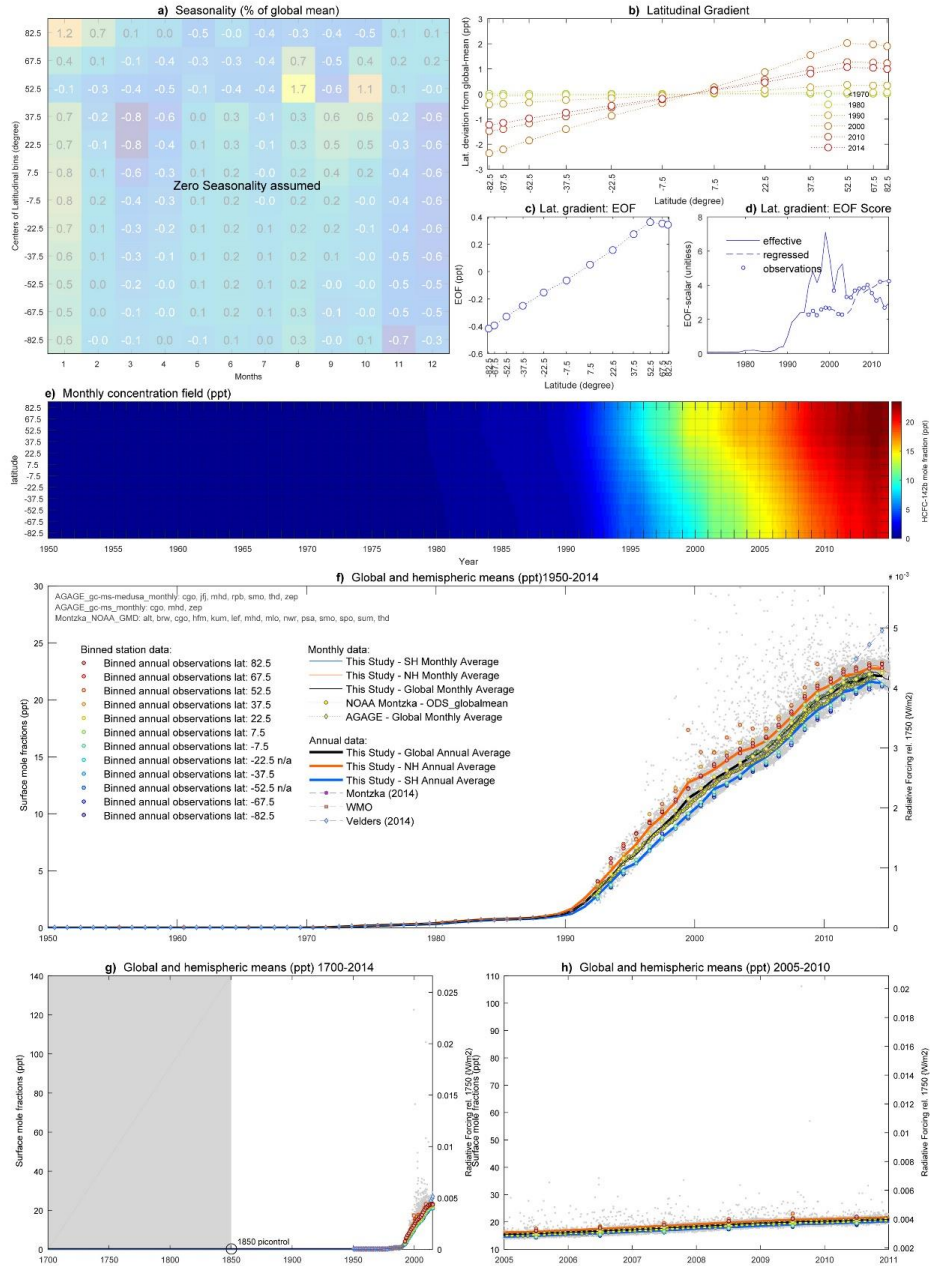
1327

Figure 39 - HCFC-142b Factsheet
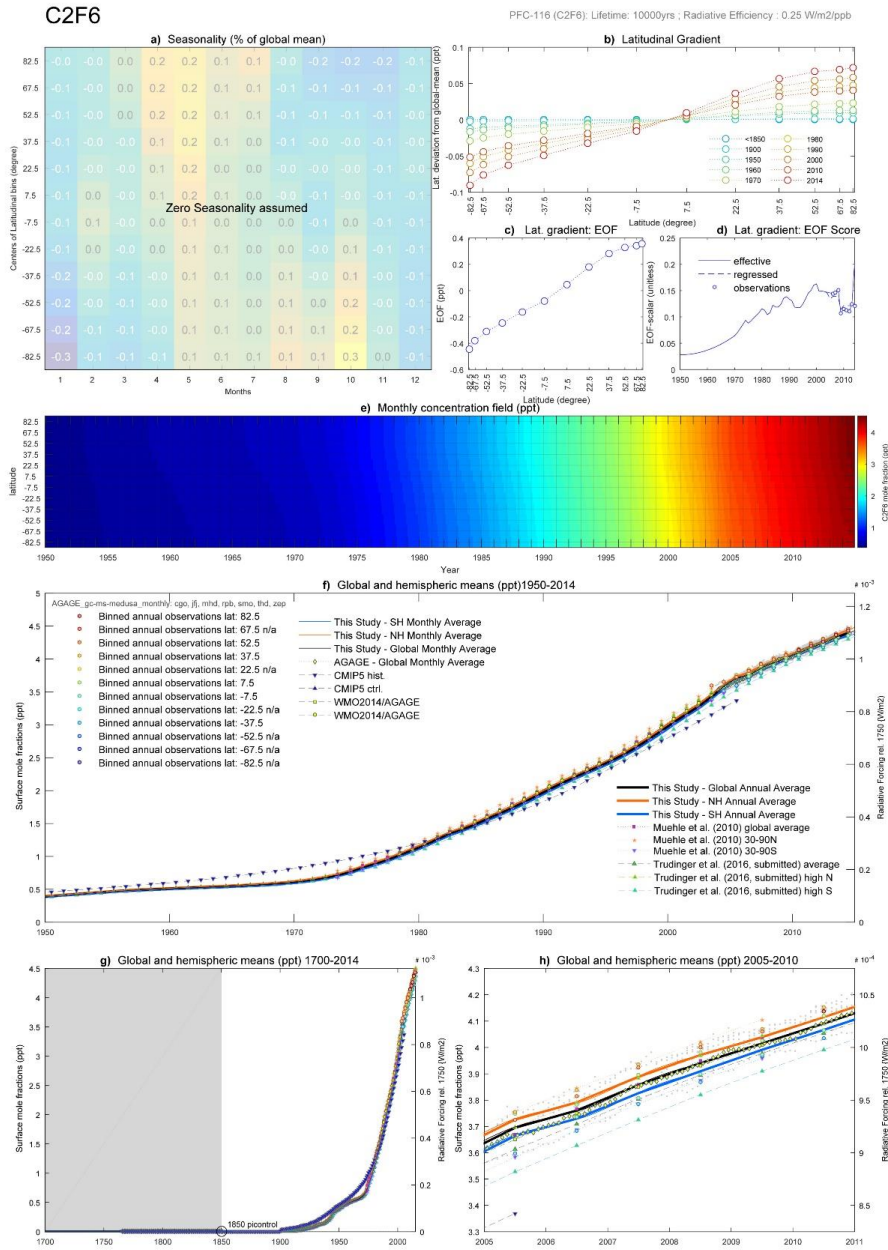
1329

Figure 40 - C2F6 Factsheet
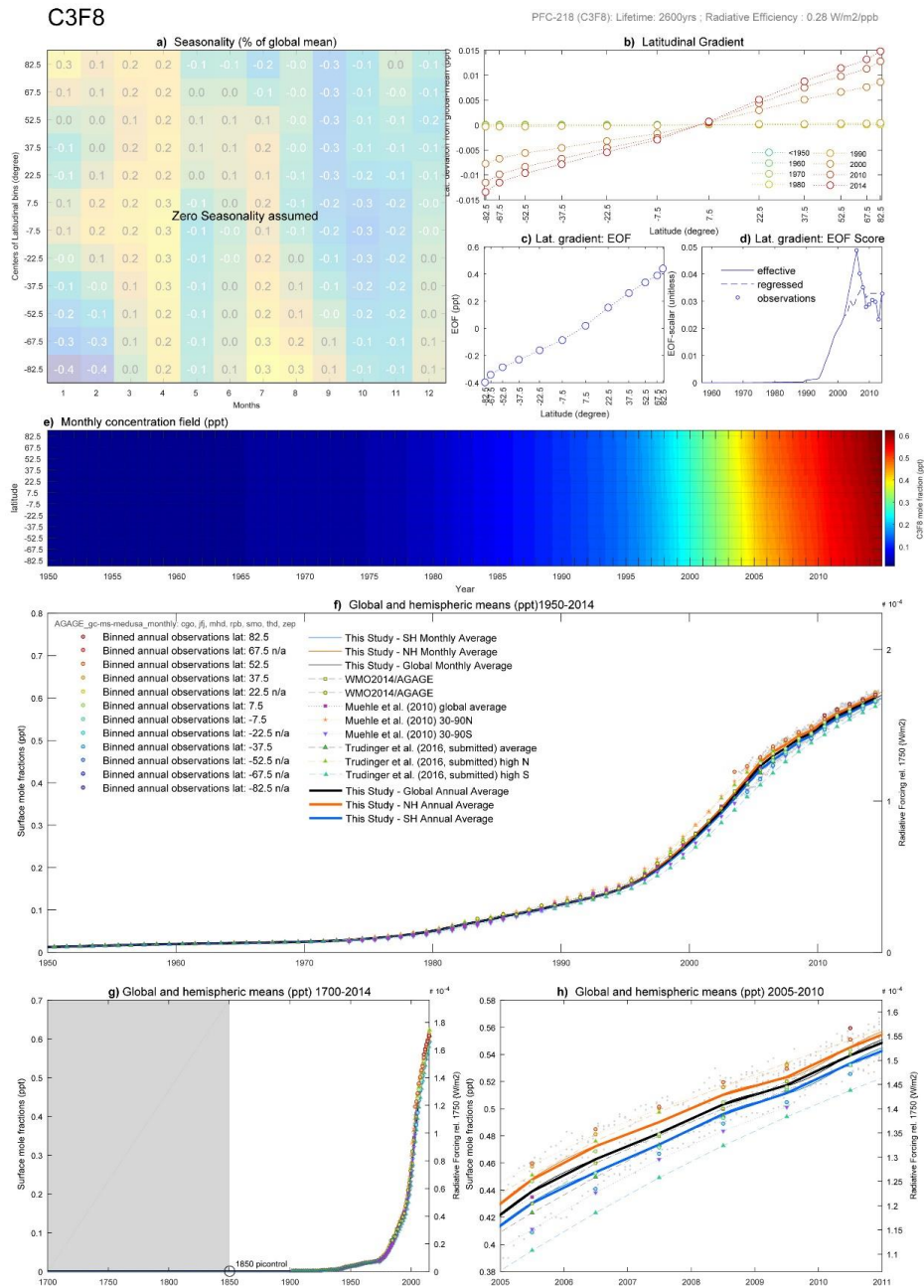
1331

Figure 41 - C3F8 Factsheet
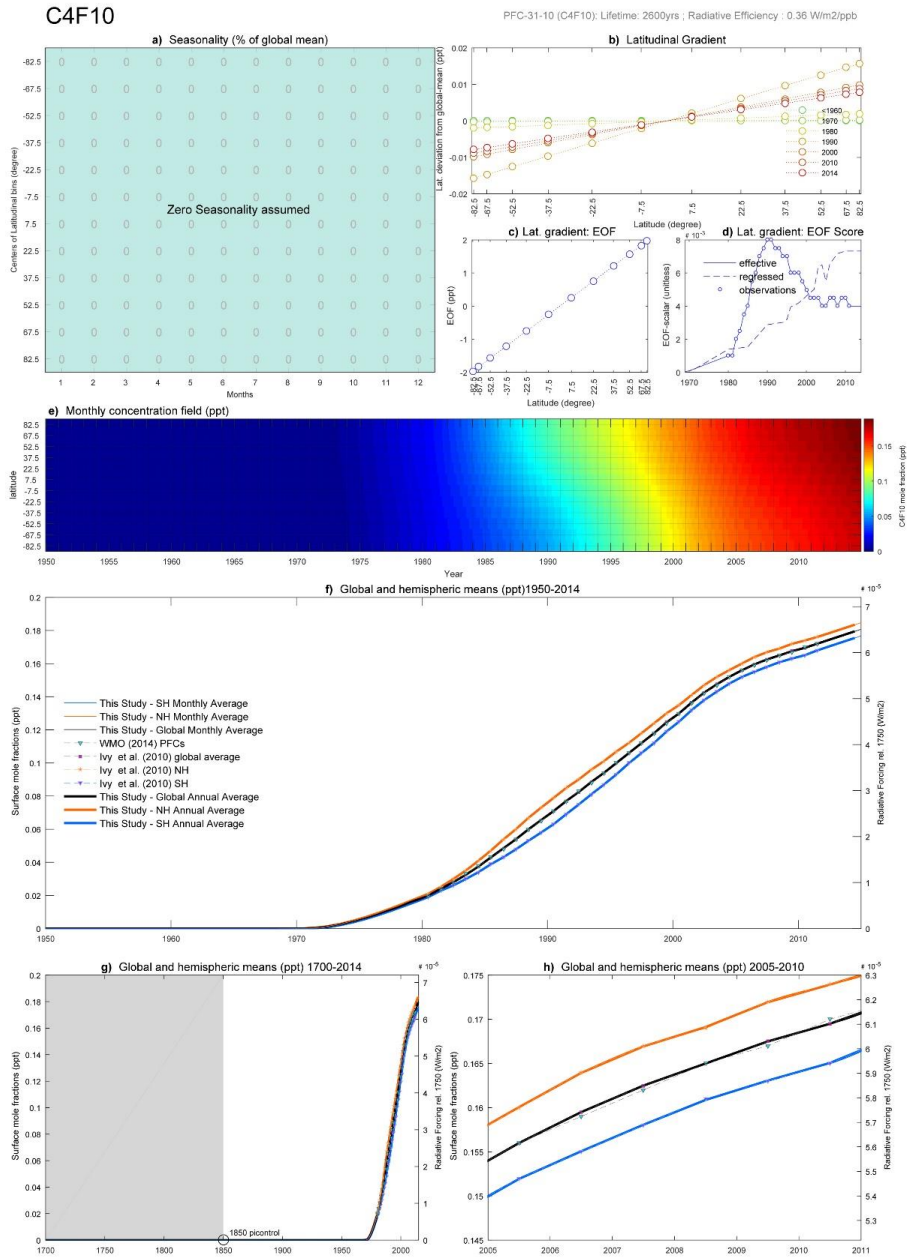
1333

Figure 42 - C4F10 Factsheet
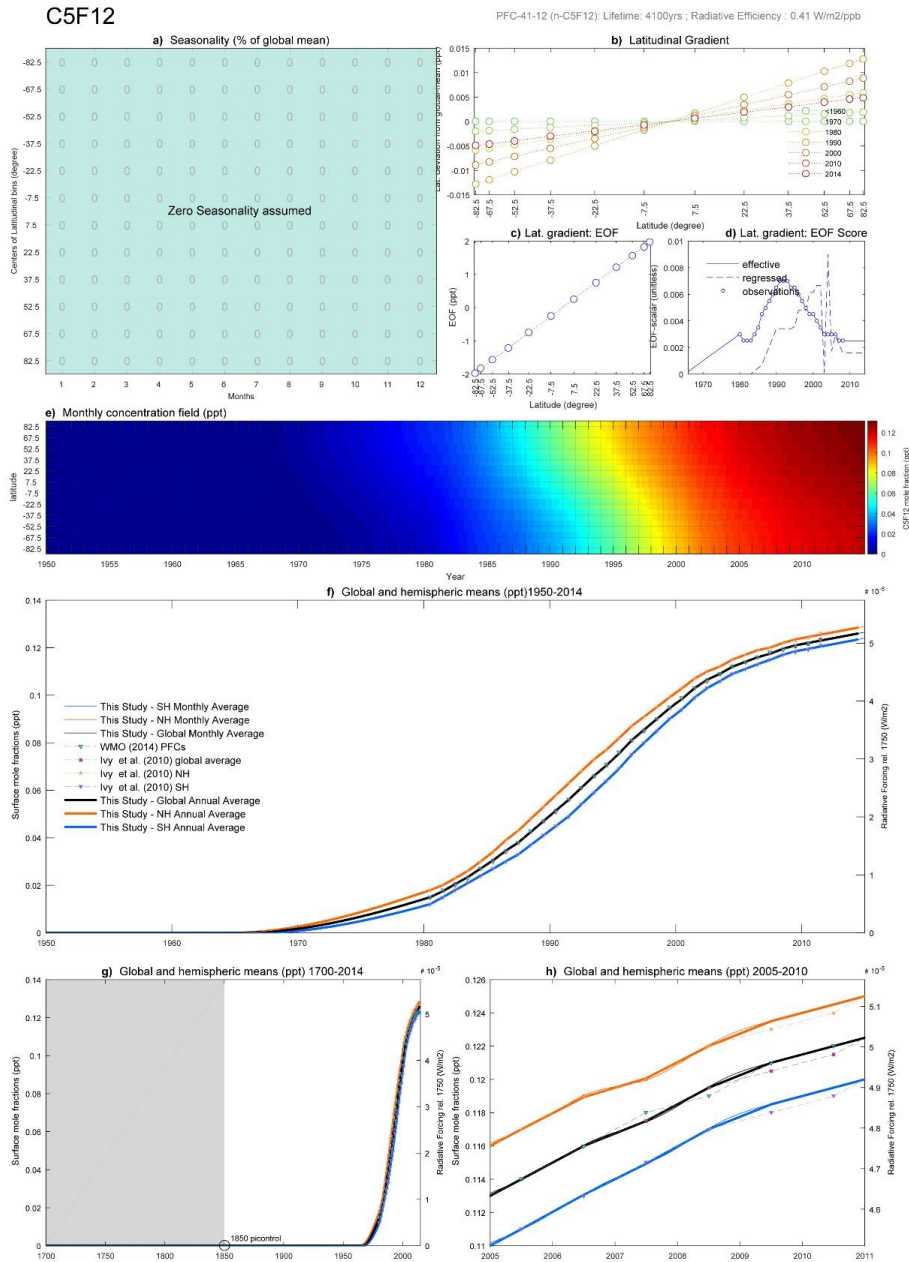
1335

1336   **Figure 43 - C5F12 Factsheet**
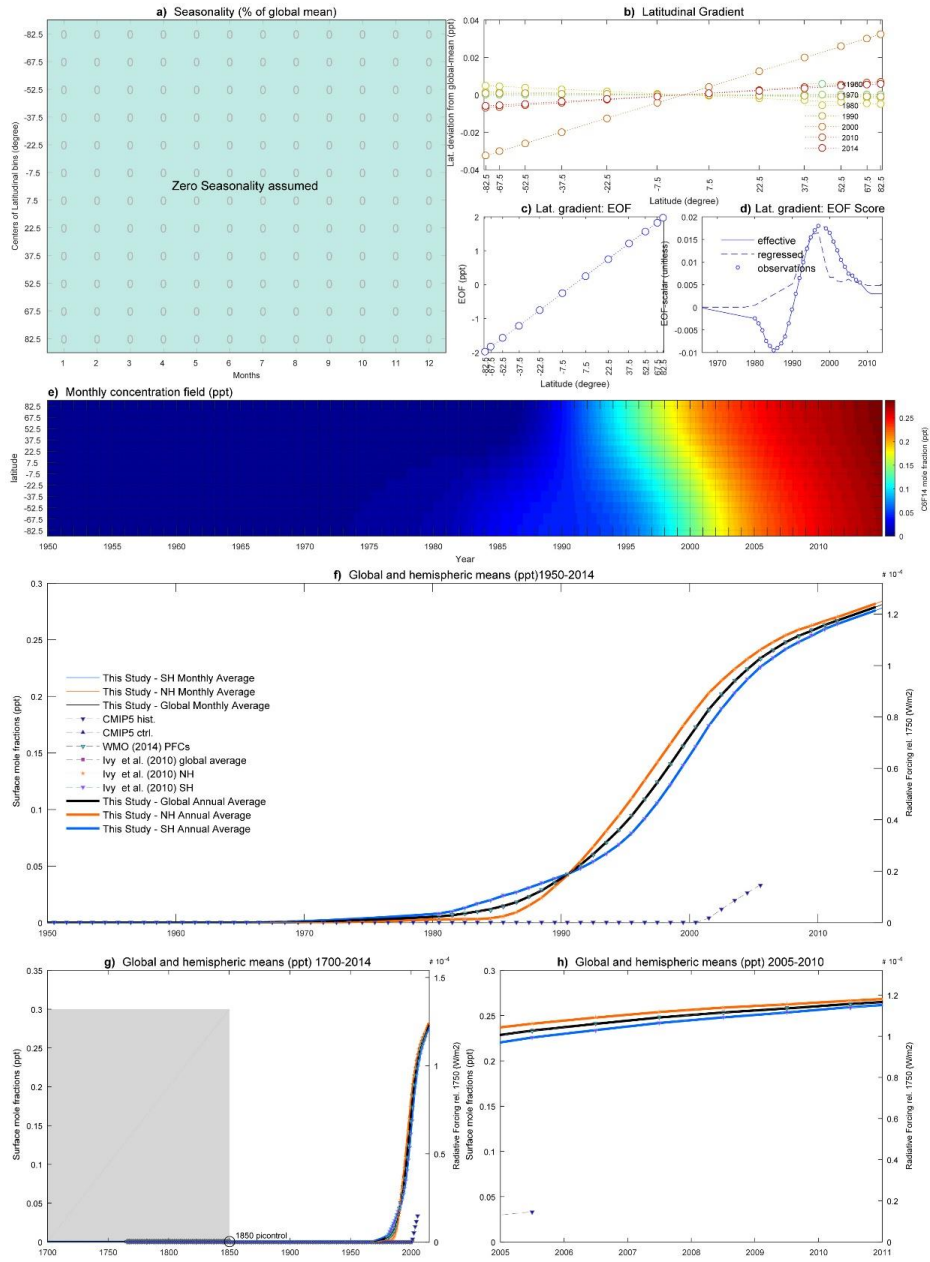
1337

Figure 44 - C6F14 Factsheet
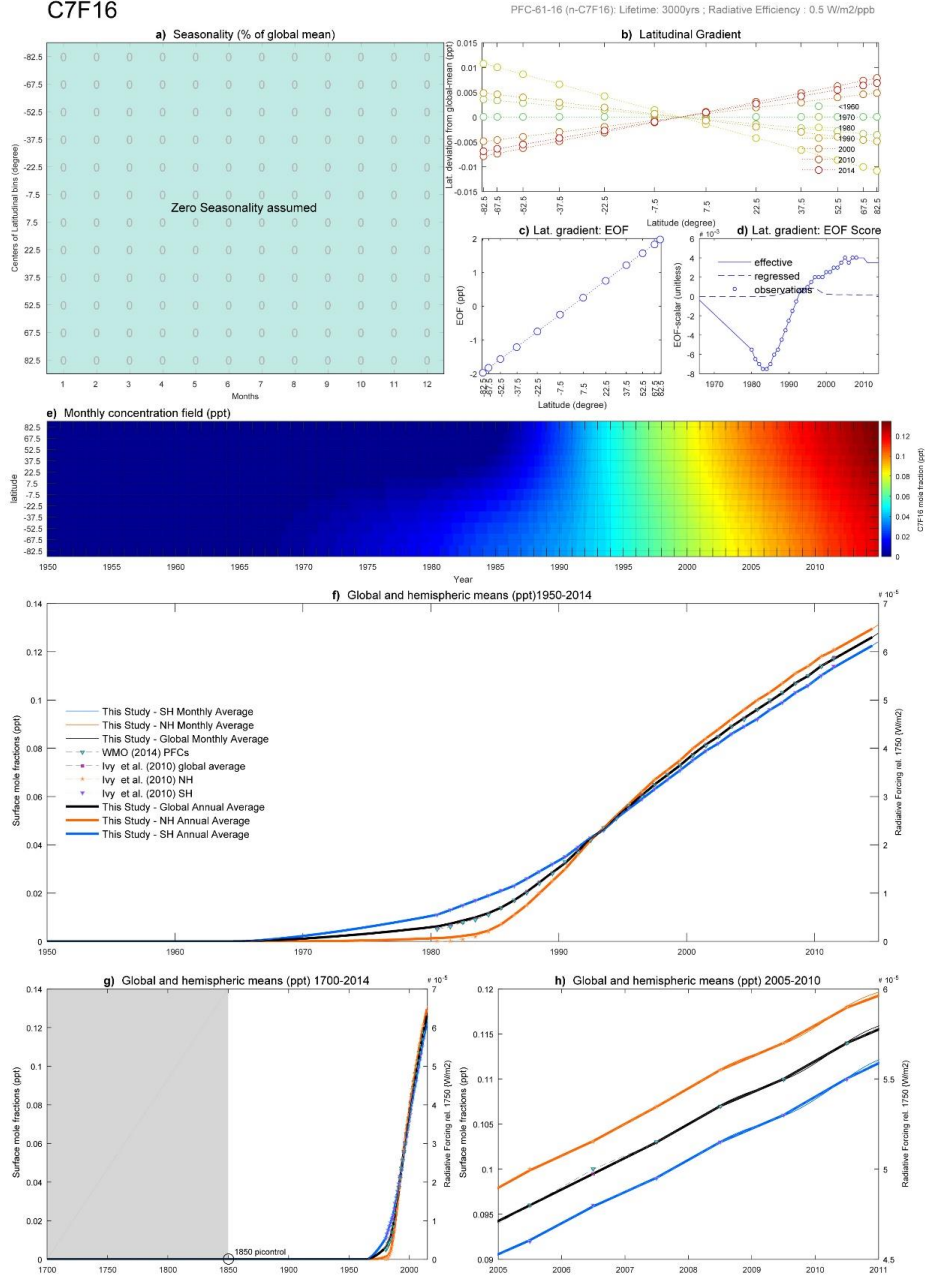
1339

Figure 45 - C7F16 Factsheet
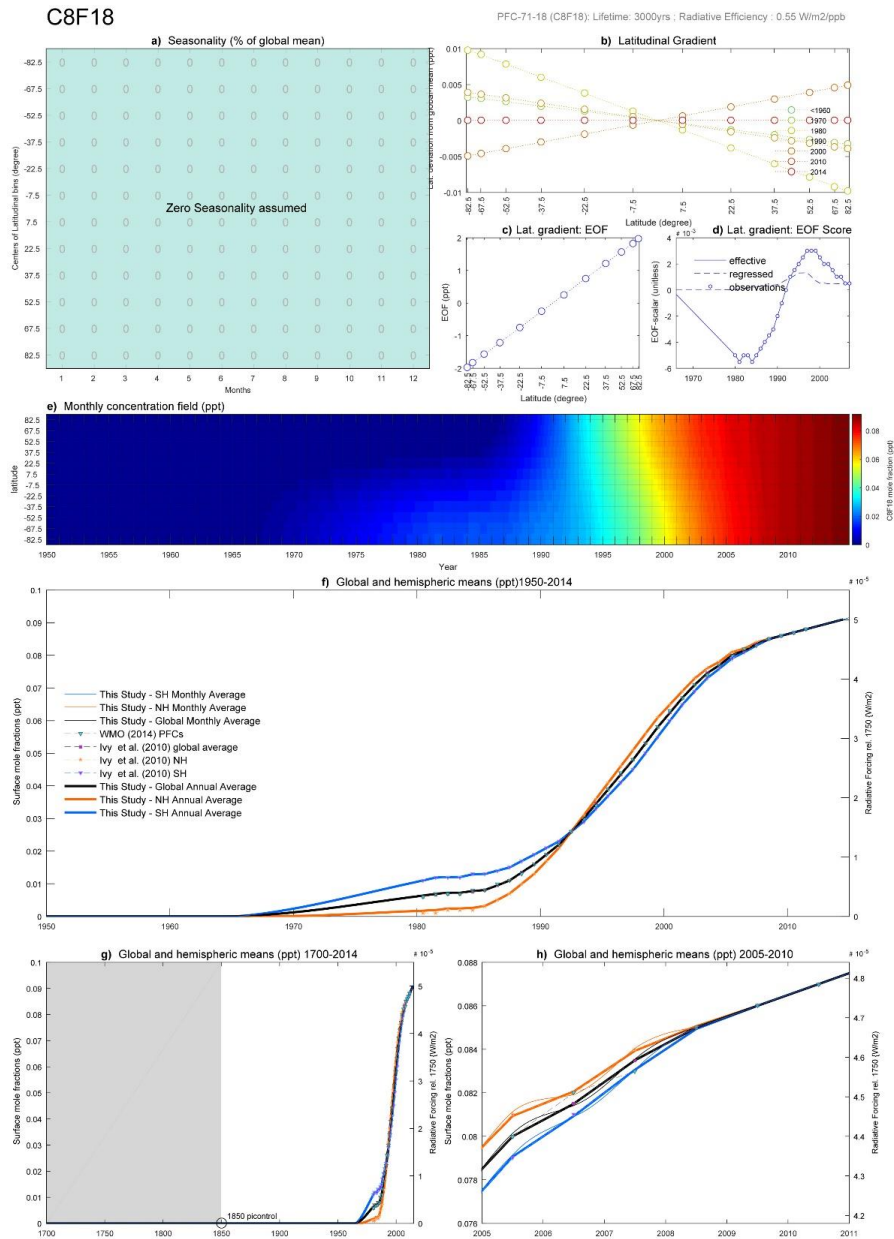
1341

1342   **Figure 46 - C8F18 Factsheet**
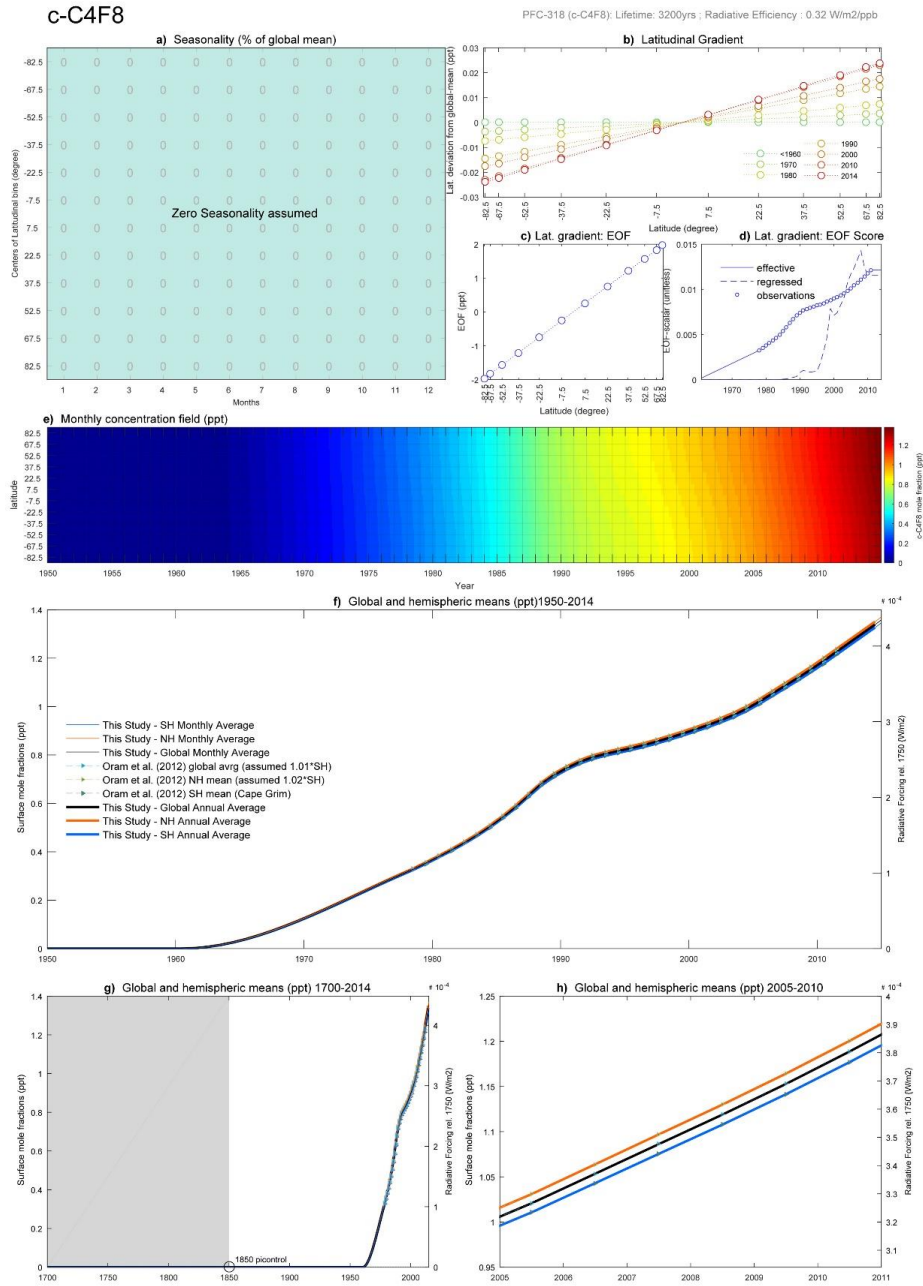
1343

1344   **Figure 47 - c-C4F8 Factsheet**
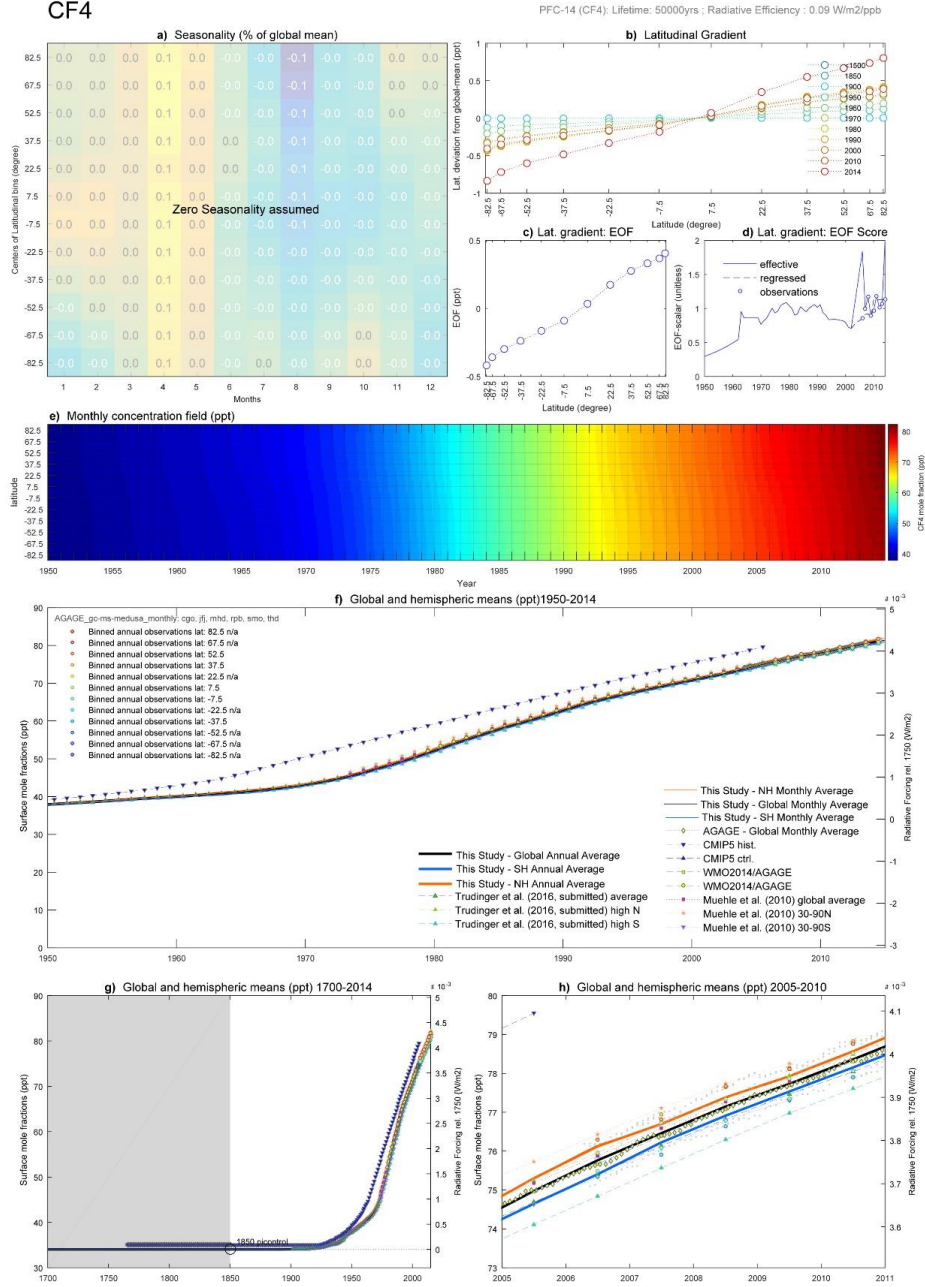
Figure 48 - CF4 Factsheet
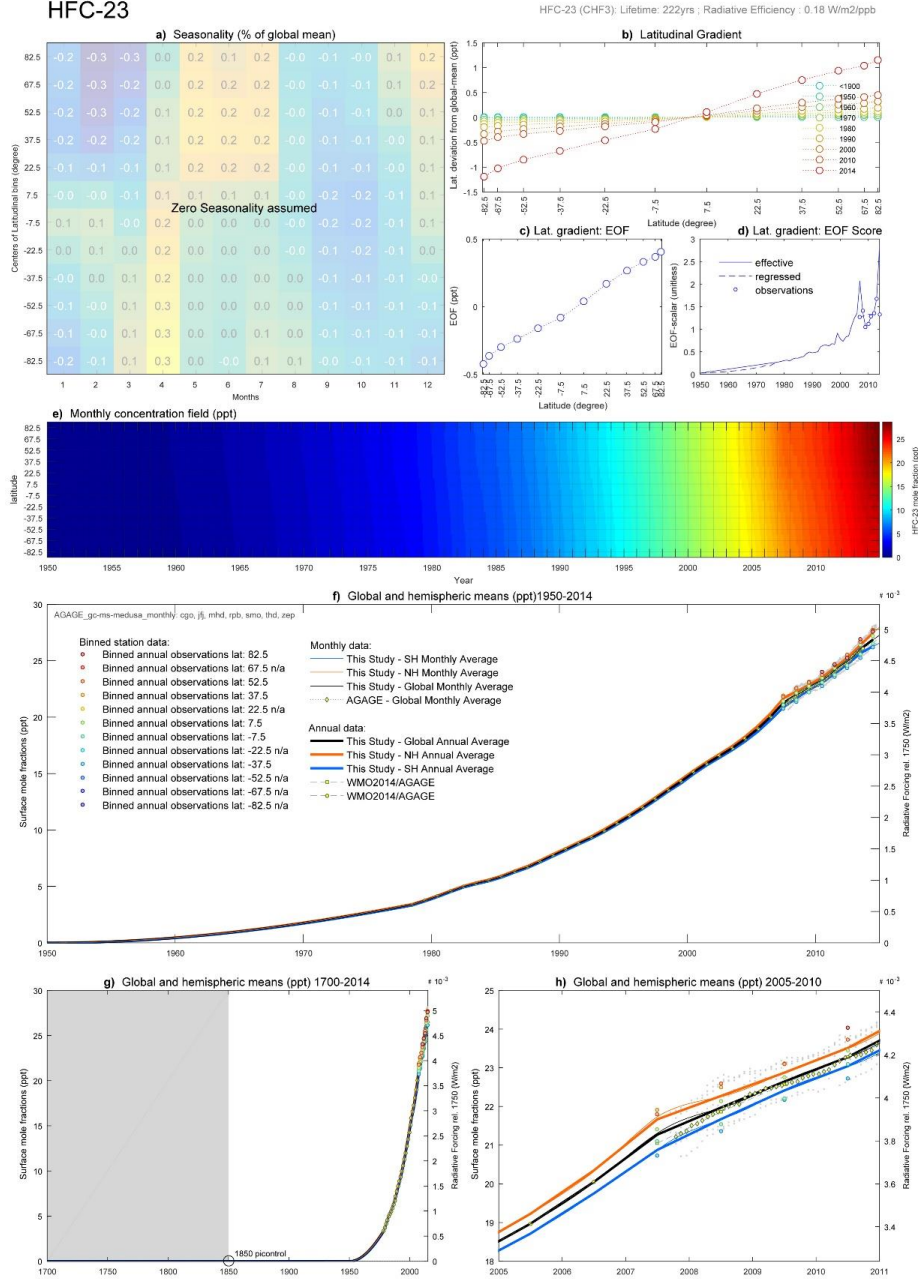
1347

1348   **Figure 49 - HFC-23 Factsheet**
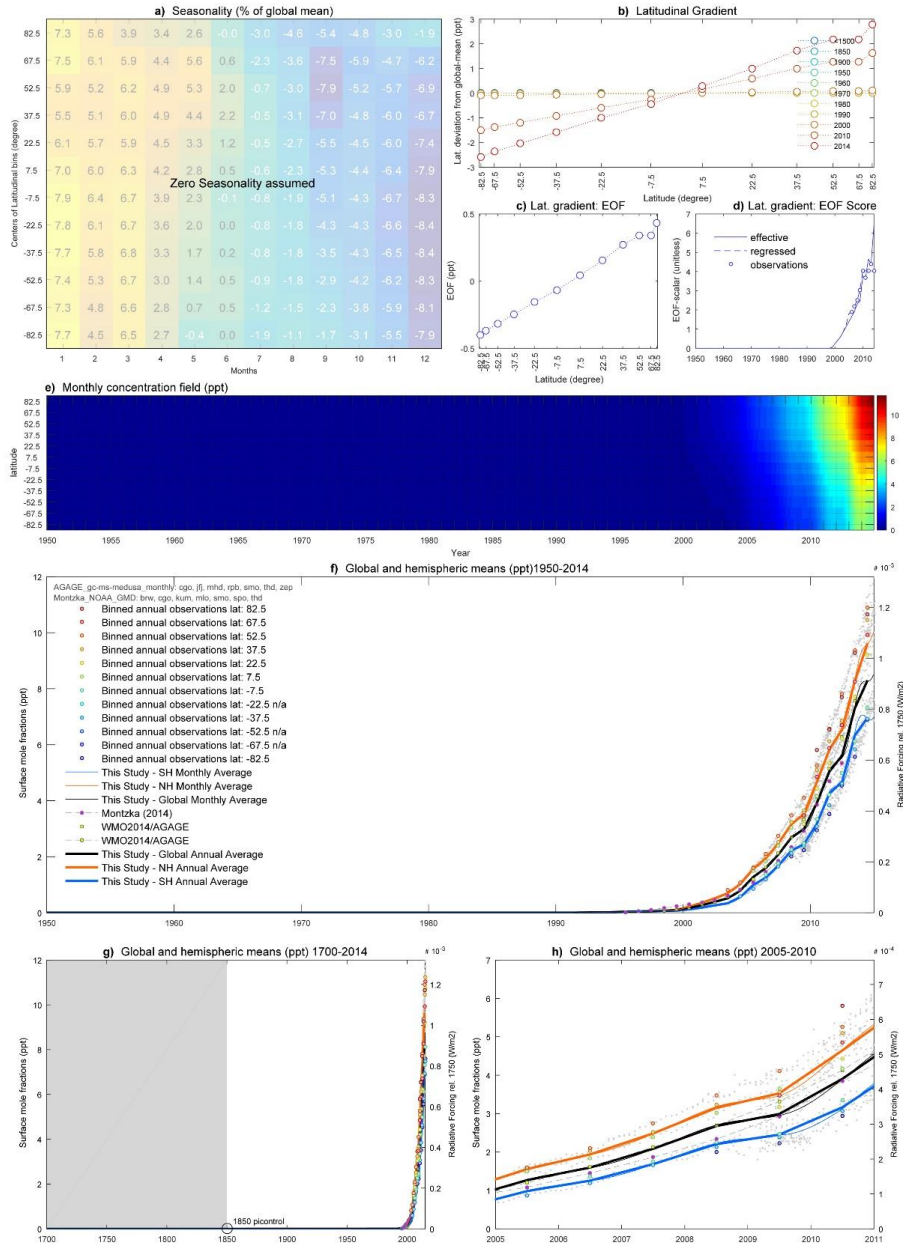
1349

1350   **Figure 50 - HFC-32 Factsheet**
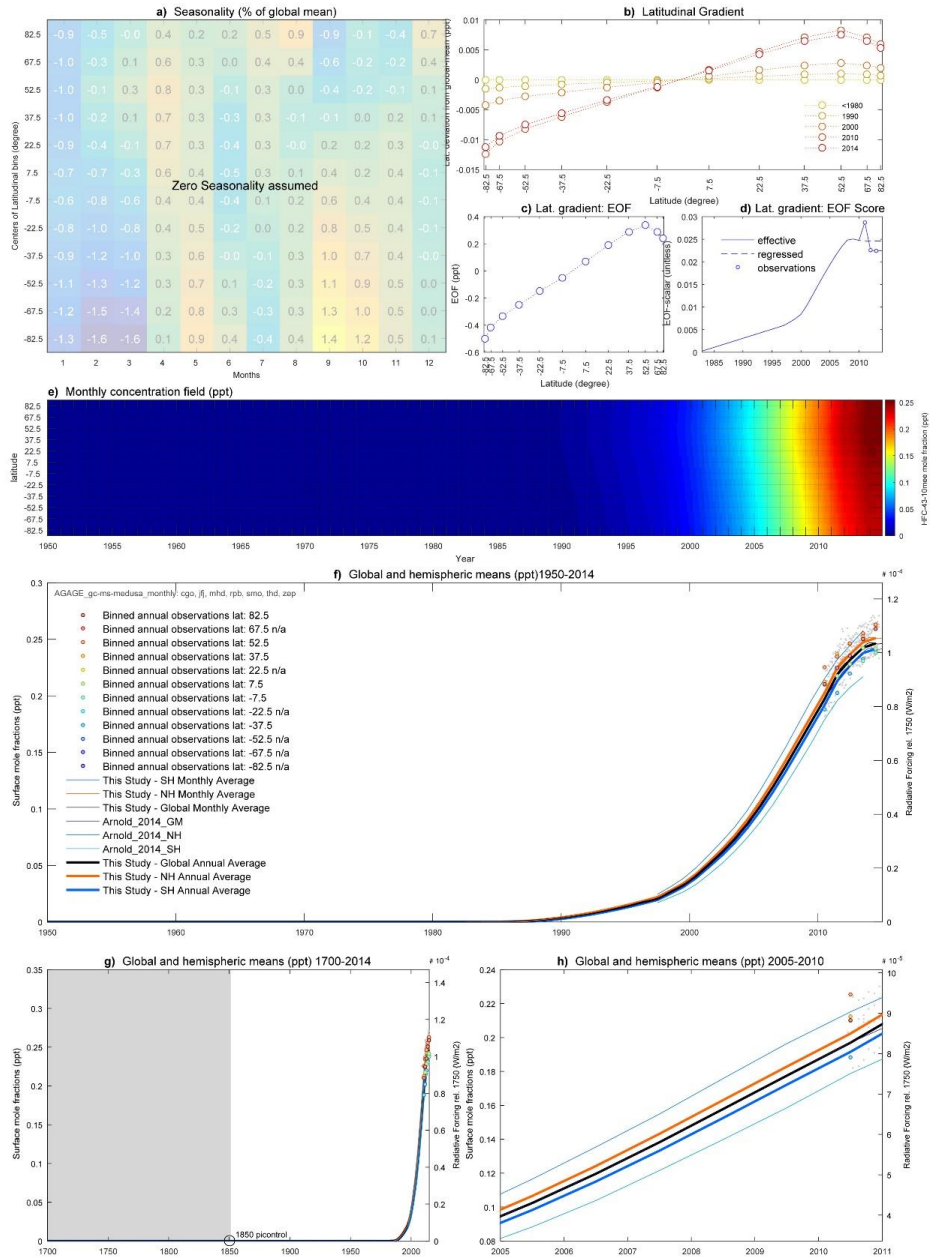
1351

1352   **Figure 51 - HFC-43-10-mee Factsheet**
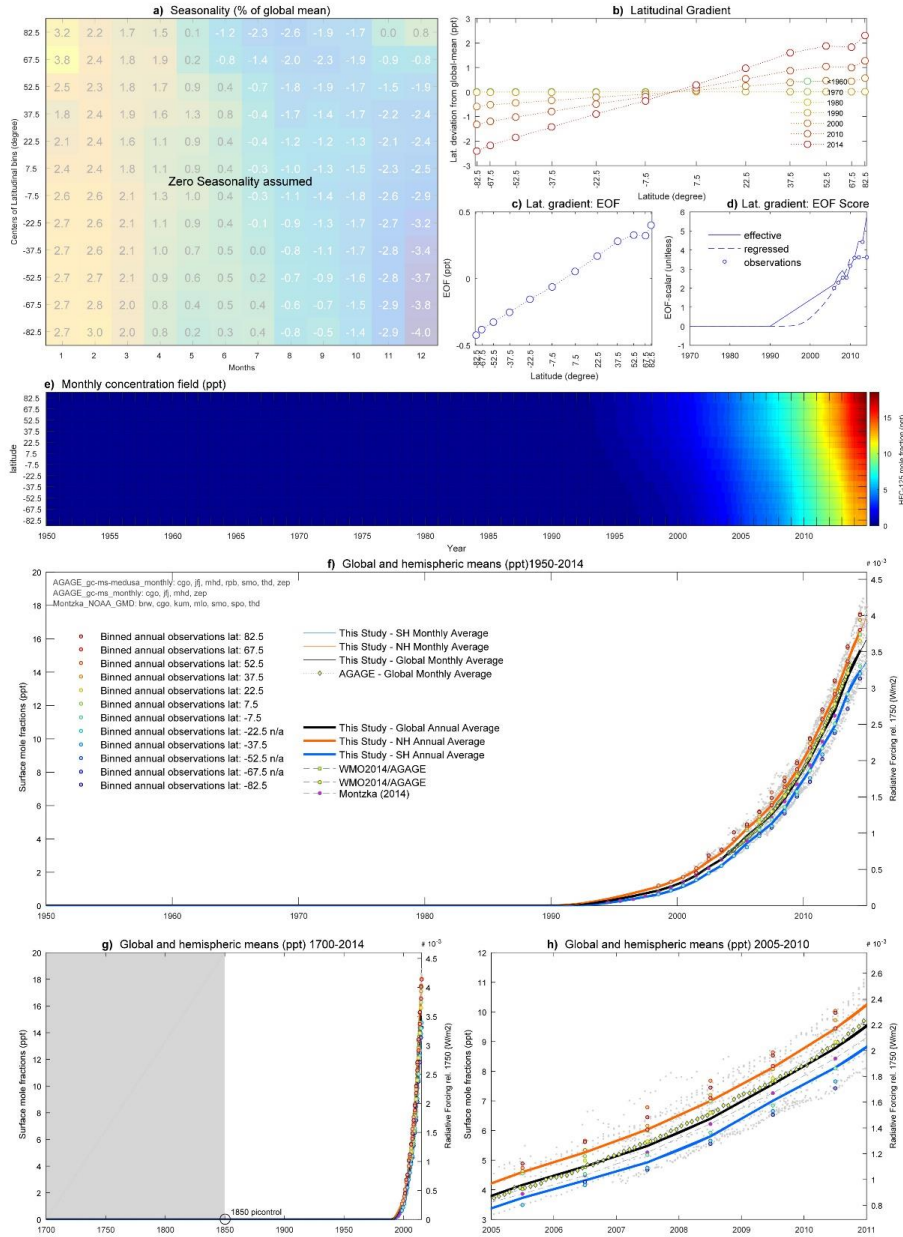
1353

1354   **Figure 52 - HFC-125 Factsheet**
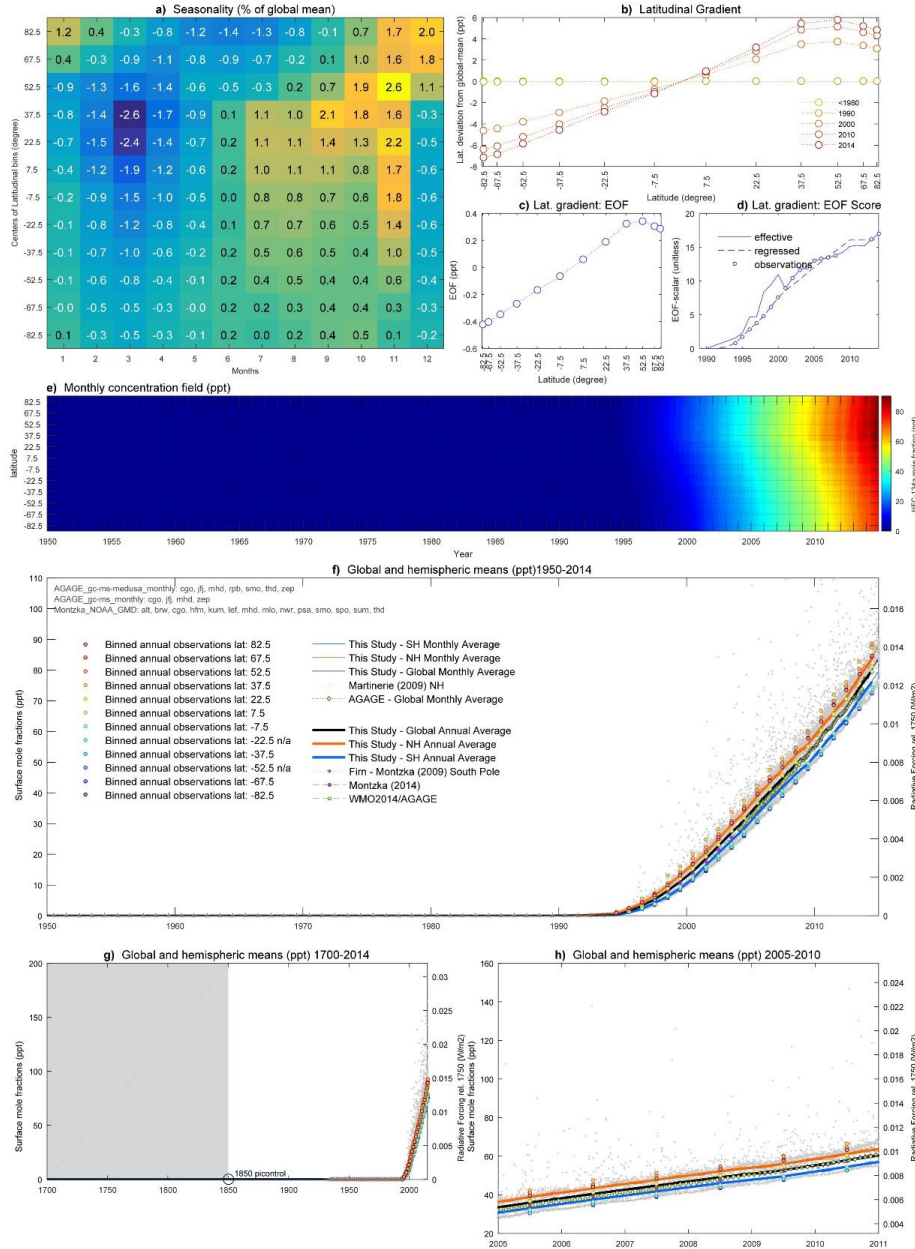
1355

1356   **Figure 53 - HFC-134a Factsheet**
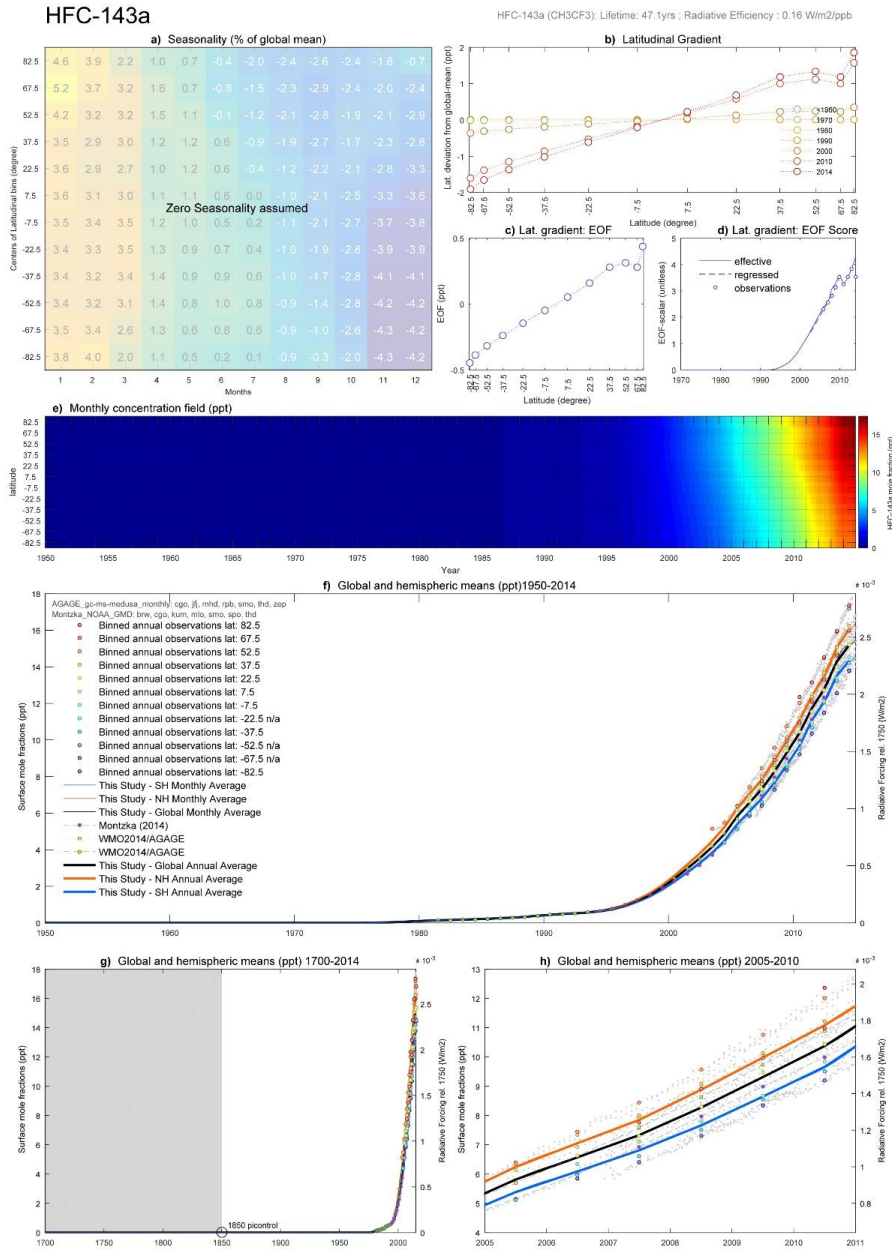
1357

1358 **Figure 54 - HFC-143a Factsheet**
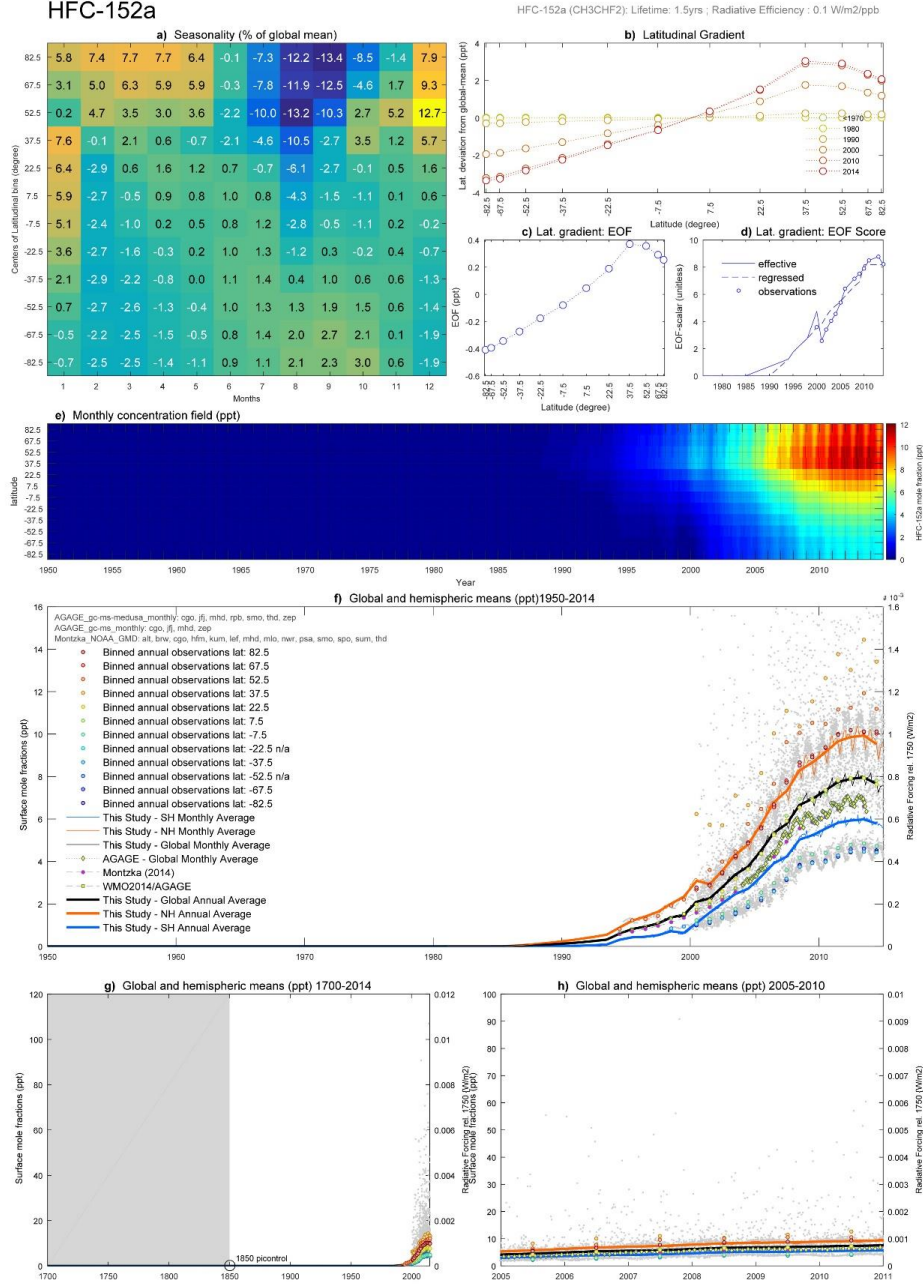
1359

1360   **Figure 55 - HFC-152a Factsheet**
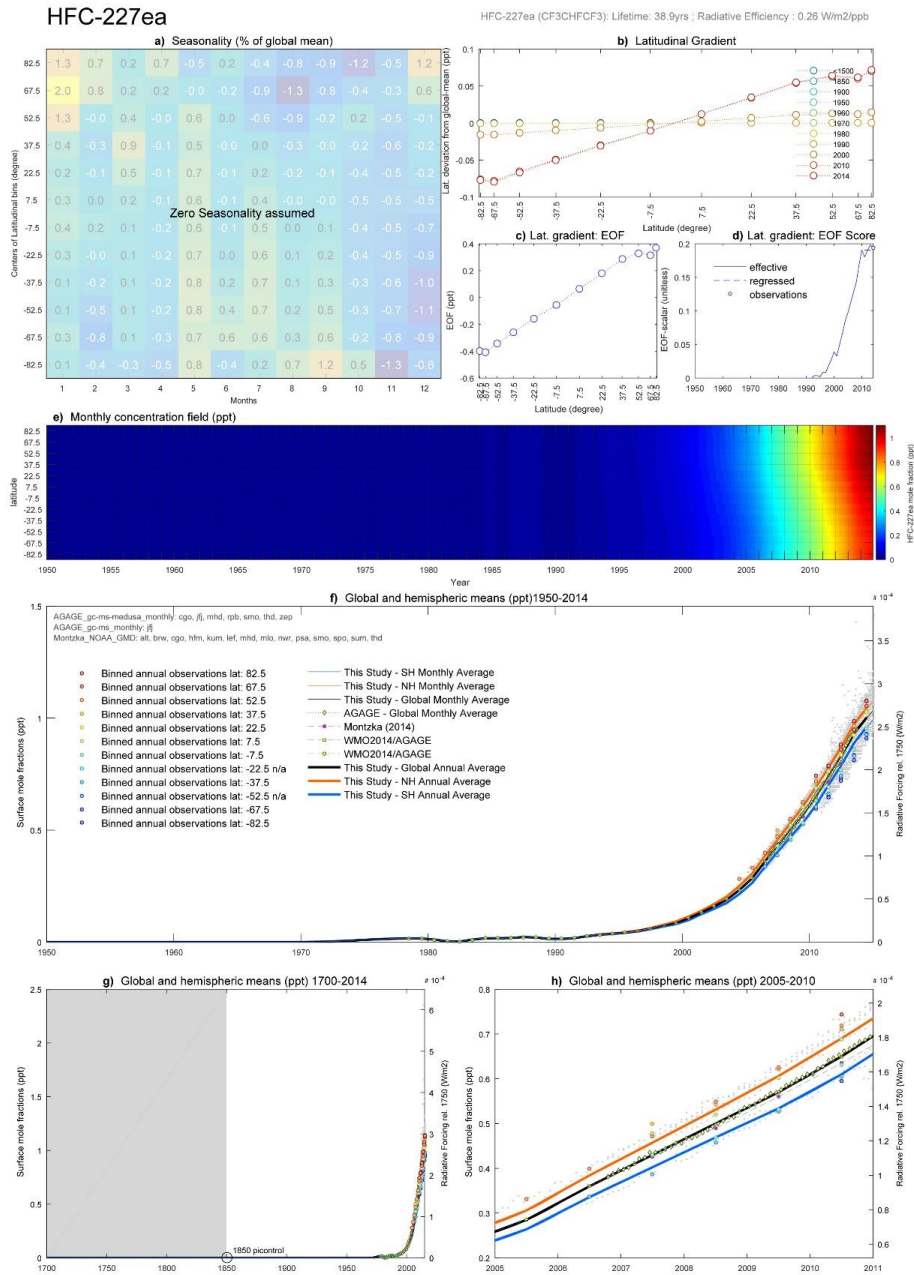
1361

1362   **Figure 56 - HFC-227ea Factsheet**
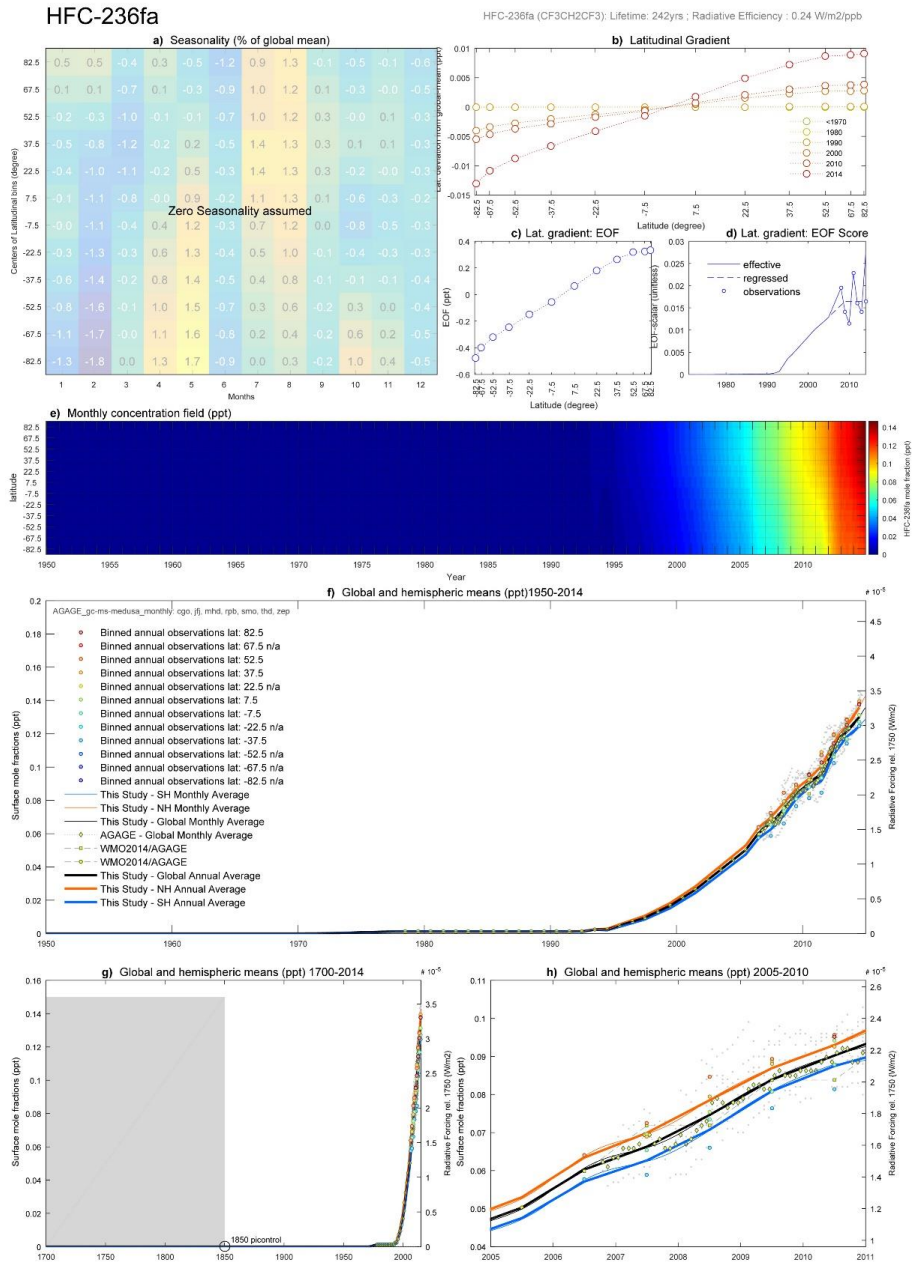
1363

1364   **Figure 57 - HFC-236fa Factsheet**
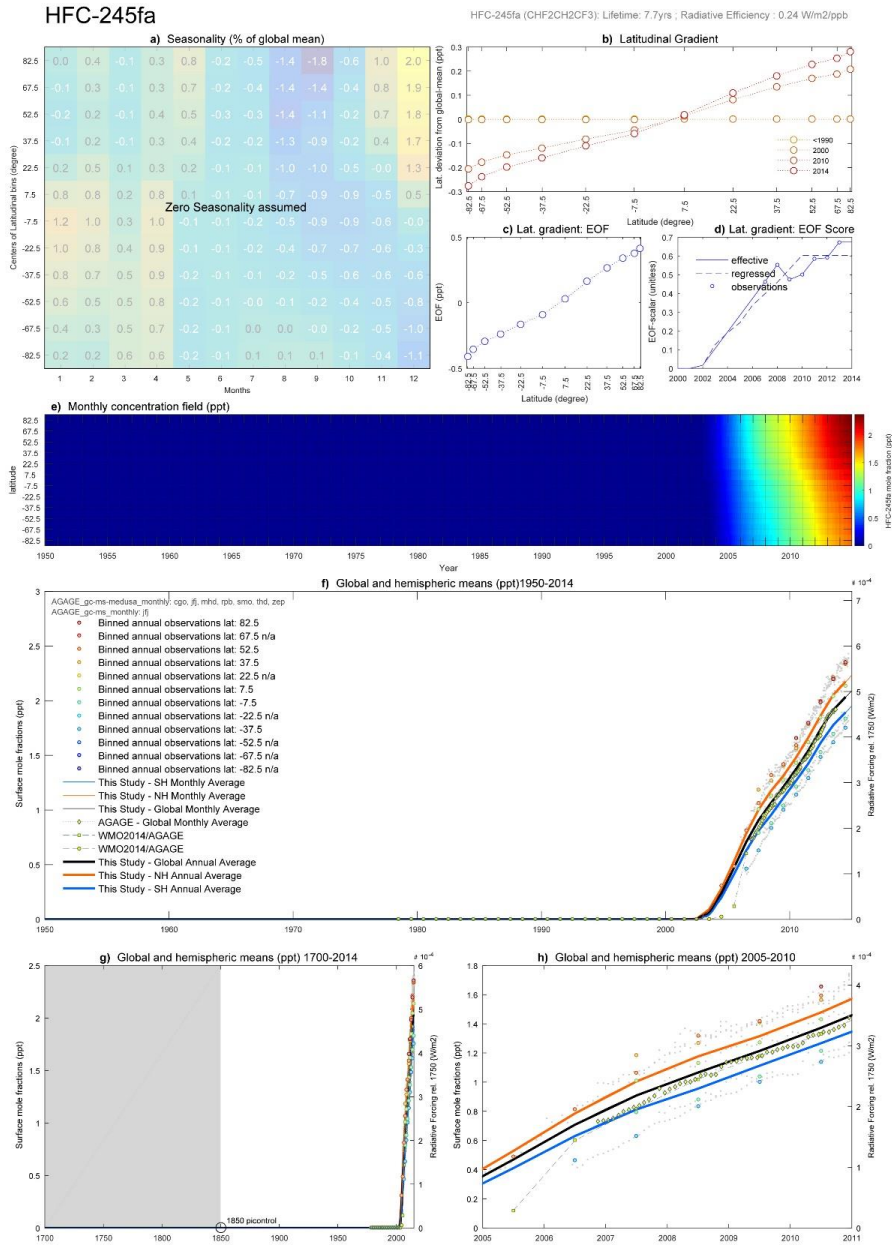
1365

1366   **Figure 58 - HFC-245fa Factsheet**
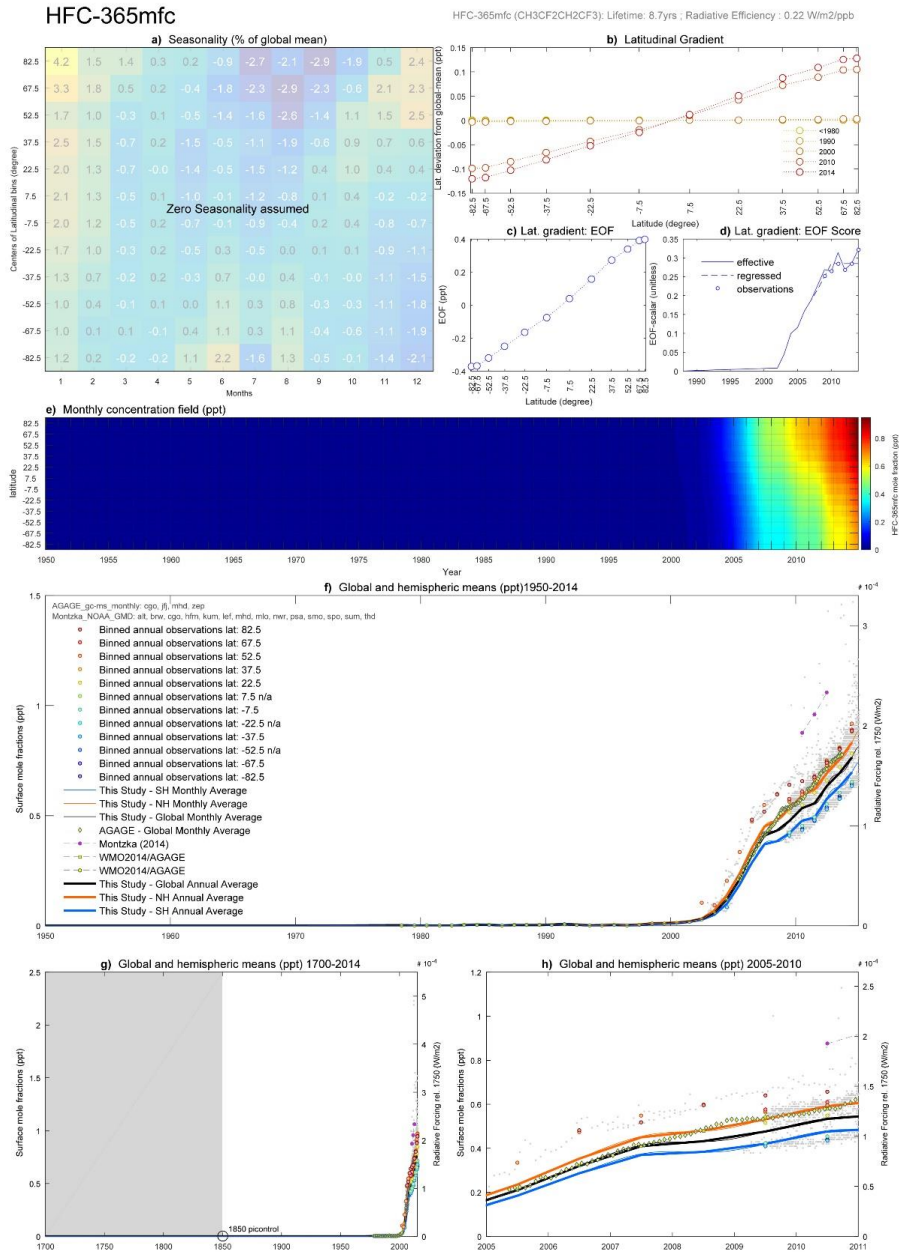
1367

1368   **Figure 59 - HFC-365mfc Factsheet.**
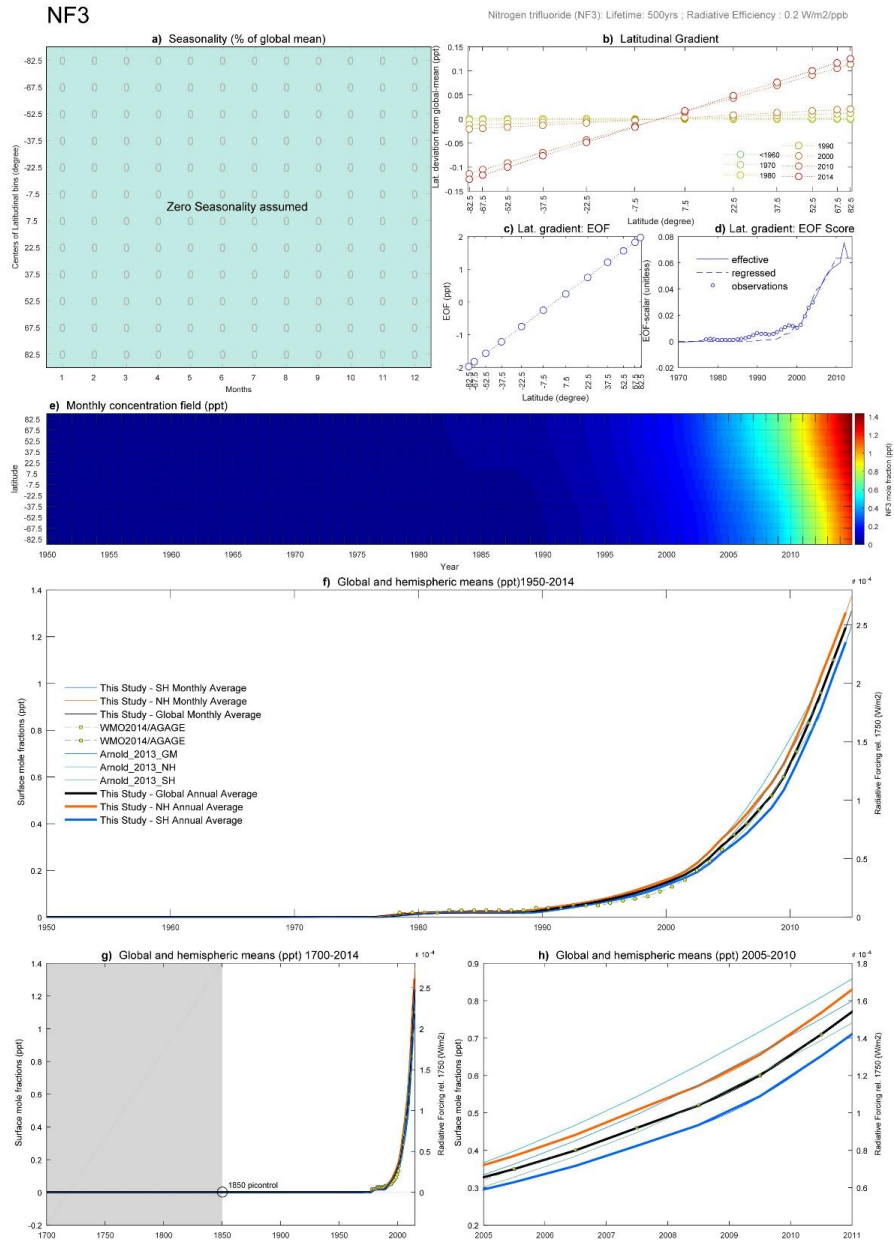
1369

1370   **Figure 60 - NF₃ Factsheet**
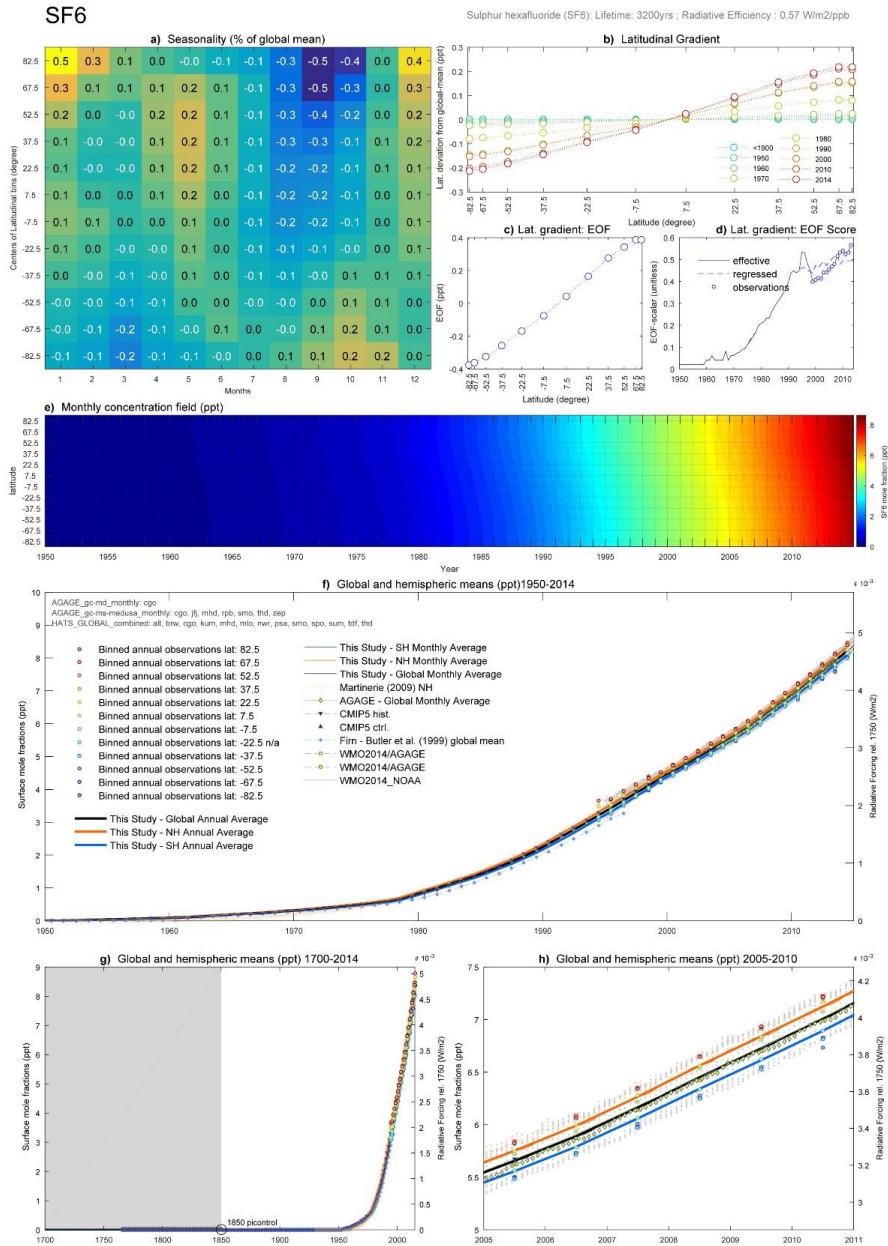
1371

1372   **Figure 61 - SF₆ Factsheet**
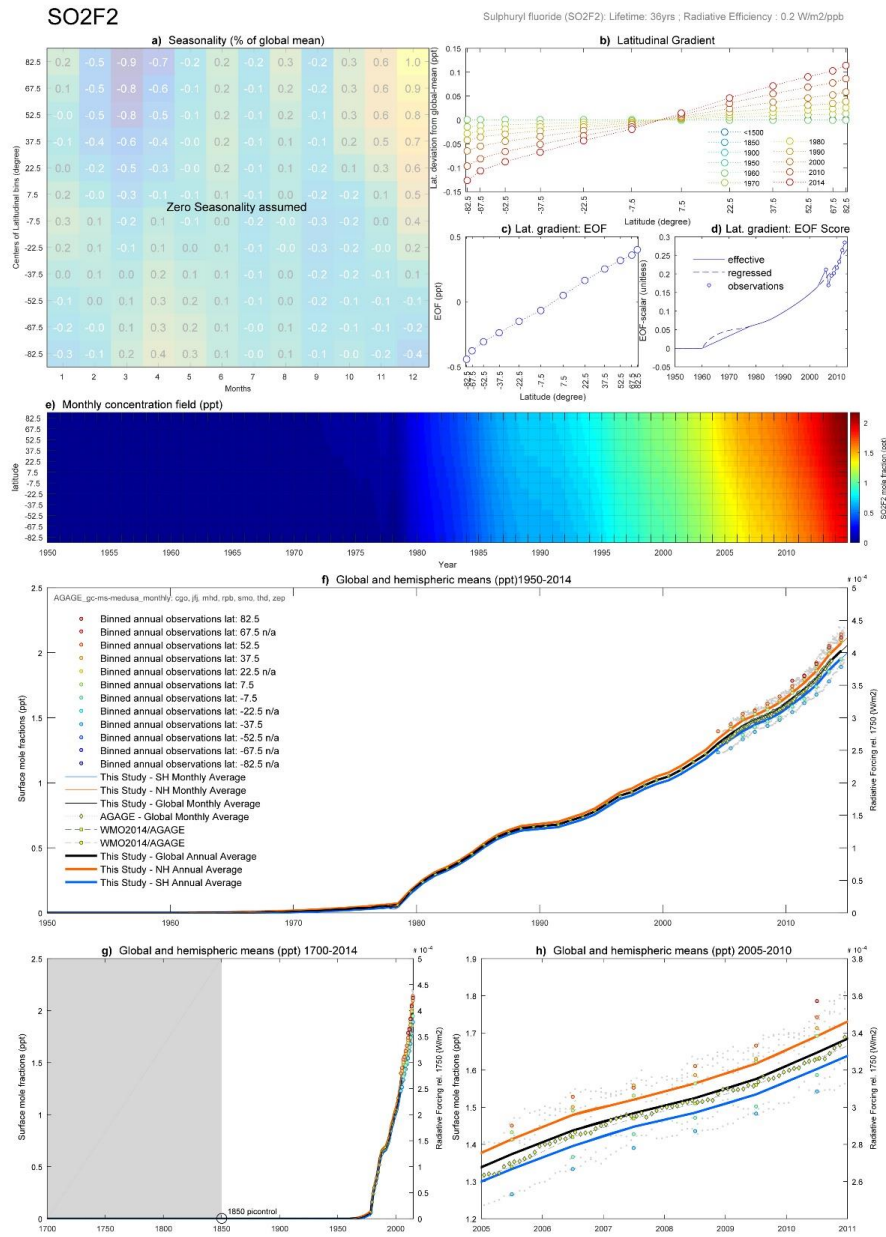
1373

1374   **Figure 62 - SO₂F₂ Factsheet**

1375

1376

1377

1378

1379

14   Appendix B: CMIP5 Analysis of CO_2 mixing ratio fields

1381

1382
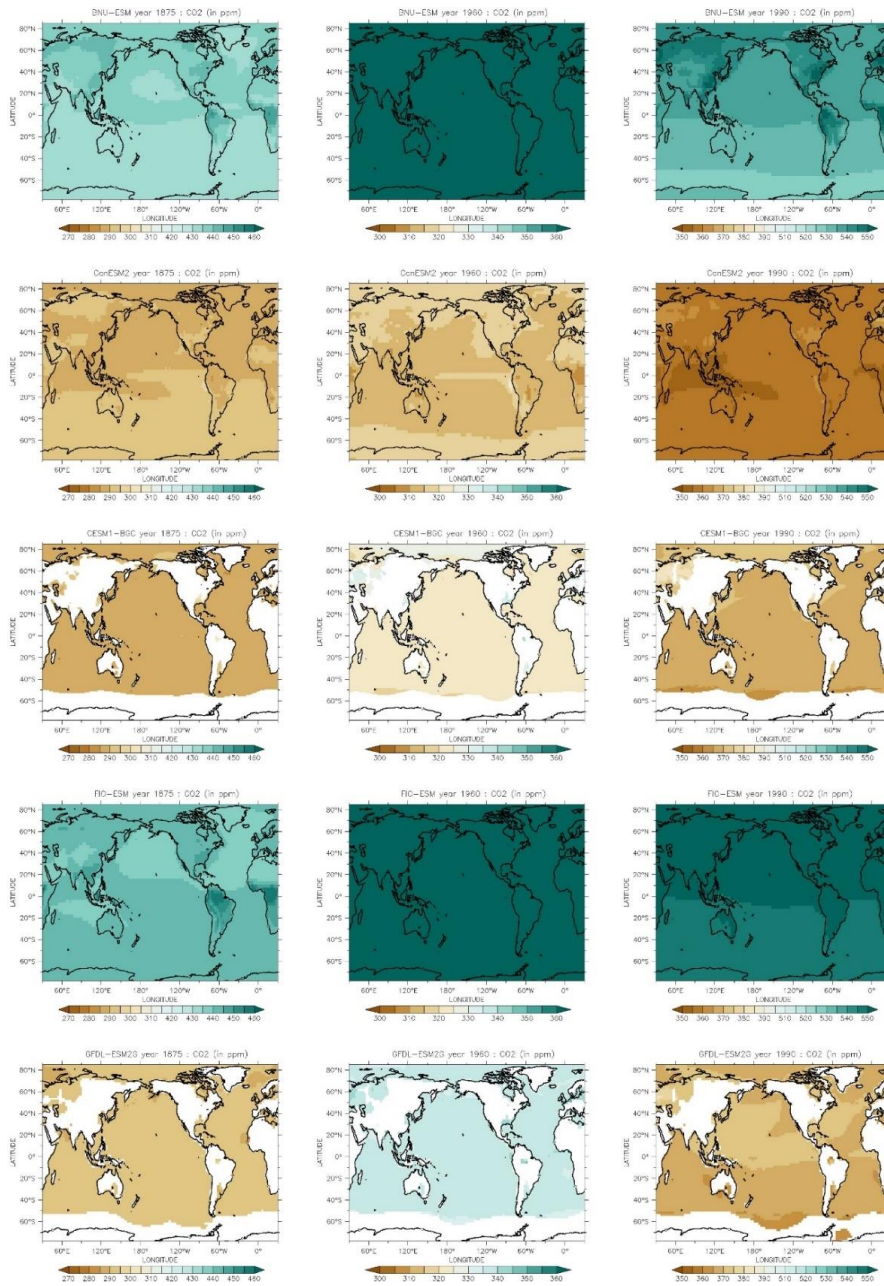
1383

Figure 63 – Annual average CO₂ mixing ratio fields diagnosed from CMIP5 ESM models for the years 1875 (left column), 1960 (middle column), and 1990 (right column). All models are on the same color scale, with coloring steps at 5 ppmv. 1990 annual average CO₂ mixing ratios are estimated in this study to be *354.07 ppmv and had been specified for CMIP5 with 353*.855 ppmv.
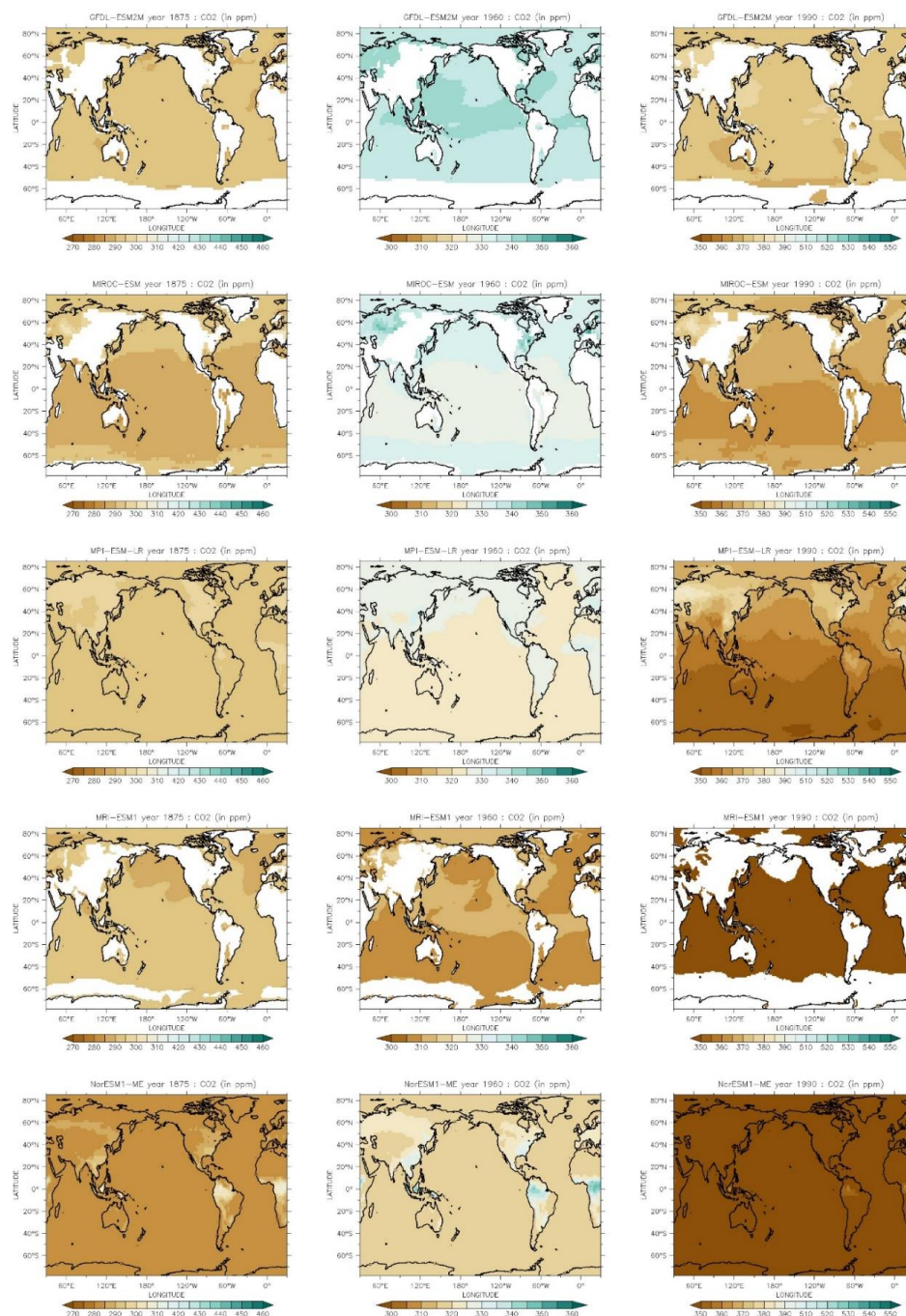
1387

Figure 64 – As Figure 63, but for a different set of five CMIP5 ESM models.

1389

15   References

Ahn, J., E. J. Brook, L. Mitchell, J. Rosen, J. R. McConnell, K. Taylor, D. Etheridge and M. Rubino (2012). "Atmospheric CO2 over the last 1000 years: A high-resolution record from the West Antarctic Ice Sheet (WAIS) Divide ice core." Global Biogeochemical Cycles **26**(2).

Anklin, M., J. Barnola, J. Schwander, B. Stauffer and D. Raynaud (1995). "Processes affecting the CO2 concentrations measured in Greenland ice." Tellus B **47**(4): 461-470.

Arnold, T., C. M. Harth, J. Mühle, A. J. Manning, P. K. Salameh, J. Kim, D. J. Ivy, L. P. Steele, V. V. Petrenko and J. P. Severinghaus (2013). "Nitrogen trifluoride global emissions estimated from updated atmospheric measurements." Proceedings of the National Academy of Sciences **110**(6): 2029-2034.

Arnold, T., D. J. Ivy, C. M. Harth, M. K. Vollmer, J. Mühle, P. K. Salameh, L. Paul Steele, P. B. Krummel, R. H. Wang and D. Young (2014). "HFC-43-10mee atmospheric abundances and global emission estimates." Geophysical Research Letters **41**(6): 2228-2235.

Aucott, M., A. McCulloch, T. Graedel, G. Kleiman, P. Midgley and Y. F. Li (1999). "Anthropogenic emissions of trichloromethane (chloroform, CHCl3) and chlorodifluoromethane (HCFC-22): Reactive chlorine emissions inventory." Journal of Geophysical Research: Atmospheres **104**(D7): 8405-8415.

Baker, D., R. Law, K. Gurney, P. Rayner, P. Peylin, A. Denning, P. Bousquet, L. Bruhwiler, Y. H. Chen and P. Ciais (2006). "TransCom 3 inversion intercomparison: Impact of transport model errors on the interannual variability of regional CO2 fluxes, 1988–2003." Global Biogeochemical Cycles **20**(1).

Barbante, C., J.-M. Barnola, S. Becagli, J. Beer, M. Bigler, C. Boutron, T. Blunier, E. Castellano, O. Cattani and J. Chappellaz (2006). "One-to-one coupling of glacial climate variability in Greenland and Antarctica." Nature **444**(7116): 195-198.

Barnola, J., M. Anklin, J. Porcheron, D. Raynaud, J. Schwander and B. Stauffer (1995). "CO2 evolution during the last millennium as recorded by Antarctic and Greenland ice." Tellus B **47**(1-2): 264-272.

Bauska, T. K., F. Joos, A. C. Mix, R. Roth, J. Ahn and E. J. Brook (2015). "Links between atmospheric carbon dioxide, the land carbon reservoir and climate over the past millennium." Nature Geoscience **8**(5): 383-387.

Bereiter, B., S. Eggleston, J. Schmitt, C. Nehrbass-Ahles, T. F. Stocker, H. Fischer, S. Kipfstuhl and J. Chappellaz (2015). "Revision of the EPICA Dome C CO2 record from 800 to 600 kyr before present." Geophysical Research Letters **42**(2): 542-549.

Boden, T. A., G. Marland and R. J. Andres (2013). Global, Regional, and National Fossil-Fuel CO2 Emissions. Oak Ridge, Tenn., USA. , Carbon Dioxide Information Analysis Center, Oak Ridge National Laboratory, U.S. Department of Energy. .

Buizert, C., P. Martinerie, V. V. Petrenko, J. P. Severinghaus, C. M. Trudinger, E. Witrant, J. L. Rosen, A. J. Orsi, M. Rubino, D. M. Etheridge, L. P. Steele, C. Hogan, J. C. Laube, W. T. Sturges, V. A. Levchenko, A. M. Smith, I. Levin, T. J. Conway, E. J. Dlugokencky, P. M. Lang, K. Kawamura, T. M. Jenk, J. W. C. White, T. Sowers, J. Schwander and T. Blunier (2012). "Gas transport in firn: multiple-tracer characterisation and model intercomparison for NEEM, Northern Greenland." Atmos. Chem. Phys. **12**(9): 4259-4277.

Butler, J. H., M. Battle, M. L. Bender, S. A. Montzka, A. D. Clarke, E. S. Saltzman, C. M. Sucher, J. P. Severinghaus and J. W. Elkins (1999). "A record of atmospheric halocarbons during the twentieth century from polar firn air." Nature **399**(6738): 749-755.

Capron, E., A. Landais, B. Lemieux-Dudon, A. Schilt, V. Masson-Delmotte, D. Buiron, J. Chappellaz, D. Dahl-Jensen, S. Johnsen and M. Leuenberger (2010). "Synchronising EDML and NorthGRIP ice cores using δ 18 O of atmospheric oxygen (δ 18 O atm) and CH 4 measurements over MIS5 (80–123 kyr)." Quaternary Science Reviews **29**(1): 222-234.

Conway, T. J., P. Tans, L. S. Waterman, K. W. Thoning, K. A. Masarie and R. H. Gammon (1988). "Atmospheric carbon dioxide measurements in the remote global troposphere, 1981–1984." Tellus B **40B**(2): 81-115.

Conway, T. J., P. P. Tans, L. S. Waterman, K. W. Thoning, D. R. Kitzis, K. A. Masarie and N. Zhang (1994). "Evidence for interannual variability of the carbon cycle from the National Oceanic and Atmospheric Administration/Climate Monitoring and Diagnostics Laboratory Global Air Sampling Network." Journal of Geophysical Research: Atmospheres **99**(D11): 22831-22855.

Cooperative Global Atmospheric Data Integration Project (2013). Multi-laboratory compilation of synchronized and gap-filled atmospheric carbon dioxide records for the period 1979-2012 (obspack_co2_1_GLOBALVIEW-CO2_2013_v1.0.4_2013-12-23). C. NOAA Global Monitoring Division: Boulder, U.S.A.

Cox, M., G. Sturrock, P. Fraser, S. Siems, P. Krummel and S. O'doherty (2003). "Regional sources of methyl chloride, chloroform and dichloromethane identified from AGAGE observations at Cape Grim, Tasmania, 1998–2000." Journal of atmospheric chemistry **45**(1): 79-99.

Cunnold, D., L. Steele, P. Fraser, P. Simmonds, R. Prinn, R. Weiss, L. Porter, S. O'Doherty, R. Langenfelds and P. Krummel (2002). "In situ measurements of atmospheric methane at GAGE/AGAGE sites during 1985–2000 and resulting source inferences." Journal of Geophysical Research: Atmospheres **107**(D14).

Cunnold, D., R. Weiss, R. Prinn, D. Hartley, P. Simmonds, P. Fraser, B. Miller, F. Alyea and L. Porter (1997). "GAGE/AGAGE measurements indicating reductions in global emissions of CCl3F and CCl2F2 in 1992–1994." Journal of Geophysical Research: Atmospheres **102**(D1): 1259-1269.

Dahl-Jensen, D., M. Albert, A. Aldahan, N. Azuma, D. Balslev-Clausen, M. Baumgartner, A.-M. Berggren, M. Bigler, T. Binder and T. Blunier (2013). "Eemian interglacial reconstructed from a Greenland folded ice core." Nature **493**(7433): 489-494.

Denning, A. S., I. Y. Fung and D. Randall (1995). "Latitudinal gradient of atmospheric CO2 due to seasonal exchange with land biota." Nature **376**(6537): 240-243.

Denning, A. S., T. Takahashi and P. Friedlingstein (1999). "Can a strong atmospheric CO2 rectifier effect be reconciled with a "reasonable" carbon budget?" Tellus B **51**(2): 249-253.

Dlugokencky, E. J., L. Bruhwiler, J. W. C. White, L. K. Emmons, P. C. Novelli, S. A. Montzka, K. A. Masarie, P. M. Lang, A. M. Crotwell, J. B. Miller and L. V. Gatti (2009). "Observational constraints on recent increases in the atmospheric CH4 burden." Geophysical Research Letters **36**(18): n/a-n/a.

Dlugokencky, E. J., K. A. Masaire, P. M. Lang, P. P. Tans, L. P. Steele and E. G. Nisbet (1994a). "A dramatic decrease in the growth rate of atmospheric methane in the northern hemisphere during 1992." Geophysical Research Letters **21**(1): 45-48.

Dlugokencky, E. J., K. A. Masarie, P. M. Lang and P. P. Tans (1998). "Continuing decline in the growth rate of the atmospheric methane burden." Nature **393**(6684): 447-450.

Dlugokencky, E. J., R. C. Myers, P. M. Lang, K. A. Masarie, A. M. Crotwell, K. W. Thoning, B. D. Hall, J. W. Elkins and L. P. Steele (2005). "Conversion of NOAA atmospheric dry air CH4 mole fractions to a gravimetrically prepared standard scale." Journal of Geophysical Research: Atmospheres **110**(D18): n/a-n/a.

Dlugokencky, E. J., P.M. Lang, A.M. Crotwell, K.A. Masarie, and M.J. Crotwell (2015a). Atmospheric Methane Dry Air Mole Fractions from the NOAA ESRL Carbon Cycle Cooperative Global Air Sampling Network, 1983-2014. NOAA.

Dlugokencky, E. J., P.M. Lang, K.A. Masarie, A.M. Crotwell, M.J. Crotwell (2015b). Atmospheric Carbon Dioxide Dry Air Mole Fractions from the NOAA ESRL Carbon Cycle Cooperative Global Air Sampling Network, 1968-2014. NOAA.

Dlugokencky, E. J., L. P. Steele, P. M. Lang and K. A. Masarie (1994b). "The Growth-Rate and Distribution of Atmospheric Methane." Journal of Geophysical Research-Atmospheres **99**(D8): 17021-17043.

Dlugokencky, E. J., L. P. Steele, P. M. Lang and K. A. Masarie (1994c). "The growth rate and distribution of atmospheric methane." Journal of Geophysical Research: Atmospheres **99**(D8): 17021-17043.

Dlugokencky, E. J., B. P. Walter, K. A. Masarie, P. M. Lang and E. S. Kasischke (2001). "Measurements of an anomalous global methane increase during 1998." Geophysical Research Letters **28**(3): 499-502.

Enting, I. and J. Mansbridge (1989). "Seasonal sources and sinks of atmospheric CO 2 direct inversion of filtered data." Tellus B **41**(2).

Enting, I. and J. Mansbridge (1991). "Latitudinal distribution of sources and sinks of CO2: Results of an inversion study." Tellus B **43**(2): 156-170.

Enting, I., C. Trudinger and R. Francey (1995). "A synthesis inversion of the concentration and δ13 C of atmospheric CO2." Tellus B **47**(1-2): 35-52.

Enting, I. G. (1998). Green's function methods of tracer inversion, Wiley Online Library.

1488   Etheridge, D., L. P. Steele, R. Francey and R. Langenfelds (1998a). "Atmospheric methane between 1000 AD and
1489   present: Evidence of anthropogenic emissions and climatic variability." Journal of Geophysical Research:
1490   Atmospheres **103**(D13): 15979-15993.
1491   Etheridge, D. M., L. P. Steele, R. J. Francey and R. L. Langenfelds (1998b). "Atmospheric methane between 1000
1492   AD and present: Evidence of anthropogenic emissions and climatic variability." Journal of Geophysical Research-
1493   Atmospheres **103**(D13): 15979-15993.
1494   Etheridge, D. M., L. P. Steele, R. L. Langenfelds, R. J. Francey, J.-M. Barnola and V. I. Morgan. (1998c). "Historical
1495   CO2 record from the Law Dome DE08, DE08-2, and DSS ice cores."   Retrieved May, 2007, from
1496   ftp://ftp.ncdc.noaa.gov/pub/data/paleo/icecore/antarctica/law/law_co2.txt.
1497   Etheridge, D. M., L. P. Steele, R. L. Langenfelds, R. J. Francey, J. M. Barnola and V. I. Morgan (1996). "Natural and
1498   anthropogenic changes in atmospheric CO2 over the last 1000 years from air in Antarctic ice and firn." Journal of
1499   Geophysical Research-Atmospheres **101**(D2): 4115-4128.
1500   Eyring, V., S. Bony, G. A. Meehl, C. Senior, B. Stevens, R. J. Stouffer and K. E. Taylor (2015). "Overview of the
1501   Coupled Model Intercomparison Project Phase 6 (CMIP6) experimental design and organisation." Geosci. Model
1502   Dev. Discuss. **2015**: 10539-10583.
1503   Eyring, V., S. Bony, G. A. Meehl, C. A. Senior, B. Stevens, R. J. Stouffer and K. E. Taylor (2016). "Overview of the
1504   Coupled Model Intercomparison Project Phase 6 (CMIP6) experimental design and organization." Geosci. Model
1505   Dev. **9**(5): 1937-1958.
1506   Fluckiger, J., E. Monnin, B. Stauffer, J. Schwander, T. F. Stocker, J. Chappellaz, D. Raynaud and J. M. Barnola (2002).
1507   "High-resolution Holocene N2O ice core record and its relationship with CH4 and CO2." Global Biogeochemical
1508   Cycles **16**(1): -.
1509   Forkel, M., N. Carvalhais, C. Rödenbeck, R. Keeling, M. Heimann, K. Thonicke, S. Zaehle and M. Reichstein (2016).
1510   "Enhanced seasonal CO2 exchange caused by amplified plant productivity in northern ecosystems." Science:
1511   aac4971.
1512   Francey, R. J. and J. S. Frederiksen (2016). "The 2009–2010 step in atmospheric CO2 interhemispheric difference."
1513   Biogeosciences **13**(3): 873-885.
1514   Francey, R. J., C. M. Trudinger, M. van der Schoot, R. M. Law, P. B. Krummel, R. L. Langenfelds, L. Paul Steele, C. E.
1515   Allison, A. R. Stavert, R. J. Andres and C. Rodenbeck (2013). "Atmospheric verification of anthropogenic CO2
1516   emission trends." Nature Clim. Change **3**(5): 520-524.
1517   Fraser, P., D. Cunnold, F. Alyea, R. Weiss, R. Prinn, P. Simmonds, B. Miller and R. Langenfelds (1996). "Lifetime and
1518   emission estimates of 1, 1, 2-trichlorotrifluorethane (CFC-113) from daily global background observations June
1519   1982–June 1994." Journal of Geophysical Research: Atmospheres **101**(D7): 12585-12599.
1520   Fung, I., J. John, J. Lerner, E. Matthews, M. Prather, L. Steele and P. Fraser (1991). "Three-dimensional model
1521   synthesis of the global methane cycle." Journal of Geophysical Research: Atmospheres **96**(D7): 13033-13065.
1522   Ghosh, A., P. K. Patra, K. Ishijima, T. Umezawa, A. Ito, D. M. Etheridge, S. Sugawara, K. Kawamura, J. B. Miller, E.
1523   J. Dlugokencky, P. B. Krummel, P. J. Fraser, L. P. Steele, R. L. Langenfelds, C. M. Trudinger, J. W. C. White, B.
1524   Vaughn, T. Saeki, S. Aoki and T. Nakazawa (2015). "Variations in global methane sources and sinks during 1910–
1525   2010." Atmos. Chem. Phys. **15**(5): 2595-2612.
1526   Graven, H. D., R. F. Keeling, S. C. Piper, P. K. Patra, B. B. Stephens, S. C. Wofsy, L. R. Welp, C. Sweeney, P. P. Tans,
1527   J. J. Kelley, B. C. Daube, E. A. Kort, G. W. Santoni and J. D. Bent (2013). "Enhanced Seasonal Exchange of CO2 by
1528   Northern Ecosystems Since 1960." Science **341**(6150): 1085-1089.
1529   Gray, J. M., S. Frolking, E. A. Kort, D. K. Ray, C. J. Kucharik, N. Ramankutty and M. A. Friedl (2014). "Direct human
1530   influence on atmospheric CO2 seasonality from increased cropland productivity." Nature **515**(7527): 398-401.
1531   Gurney, K. R., R. M. Law, A. S. Denning, P. J. Rayner, D. Baker, P. Bousquet, L. Bruhwiler, Y.-H. Chen, P. Ciais and
1532   S. Fan (2002). "Towards robust regional estimates of CO2 sources and sinks using atmospheric transport models."
1533   Nature **415**(6872): 626-630.
1534   Gurney, K. R., R. M. Law, A. S. Denning, P. J. Rayner, D. Baker, P. Bousquet, L. Bruhwiler, Y. H. CHEN, P. Ciais and
1535   S. Fan (2003). "TransCom 3 CO2 inversion intercomparison: 1. Annual mean control results and sensitivity to
1536   transport and prior flux information." Tellus B **55**(2): 555-579.

Gurney, K. R., R. M. Law, A. S. Denning, P. J. Rayner, B. C. Pak, D. Baker, P. Bousquet, L. Bruhwiler, Y. H. Chen and P. Ciais (2004). "Transcom 3 inversion intercomparison: Model mean results for the estimation of seasonal carbon sources and sinks." Global Biogeochemical Cycles **18**(1).

Gütschow, J., M. L. Jeffery, R. Gieseke, R. Gebel, D. Stevens, M. Krapp and M. Rocha (2016). "The PRIMAP-hist national historical emissions time series." Earth Syst. Sci. Data Discuss. **2016**: 1-44.

Hurrell, J. W., M. M. Holland, P. R. Gent, S. Ghan, J. E. Kay, P. J. Kushner, J.-F. Lamarque, W. G. Large, D. Lawrence, K. Lindsay, W. H. Lipscomb, M. C. Long, N. Mahowald, D. R. Marsh, R. B. Neale, P. Rasch, S. Vavrus, M. Vertenstein, D. Bader, W. D. Collins, J. J. Hack, J. Kiehl and S. Marshall (2013). "The Community Earth System Model: A Framework for Collaborative Research." Bulletin of the American Meteorological Society **94**(9): 1339-1360.

Hurtt, G., L. P. Chini, S. Frolking, R. Betts, J. Feddema, G. Fischer, J. Fisk, K. Hibbard, R. Houghton and A. Janetos (2011). "Harmonization of land-use scenarios for the period 1500–2100: 600 years of global gridded annual land-use transitions, wood harvest, and resulting secondary lands." Climatic Change **109**(1-2): 117-161.

IPCC, Ed. (2013). Climate Change 2013: The Physical Science Basis. Contribution of Working Group I to the Fifth Assessment Report of the Intergovernmental Panel on Climate Change. Cambridge, United Kingdom and New York, NY, USA, Cambridge University Press.

Ivy, D. J., M. Rigby, M. Baasandorj, J. B. Burkholder and R. G. Prinn (2012). "Global emission estimates and radiative impact of C_4F_{10}, C_5F_{12}, C_6F_{14}, C_7F_{16} and C_8F_{18}." Atmos. Chem. Phys. **12**(16): 7635-7645.

Jones, C. D. and P. M. Cox (2001). "Modeling the volcanic signal in the atmospheric CO2 record." Global Biogeochemical Cycles **15**(2): 453-465.

Keeling, C. D., R. B. Bacastow, A. E. Bainbridge, C. A. Ekdahl, P. R. Guenther, L. S. Waterman and J. F. Chin (1976). "Atmospheric carbon dioxide variations at Mauna Loa observatory, Hawaii." Tellus **28**(6): 538-551.

Keeling, C. D., R. B. Bacastow, A. Carter, S. C. Piper, T. P. Whorf, M. Heimann, W. G. Mook and H. Roeloffzen (1989a). "A three-dimensional model of atmospheric CO2 transport based on observed winds: 1. Analysis of observational data." Aspects of climate variability in the Pacific and the Western Americas: 165-236.

Keeling, C. D., S. C. Piper and M. Heimann (1989b). "A three-dimensional model of atmospheric CO2 transport based on observed winds: 4. Mean annual gradients and interannual variations." Aspects of climate variability in the Pacific and the Western Americas: 305-363.

Keeling, C. D., S. C. Piper, T. P. Whorf and R. F. Keeling (2011). "Evolution of natural and anthropogenic fluxes of atmospheric CO2 from 1957 to 2003." Tellus B **63**(1): 1-22.

Kohlmaier, G. H., E. O. Siré, A. Janecek, C. D. Keeling, S. C. Piper and R. Revelle (1989). "Modelling the seasonal contribution of a CO2 fertilization effect of the terrestrial vegetation to the amplitude increase in atmospheric CO2 at Mauna Loa Observatory." Tellus B **41**(5): 487-510.

Komhyr, W. D., R. H. Gammon, T. B. Harris, L. S. Waterman, T. J. Conway, W. R. Taylor and K. W. Thoning (1985). "Global atmospheric CO2 distribution and variations from 1968–1982 NOAA/GMCC CO2 flask sample data." Journal of Geophysical Research: Atmospheres **90**(D3): 5567-5596.

Komhyr, W. D., L. S. Waterman and W. R. Taylor (1983). "Semiautomatic nondispersive infrared analyzer apparatus for CO2 air sample analyses." Journal of Geophysical Research: Oceans **88**(C2): 1315-1322.

Koppmann, R., F. Johnen, C. Plass-Dülmer and J. Rudolph (1993). "Distribution of methylchloride, dichloromethane, trichloroethene and tetrachloroethene over the North and South Atlantic." Journal of Geophysical Research: Atmospheres **98**(D11): 20517-20526.

Lang, P. M., L.P. Steele, and R.C. Martin (1990a). "Atmospheric methane data for the period 1986-1988 from the NOAA/CMDL global cooperative flask sampling network." NOAA Technical Memorandum ERL CMDL-2.

Lang, P. M., L.P. Steele, L.S. Waterman, R.C. Martin, K.A. Masarie, and E.J. Dlugokencky (1992). "NOAA/CMDL Atmospheric methane data for the period 1983-1990 from shipboard flask sampling." NOAA Technical Memorandum ERL CMDL-4.

Lang, P. M., L.P. Steele, R.C. Martin, and K.A. Masarie (1990b). "Atmospheric methane data for the period 1983-1985 from the NOAA/GMCC global cooperative flask sampling network." NOAA Technical Memorandum ERL CMDL-1.

Lewis, D. (2016). "Australian climate job cuts leave hole in Southern Hemisphere research." Nature.

Loulergue, L., A. Schilt, R. Spahni, V. Masson-Delmotte, T. Blunier, B. Lemieux, J.-M. Barnola, D. Raynaud, T. F. Stocker and J. Chappellaz (2008). "Orbital and millennial-scale features of atmospheric CH4 over the past 800,000 years." Nature **453**(7193): 383-386.

Lüthi, D., M. Le Floch, B. Bereiter, T. Blunier, J.-M. Barnola, U. Siegenthaler, D. Raynaud, J. Jouzel, H. Fischer and K. Kawamura (2008). "High-resolution carbon dioxide concentration record 650,000–800,000 years before present." Nature **453**(7193): 379-382.

MacFarling Meure, C., D. Etheridge, C. Trudinger, P. Steele, R. Langenfelds, T. Van Ommen, A. Smith and J. Elkins (2006). "Law Dome CO2, CH4 and N2O ice core records extended to 2000 years BP." Geophysical Research Letters **33**(14).

Martinerie, P., E. Nourtier-Mazauric, J. M. Barnola, W. T. Sturges, D. R. Worton, E. Atlas, L. K. Gohar, K. P. Shine and G. P. Brasseur (2009). "Long-lived halocarbon trends and budgets from atmospheric chemistry modelling constrained with measurements in polar firn." Atmos. Chem. Phys. **9**(12): 3911-3934.

Masarie, K. A. and P. P. Tans (1995). "Extension and integration of atmospheric carbon dioxide data into a globally consistent measurement record." Journal of Geophysical Research: Atmospheres **100**(D6): 11593-11610.

Matthes, K., B. Funke, M. E. Anderson, L. Barnard, J. Beer, P. Charbonneau, M. A. Clilverd, T. Dudok de Wit, M. Haberreiter, A. Hendry, C. H. Jackman, M. Kretschmar, T. Kruschke, M. Kunze, U. Langematz, D. R. Marsh, A. Maycock, S. Misios, C. J. Rodger, A. A. Scaife, A. Seppälä, M. Shangguan, M. Sinnhuber, K. Tourpali, I. Usoskin, M. van de Kamp, P. T. Verronen and S. Versick (2016). "Solar Forcing for CMIP6 (v3.1)." Geosci. Model Dev. Discuss. **2016**: 1-82.

Meehl, G. A., C. Covey, B. McAvaney, M. Latif and R. J. Stouffer (2005). "Overview of coupled model intercomparison project." Bulletin of the American Meteorological Society (BAMS) **86**(89).

Meinshausen, M., S. Smith, K. Calvin, J. Daniel, M. Kainuma, J. F. Lamarque, K. Matsumoto, S. Montzka, S. Raper, K. Riahi, A. Thomson, G. Velders and D. P. van Vuuren (2011a). "The RCP greenhouse gas concentrations and their extensions from 1765 to 2300." Climatic Change **109**(1): 213-241.

Meinshausen, M., S. J. Smith, K. Calvin, J. S. Daniel, M. Kainuma, J. Lamarque, K. Matsumoto, S. Montzka, S. Raper and K. Riahi (2011b). "The RCP greenhouse gas concentrations and their extensions from 1765 to 2300." Climatic Change **109**(1-2): 213-241.

Miller, B., J. Huang, R. Weiss, R. Prinn and P. Fraser (1998). "Atmospheric trend and lifetime of chlorodifluoromethane (HCFC-22) and the global tropospheric OH concentration." Journal of Geophysical Research: Atmospheres **103**(D11): 13237-13248.

Mitchell, L., E. Brook, J. E. Lee, C. Buizert and T. Sowers (2013). "Constraints on the Late Holocene anthropogenic contribution to the atmospheric methane budget." Science **342**(6161): 964-966.

Montzka, S., J. Butler, B. Hall, D. Mondeel and J. Elkins (2003). "A decline in tropospheric organic bromine." Geophysical Research Letters **30**(15).

Montzka, S., L. Kuijpers, M. Battle, M. Aydin, K. Verhulst, E. Saltzman and D. Fahey (2010). "Recent increases in global HFC-23 emissions." Geophysical Research Letters **37**(2).

Montzka, S., M. McFarland, S. Andersen, B. Miller, D. Fahey, B. Hall, L. Hu, C. Siso and J. Elkins (2014). "Recent trends in global emissions of hydrochlorofluorocarbons and hydrofluorocarbons: Reflecting on the 2007 adjustments to the Montreal Protocol." The Journal of Physical Chemistry A **119**(19): 4439-4449.

Montzka, S. A., J. H. Butler, J. W. Elkins, T. M. Thompson, A. D. Clarke and L. T. Lock (1999). "Present and future trends in the atmospheric burden of ozone-depleting halogens." Nature **398**(6729): 690-694.

Montzka, S. A., E. J. Dlugokencky and J. H. Butler (2011). "Non-CO2 greenhouse gases and climate change." Nature **476**(7358): 43-50.

Mühle, J., A. Ganesan, B. Miller, P. Salameh, C. Harth, B. Greally, M. Rigby, L. Porter, L. Steele and C. Trudinger (2010a). "Perfluorocarbons in the global atmosphere: tetrafluoromethane, hexafluoroethane, and octafluoropropane." Atmospheric Chemistry and Physics **10**(11): 5145-5164.

Mühle, J., A. L. Ganesan, B. R. Miller, P. K. Salameh, C. M. Harth, B. R. Greally, M. Rigby, L. W. Porter, L. P. Steele, C. M. Trudinger, P. B. Krummel, S. O'Doherty, P. J. Fraser, P. G. Simmonds, R. G. Prinn and R. F. Weiss (2010b). "Perfluorocarbons in the global atmosphere: tetrafluoromethane, hexafluoroethane, and octafluoropropane." Atmos. Chem. Phys. **10**(11): 5145-5164.

Mühle, J., J. Huang, R. Weiss, R. Prinn, B. Miller, P. Salameh, C. Harth, P. Fraser, L. Porter and B. Greally (2009). "Sulfuryl fluoride in the global atmosphere." Journal of Geophysical Research: Atmospheres **114**(D5).

NOAA (2013). Cooperative Global Atmospheric Data Integration Project: Multi-laboratory compilation of synchronized and gap-filled atmospheric carbon dioxide records for the period 1979-2012 (obspack_co2_1_GLOBALVIEW-CO2_2013_v1.0.4_2013-12-23). C. NOAA Global Monitoring Division: Boulder, U.S.A.

NOAA ESRL GMD (2014a). Atmospheric Carbon Dioxide Dry Air Mole Fractions from quasi-continuous measurements at American Samoa. D. R. K. K.W. Thoning, and A. Crotwell. National Oceanic and Atmospheric Administration (NOAA), Earth System Research Laboratory (ESRL), Global Monitoring Division (GMD): Boulder, Colorado, USA.

NOAA ESRL GMD (2014b). Atmospheric Carbon Dioxide Dry Air Mole Fractions from quasi-continuous measurements at Barrow, Alaska. D. R. K. K.W. Thoning, and A. Crotwell. National Oceanic and Atmospheric Administration (NOAA), Earth System Research Laboratory (ESRL), Global Monitoring Division (GMD): Boulder, Colorado, USA.

NOAA ESRL GMD (2014c). Atmospheric Carbon Dioxide Dry Air Mole Fractions from quasi-continuous measurements at Mauna Loa, Hawaii. D. R. K. K.W. Thoning, and A. Crotwell. National Oceanic and Atmospheric Administration (NOAA), Earth System Research Laboratory (ESRL), Global Monitoring Division (GMD): Boulder, Colorado, USA.

O'Doherty, S., D. Cunnold, A. Manning, B. Miller, R. Wang, P. Krummel, P. Fraser, P. Simmonds, A. McCulloch and R. Weiss (2004). "Rapid growth of hydrofluorocarbon 134a and hydrochlorofluorocarbons 141b, 142b, and 22 from advanced global atmospheric gases experiment (AGAGE) observations at Cape Grim, Tasmania, and Mace Head, Ireland." Journal of Geophysical Research: Atmospheres **109**(D6).

O'Doherty, S., P. Simmonds, D. Cunnold, H. Wang, G. Sturrock, P. Fraser, D. Ryall, R. Derwent, R. Weiss and P. Salameh (2001). "In situ chloroform measurements at Advanced Global Atmospheric Gases Experiment atmospheric research stations from 1994 to 1998." Journal of Geophysical Research: Atmospheres **106**(D17): 20429-20444.

O'Neill, B. C., C. Tebaldi, D. van Vuuren, V. Eyring, P. Friedlingstein, G. Hurtt, R. Knutti, E. Kriegler, J. F. Lamarque, J. Lowe, J. Meehl, R. Moss, K. Riahi and B. M. Sanderson (2016). "The Scenario Model Intercomparison Project (ScenarioMIP) for CMIP6." Geosci. Model Dev. Discuss. **2016**: 1-35.

Olsen, S. C. and J. T. Randerson (2004). "Differences between surface and column atmospheric CO2 and implications for carbon cycle research." Journal of Geophysical Research: Atmospheres **109**(D2).

Oram, D., F. S. Mani, J. Laube, M. Newland, C. Reeves, W. Sturges, S. Penkett, C. Brenninkmeijer, T. Röckmann and P. Fraser (2012). "Long-term tropospheric trend of octafluorocyclobutane (cC 4 F 8 or PFC-318)." Atmospheric chemistry and physics **12**(1): 261-269.

Peylin, P., P. Bousquet, C. Le Quéré, S. Sitch, P. Friedlingstein, G. McKinley, N. Gruber, P. Rayner and P. Ciais (2005). "Multiple constraints on regional CO2 flux variations over land and oceans." Global Biogeochemical Cycles **19**(1): n/a-n/a.

Peylin, P., R. M. Law, K. R. Gurney, F. Chevallier, A. R. Jacobson, T. Maki, Y. Niwa, P. K. Patra, W. Peters, P. J. Rayner, C. Rödenbeck, I. T. van der Laan-Luijkx and X. Zhang (2013). "Global atmospheric carbon budget: results from an ensemble of atmospheric CO$_2$ inversions." Biogeosciences **10**(10): 6699-6720.

Prinn, R., D. Cunnold, R. Rasmussen, P. Simmonds, F. Alyea, A. Crawford, P. Fraser and R. Rosen (1990). "Atmospheric emissions and trends of nitrous oxide deduced from 10 years of ALE–GAGE data." Journal of Geophysical Research: Atmospheres **95**(D11): 18369-18385.

Prinn, R., J. Huang, R. Weiss, D. Cunnold, P. Fraser, P. Simmonds, A. McCulloch, C. Harth, S. Reimann and P. Salameh (2005). "Evidence for variability of atmospheric hydroxyl radicals over the past quarter century." Geophysical Research Letters **32**(7).

Prinn, R., J. Huang, R. Weiss, D. Cunnold, P. Fraser, P. Simmonds, A. McCulloch, C. Harth, P. Salameh and S. O'Doherty (2001). "Evidence for substantial variations of atmospheric hydroxyl radicals in the past two decades." Science **292**(5523): 1882-1888.

Prinn, R., R. Weiss, P. Fraser, P. Simmonds, D. Cunnold, F. Alyea, S. O'Doherty, P. Salameh, B. Miller and J. Huang (2000a). "A history of chemically and radiatively important gases in air deduced from ALE/GAGE/AGAGE." Journal of Geophysical Research: Atmospheres **105**(D14): 17751-17792.

Prinn, R. G., R. F. Weiss, P. J. Fraser, P. G. Simmonds, D. M. Cunnold, F. N. Alyea, S. O'Doherty, P. Salameh, B. R. Miller, J. Huang, R. H. J. Wang, D. E. Hartley, C. Harth, L. P. Steele, G. Sturrock, P. M. Midgley and A. McCulloch (2000b). "A history of chemically and radiatively important gases in air deduced from ALE/GAGE/AGAGE." Journal of Geophysical Research: Atmospheres **105**(D14): 17751-17792.

Rayner, P., I. Enting, R. Francey and R. Langenfelds (1999). "Reconstructing the recent carbon cycle from atmospheric CO2, δ13C and O2/N2 observations*." Tellus B **51**(2): 213-232.

Reimann, S., A. J. Manning, P. G. Simmonds, D. M. Cunnold, R. H. Wang, J. Li, A. McCulloch, R. G. Prinn, J. Huang and R. F. Weiss (2005). "Low European methyl chloroform emissions inferred from long-term atmospheric measurements." Nature **433**(7025): 506-508.

Rhodes, R. H., X. Faïn, C. Stowasser, T. Blunier, J. Chappellaz, J. R. McConnell, D. Romanini, L. E. Mitchell and E. J. Brook (2013). "Continuous methane measurements from a late Holocene Greenland ice core: Atmospheric and in-situ signals." Earth and Planetary Science Letters **368**: 9-19.

Rigby, M., A. L. Ganesan and R. G. Prinn (2011). "Deriving emissions time series from sparse atmospheric mole fractions." Journal of Geophysical Research: Atmospheres **116**(D8): n/a-n/a.

Rigby, M., R. G. Prinn, S. O'Doherty, B. R. Miller, D. Ivy, J. Mühle, C. M. Harth, P. K. Salameh, T. Arnold, R. F. Weiss, P. B. Krummel, L. P. Steele, P. J. Fraser, D. Young and P. G. Simmonds (2014). "Recent and future trends in synthetic greenhouse gas radiative forcing." Geophysical Research Letters **41**(7): 2623-2630.

Rigby, M., R. G. Prinn, S. O'Doherty, S. A. Montzka, A. McCulloch, C. M. Harth, J. Mühle, P. K. Salameh, R. F. Weiss, D. Young, P. G. Simmonds, B. D. Hall, G. S. Dutton, D. Nance, D. J. Mondeel, J. W. Elkins, P. B. Krummel, L. P. Steele and P. J. Fraser (2013). "Re-evaluation of the lifetimes of the major CFCs and CH_3CCl_3 using atmospheric trends." Atmos. Chem. Phys. **13**(5): 2691-2702.

Rubino, M., D. Etheridge, C. Trudinger, C. Allison, M. Battle, R. Langenfelds, L. Steele, M. Curran, M. Bender and J. White (2013). "A revised 1000 year atmospheric δ13C-CO2 record from Law Dome and South Pole, Antarctica." Journal of Geophysical Research: Atmospheres **118**(15): 8482-8499.

Schilt, A., M. Baumgartner, T. Blunier, J. Schwander, R. Spahni, H. Fischer and T. F. Stocker (2010a). "Glacial–interglacial and millennial-scale variations in the atmospheric nitrous oxide concentration during the last 800,000 years." Quaternary Science Reviews **29**(1): 182-192.

Schilt, A., M. Baumgartner, J. Schwander, D. Buiron, E. Capron, J. Chappellaz, L. Loulergue, S. Schüpbach, R. Spahni, H. Fischer and T. F. Stocker (2010b). "Atmospheric nitrous oxide during the last 140,000 years." Earth and Planetary Science Letters **300**(1–2): 33-43.

Shindell, D., G. Faluvegi, L. Nazarenko, K. Bowman, J.-F. Lamarque, A. Voulgarakis, G. A. Schmidt, O. Pechony and R. Ruedy (2013). "Attribution of historical ozone forcing to anthropogenic emissions." Nature Climate Change **3**(6): 567-570.

Simmonds, P., D. Cunnold, R. Weiss, R. Prinn, P. Fraser, A. McCulloch, F. Alyea and S. O'Doherty (1998). "Global trends and emission estimates of CCl4 from in situ background observations from July 1978 to June 1996." Journal of Geophysical Research: Atmospheres **103**(D13): 16017-16027.

Simmonds, P., R. Derwent, A. Manning, P. Fraser, P. Krummel, S. O'doherty, R. Prinn, D. Cunnold, B. Miller and H. Wang (2004). "AGAGE observations of methyl bromide and methyl chloride at Mace Head, Ireland, and Cape Grim, Tasmania, 1998–2001." Journal of atmospheric chemistry **47**(3): 243-269.

Sowers, T., R. B. Alley and J. Jubenville (2003). "Ice core records of atmospheric N2O covering the last 106,000 years." Science **301**(5635): 945-948.

Spahni, R., J. Chappellaz, T. F. Stocker, L. Loulergue, G. Hausammann, K. Kawamura, J. Flückiger, J. Schwander, D. Raynaud and V. Masson-Delmotte (2005). "Atmospheric methane and nitrous oxide of the late Pleistocene from Antarctic ice cores." Science **310**(5752): 1317-1321.

Steele, L. P., E. J. Dlugokencky, P. M. Lang, P. P. Tans, R. C. Martin and K. A. Masarie (1992). "Slowing down of the global accumulation of atmospheric methane during the 1980s." Nature **358**(6384): 313-316.

Steele, L. P., P. J. Fraser, R. A. Rasmussen, M. A. K. Khalil, T. J. Conway, A. J. Crawford, R. H. Gammon, K. A. Masarie and K. W. Thoning (1987). "The global distribution of methane in the troposphere." Journal of Atmospheric Chemistry **5**(2): 125-171.

Steele, L. P. a. P. M. L. (1991). Atmospheric methane concentrations - the NOAA/CMDL global cooperative flask sampling network, 1983-1988.

Sturrock, G. A., D. M. Etheridge, C. M. Trudinger, P. J. Fraser and A. M. Smith (2002). "Atmospheric histories of halocarbons from analysis of Antarctic firn air: Major Montreal Protocol species." Journal of Geophysical Research: Atmospheres **107**(D24): ACH 12-11-ACH 12-14.

Tans, P. P., T. J. Conway and T. Nakazawa (1989). "Latitudinal distribution of the sources and sinks of atmospheric carbon dioxide derived from surface observations and an atmospheric transport model." Journal of Geophysical Research: Atmospheres **94**(D4): 5151-5172.

Tans, P. P., I. Y. Fung and T. Takahashi (1990a). "Observational contrains on the global atmospheric CO2 budget." Science **247**(4949): 1431-1438.

Tans, P. P., K. W. Thoning, W. P. Elliott and T. J. Conway (1990b). "Error estimates of background atmospheric CO2 patterns from weekly flask samples." Journal of Geophysical Research: Atmospheres **95**(D9): 14063-14070.

Thoning, K. W., T. J. Conway, N. Zhang and D. Kitzis (1995). "Analysis System for Measurement of CO2 Mixing Ratios in Flask Air Samples." Journal of Atmospheric and Oceanic Technology **12**(6): 1349-1356.

Thoning, K. W., P. Tans, T.J. Conway, and L.S. Waterman (1987). "NOAA/GMCC calibrations of CO2-in-air reference gases:1979-1985." NOAA Tech. Memo. ERL ARL-150, NOAA Environmental Research Laboratories, Boulder, CO.

Thoning, K. W., P. P. Tans and W. D. Komhyr (1989). "Atmospheric carbon dioxide at Mauna Loa Observatory: 2. Analysis of the NOAA GMCC data, 1974–1985." Journal of Geophysical Research: Atmospheres **94**(D6): 8549-8565.

Trolier, M., J. W. C. White, P. P. Tans, K. A. Masarie and P. A. Gemery (1996). "Monitoring the isotopic composition of atmospheric CO2: Measurements from the NOAA Global Air Sampling Network." Journal of Geophysical Research: Atmospheres **101**(D20): 25897-25916.

Trudinger, C., D. Etheridge, G. Sturrock, P. Fraser, P. Krummel and A. McCulloch (2004). "Atmospheric histories of halocarbons from analysis of Antarctic firn air: Methyl bromide, methyl chloride, chloroform, and dichloromethane." Journal of Geophysical Research: Atmospheres **109**(D22).

Trudinger, C. M., D. M. Etheridge, P. J. Rayner, I. G. Enting, G. A. Sturrock and R. L. Langenfelds (2002). "Reconstructing atmospheric histories from measurements of air composition in firn." Journal of Geophysical Research: Atmospheres **107**(D24): ACH 15-11-ACH 15-13.

Trudinger, C. M., P. J. Fraser, D. M. Etheridge, W. T. Sturges, M. K. Vollmer, M. Rigby, P. Martinerie, J. Mühle, D. R. Worton, P. B. Krummel, L. P. Steele, B. R. Miller, J. Laube, F. Mani, P. J. Rayner, C. M. Harth, E. Witrant, T. Blunier, J. Schwander, S. O'Doherty and M. Battle (2016). "Atmospheric abundance and global emissions of perfluorocarbons CF4, C2F6 and C3F8 since 1900 inferred from ice core, firn, air archive and in situ measurements." Atmos. Chem. Phys. Discuss. **2016**: 1-34.

Tsutsumi, Y., M. Kazumasa, H. Takatoshi, I. Masaaki and T.J. Conway (2009). Technical Report of Global Analysis Method for Major Greenhouse Gases by the World Data Center for Greenhouse Gases. WMO/TD-No. 1473, World Meteorological Organization Global Atmosphere Watch. **GAW Report No. 184**.

Velders, G. J. M., S. Solomon and J. S. Daniel (2014). "Growth of climate change commitments from HFC banks and emissions." Atmos. Chem. Phys. **14**(9): 4563-4572.

Vollmer, M. K., B. R. Miller, M. Rigby, S. Reimann, J. Mühle, P. B. Krummel, S. O'Doherty, J. Kim, T. S. Rhee, R. F. Weiss, P. J. Fraser, P. G. Simmonds, P. K. Salameh, C. M. Harth, R. H. J. Wang, L. P. Steele, D. Young, C. R. Lunder, O. Hermansen, D. Ivy, T. Arnold, N. Schmidbauer, K.-R. Kim, B. R. Greally, M. Hill, M. Leist, A. Wenger and R. G. Prinn (2011). "Atmospheric histories and global emissions of the anthropogenic hydrofluorocarbons HFC-365mfc, HFC-245fa, HFC-227ea, and HFC-236fa." Journal of Geophysical Research: Atmospheres **116**(D8): n/a-n/a.

Vollmer, M. K., J. Mühle, C. M. Trudinger, M. Rigby, S. A. Montzka, C. M. Harth, B. R. Miller, S. Henne, P. B. Krummel and B. D. Hall (2016). "Atmospheric histories and global emissions of halons H-1211 (CBrClF2), H-1301 (CBrF3), and H-2402 (CBrF2CBrF2)." Journal of Geophysical Research: Atmospheres **121**(7): 3663-3686.

1784 Welp, L. R., P. K. Patra, C. Rödenbeck, R. Nemani, J. Bi, S. C. Piper and R. F. Keeling (2016). "Increasing summer net
1785 CO2 uptake in high northern ecosystems inferred from atmospheric inversions and remote sensing." Atmos.
1786 Chem. Phys.(Discuss), submitted.
1787 WMO (2012). WMO WDCGG Data Summary 36. Global Atmosphere Watch (GAW) Data Volumne IV - Greenhouse
1788 Gases and Other Atmospheric Gases, Japan Meterological Agency and WMO,: 100.
1789 WMO (2014). Scientific Assessment of Ozone Depletion: 2014. World Meteorological Organization Global Ozone
1790 Research and Monitoring Project - Report No. 55. Geneva, Switzerland, World Meteorological Organization: 416.
1791 Worton, D. R., W. T. Sturges, J. Schwander, R. Mulvaney, J. M. Barnola and J. Chappellaz (2006). "20th century
1792 trends and budget implications of chloroform and related tri-and dihalomethanes inferred from firn air." Atmos.
1793 Chem. Phys. **6**(10): 2847-2863.
1794 Xiang, B., P. K. Patra, S. A. Montzka, S. M. Miller, J. W. Elkins, F. L. Moore, E. L. Atlas, B. R. Miller, R. F. Weiss, R. G.
1795 Prinn and S. C. Wofsy (2014). "Global emissions of refrigerants HCFC-22 and HFC-134a: Unforeseen seasonal
1796 contributions." Proceedings of the National Academy of Sciences **111**(49): 17379-17384.
1797 Zhao, C. L. and P. P. Tans (2006). "Estimating uncertainty of the WMO mole fraction scale for carbon dioxide in
1798 air." Journal of Geophysical Research: Atmospheres **111**(D8): n/a-n/a.

1799